Atomic Coherence and its Spectroscopic Applications

A thesis submitted in partial fulfillment of the requirements for the award of

Doctor of Philosophy

by

Ogaro Elijah Nyakang'o

(166121022)

Department of Physics

Indian Institute of Technology Guwahati
Guwahati - 781039, India.

April, 2021

Dedication

Dedicated to my family

Declaration

I, hereby, declare that the work reported in this thesis has been carried out in the Department of Physics, Indian Institute of Technology Guwahati, under the supervision of Dr. Kanhaiya Pandey. The work is original and has not been submitted in part or as a whole for the award of a degree or any other award in any institution or university.

Ogaro Elijah Nyakang'o
April, 2021

Certification

This is to certify that the work contained in the thesis entitled “Atomic coherence and its spectroscopic applications” submitted by Mr. Ogaro Elijah Nyakang’o in the partial fulfillment of the requirement for the award of the degree of Doctor of Philosophy in Physics, Department of Physics, Indian Institute of Technology Guwahati, is a record of the candidate’s own work carried out by him under my supervision and guidance. The matter embodied in this report has not been submitted in part or full to any other university or institute for the award of any degree.

Dr. Kanhaiya Pandey
Assistant Professor
Department of Physics
Indian Institute of Technology Guwahati
Guwahati - 781039
Assam, India.
April, 2021

Acknowledgements

I take this opportunity to acknowledge the persons to whom I owe my thanks for the successful completion of my PhD research work. My warm thanks are due to Dr. Kanhaiya Pandey whose wide experience in atomic physics, precision measurement, quantum optics, laser cooling, theoretical and numerical computations has been of great value for me. I am deeply grateful for the inspiration and motivation he provided to me during the entire research work period. His insightful comments, criticism and suggestions on different topics of the research work was instrumental for my success.

I also thank my doctoral committee members, Prof. Amarendra Kumar Sarma, Dr. Tapan Mishra and Dr. Sisir Kumar Nayak for their insightful comments and suggestion during my review seminars. Many thanks also goes to all the professors in the Department of Physics for their critical role during the course work period.

I also acknowledge Indian Council for Cultural Relations (ICCR) for the PhD scholarship. The financial assistance from ICCR helped me to successfully complete my research work at IIT Guwahati. Many thanks indeed for the opportunity accorded to me to pursue my childhood dreams.

I am greatly indebted to my parents, my wife and children for their constant support and encouragement throughout the research work period. Without their support and prayer, this work would not have been possible. I salute you all.

I extend my special thanks to my research group members Dangka Shylla and Rajnandan Choudhury Das for their great support during the research work period. I also thank all my batch-mates (2016) for their encouragement and entertaining company in the entire PhD research period.

Finally, I bow my head before God Almighty for His blessings in the successful completion of this work.

Abstract

Spectroscopy and stabilization of the laser at a particular transition is key in the modern area of atomic and optical physics. The present thesis details the mechanism of induced atomic coherence between multi-level atomic system driven by lasers and their role in the absorption and fluorescence spectrum. The theoretical study presents a frame work to identify the nature and the role of interference between the excitation paths associated with the Autler-Townes (AT) peaks (i.e., a pair of transitions from the ground state to the dressed states) in a multi-level system. In three-level system the excitation paths associated with the two AT peaks interferes pair-wise and the nature of interference is very simple which can be constructive, destructive or no interference depending upon the decay rate of the states coupled by the strong control lasers. In four-level system the nature of interference is more complicated but again the excitation paths associated with all the three AT peaks interferes pair-wise. For any system, if the decay rate of the levels coupled by the control lasers are equal then there is no interference between any of the excitation paths associated with the AT peaks.

We further studied the saturated fluorescence spectroscopy which is a very useful spectroscopic technique for weak transitions. In the study, the Doppler-free fluorescence dip in the fluorescence spectra is caused by velocity selective saturation (VSS) effect and the dip is further modified by velocity induced population oscillation (VIPO) effect. The VIPO effect is caused by the beating of two counter-propagating elec-

tromagnetic fields in a moving atomic frame (due to opposite Doppler shift for a given velocity). The line-shape of the saturated fluorescence dip is sensitive to the laser beam misalignment in the case of the atomic beam. The shifts of the fluorescence dip is dependent on the average velocity of the atomic beam and the angles of misalignment of the laser beams.

The theoretical study is experimentally utilized for double resonance spectroscopy at infrared ($5S_{1/2} \rightarrow 5P_{3/2}$) strong transition and blue ($5S_{1/2} \rightarrow 6P_{1/2}$) weak transition in Rb atom. The double resonance (at 780 nm and 421 nm) is implemented using EIT effect in a V-type system and enhanced absorption (EA) effect in optical pumping system. The scan non-linearity of the blue laser (which is the dominant source of error in the experiment) is minimized by using acousto-optic modulator to shift the laser frequency within a small range of frequencies around the neighboring hyperfine level. The hyperfine splitting of the $6P_{1/2}$ state is measured with a precision of < 400 kHz and the magnetic dipole hyperfine constant is also calculated.

We further utilized VIPO at infrared transition, VSS at blue transition and the combination of the two effects to resolve closely spaced hyperfine levels of a weak transition by eliminating the residual (or partial) two-photon Doppler broadening in a wavelength mismatched double resonance spectroscopy. The double resonance experiment is conducted on $5S_{1/2} \rightarrow 5P_{3/2}$ strong transition (at 780 nm) and $5S_{1/2} \rightarrow 6P_{3/2}$ weak transition (at 420 nm) in Rb atom at room temperature. The residual Doppler broadening is caused by the thermal motion of the atoms in the vapor cell. The elimination of the partial Doppler broadening using the VIPO and VSS effects is followed by the subtraction of the broad background of the two-photon spectrum. Since the VIPO and VSS effects are phenomena for near zero velocity group atoms, the subtraction gives rise to Doppler-free peaks and the closely spaced hyperfine levels of the $6P_{3/2}$ state in Rb are well resolved. The resolved peaks with narrow linewidth, are important for stabilizing the blue laser at a particular transition (i.e., for tight laser locking) for future goals of laser cooling and trapping at this transition. The spectroscopy and stabilization of the blue laser is also beneficial for quantum information processing with coherent excitation of Rydberg states in Rb atoms.

List of publications

Publications for the work reported in this thesis:

[1] **Elijah Ogaro Nyakang'o**, Dangka Shylla, Kirthanaa Indumathi, and Kanhaiya Pandey, "*Nature of interference between Autler-Townes (AT) peaks in generic multi-level system*", Eur. Phys. J. D (2020) 74: 187 (https://doi.org/10.1140/epjd/e2020-10187-3)

[2] **Elijah Ogaro Nyakang'o**, Dangka Shylla, Vasant Natarajan and Kanhaiya Pandey, "*Hyperfine measurement of the $6P_{1/2}$ state in ^{87}Rb using double resonance on blue and IR transition*", J. Phys. B: At. Mol. Opt. Phys. 53 (2020) 095001 (6pp) (https://doi.org/10.1088/1361-6455/ab7670).

[3] **Elijah Ogaro Nyakang'o** and Kanhaiya Pandey, "*Role of velocity induced coherent population oscillation in saturated fluorescence spectroscopy*", Eur. Phys. J. D (2020) 74: 96 (https://doi.org/10.1140/epjd/e2020-100519-0)

[4] **Elijah Ogaro Nyakang'o** and Kanhaiya Pandey, "*Resolving closely spaced levels for Doppler mismatched double resonance*", Phys. Rev. A 103, 013107 (2021) (https://doi.org/10.1103/PhysRevA.103.013107)

Additional publications:

[1] Dangka Shylla, **Elijah Ogaro Nyakang'o** and Kanhaiya Pandey, "*Highly sensitive atomic based MW interferometry*", Sci Rep 8, 8692 (2018) (https://doi.org/10.1038/s41598-018-27011-1)

Contents

List of Figures

List of Tables

1

Introduction

1.1 Introduction

The interaction of coherent light fields with an atomic medium has been immensely studied in the past few decades, especially on the ability to control and manipulate optical properties of the atomic medium. The formation of atomic coherence is the key to control and manipulate optical properties of the atomic medium for a variety of applications such as slowing and stopping of light [1, 2], storage of light [3, 4], quantum memory [5, 6, 7], atomic clock [8, 9], laser cooling [10] and also in laser spectroscopy. Atomic coherence is the induced coherence between levels of a multi-level atomic system, when it interacts with lasers.

Atomic coherence in a three-level system has been studied in a Λ-type, V-type and Ξ-type atomic systems [11, 12, 13]. In these systems, the fields drives the two different transitions with a shared common atomic level. This creates atomic coherences between the different transition pathways of the three level system which can interfere and leads to exciting quantum optical phenomena. The induced quantum phenomena includes, coherent population trapping (CPT) [14], electromagnetically induced transparency (EIT) [11, 15], electromagnetically induced absorption (EIA) [16], and lasing without inversion (LWI) [17, 18].

For example, the CPT phenomena occurs when two resonant optical fields interacts with atoms in a Λ-type system. If the frequency difference between the two optical fields matches the two-photon resonance (i.e., the microwave transition frequency of the two ground states), the atoms are placed in coherent superposition of states which is completely decoupled from both optical fields (also known as the dark state). The CPT phenomena is studied in the regime where two lasers (pump and probe) are of same intensity and the lasers should be phase coherent which is necessary for the stability of the induced dark superposition state.

The EIT effect on the other hand, is observed when a strong resonant pump drives one transition while the weak probe scans across the shared atomic level on the other transition. There are generally two approaches to theoretically study the EIT effect. The first approach is laser induced coherence between the levels which is also known as transfer of coherence since, the simultaneous driving of different levels with lasers induces coherence between levels which are not directly driven. The other approach is dressed states created by the pump laser and their excitation by the probe laser. The resonant strong pump laser shifts the atomic levels through the ac stark shift effect (or Autler-Townes (AT) splitting) [19]. The splitting of the atomic levels is equal to the Rabi frequency of the pump laser. The absorption of the probe laser tuned at the line center is reduced by two effects. One is the absorption due to the dressed states (or AT absorption peaks) and the other is quantum interference between the different excitation pathways of the dressed states created by the pump laser [17, 20].

Atomic coherences play a key role in high precision spectroscopy [21, 22, 23, 24] to discribe the line profile of the spectrum. For example, in the pump-probe spectroscopy of a two-level atomic system, a dip is induced in the probe absorption profile when it interacts with two coherent light fields. The induced dip is commonly known as the Lamb dip and is due to two closely related effects. The first one is the saturation of the transition by the strong pump [25, 26] and the other is coherent population oscillation due to the beating of the fields [27]. In the atomic frame of moving atoms, the two counter-propagating laser fields (pump and probe) with the same polarization and driving the same transition, will be beating due to opposite Doppler shift. The beating of the two laser fields causes a temporal modulation of population difference between the levels driven by the lasers. The spectroscopy based on the Lamb dip effect is known as saturated absorption spectroscopy [28, 29]. Saturated fluorescence spectroscopy is another technique which is very useful for the spectroscopy of weak transitions when absorption by the medium is much smaller than intensity noise in the laser beam [30, 26, 31, 32]. In this method, a fluorescence dip is observed in the Doppler broadened fluorescence profile of the two strong counter-propagating laser beams [26, 27]. The observed fluorescence dip is due to the velocity selective saturation and coherent population oscillation effects.

The atomic coherence also plays important role in pump-probe spectroscopy of a three-level atomic system such as the V-type [22, 33, 34] and Ξ-type [24] atomic systems. The method is very useful for the spectroscopy of weak transitions (such as $5S \rightarrow 6P$ in Rb) where direct detection of absorption is a bit challenging [21, 35] and also for transitions which are not directly accessed from the ground state (the Ξ-type atomic system [24]). The absorption of the weak probe (locked to resonance in one transition) is monitored as the strong pump scans across the shared atomic level on the other transition. As soon as the scanning pump comes to resonance, (i.e., when both laser beams are addressing zero velocity group atoms), the probe absorption is reduced at the line center (and hence the name double resonance spectroscopy). The reduction of probe absorption is due to population transfer caused by the strong pump and the coherence effect causing EIT.

1.2 Motivation

In this section, we describe the motivation behind the spectroscopy of 5S → 6P transition in Rb, which is a widely used element in atomic physics for the spectroscopy [36, 37, 38, 39, 40, 41] and laser cooling experiments. For the laser cooling of atoms, it is crucial to stabilize the laser frequency to the correct value by first performing accurate spectroscopy of the atom. The laser cooling (or Doppler cooling) and trapping (magneto-optical trapping) of Rb atoms is routinely implemented using the $5S_{1/2} \rightarrow 5P_{3/2}$ transition (at 780 nm) with a cooling temperature of up to around 200 μK in a magneto-optical trap [42, 43]. However, the weak and narrow linewidth ($2\pi \times 1.32$ MHz [44]) transition in the blue region (i.e., $5S_{1/2} \rightarrow 6P_{3/2}$ at 420 nm) is unexplored for cooling and trapping of Rb. The expected cooling temperature on the blue transition is 5 times lower in the magneto-optical trap than the routinely used IR transition, which is similar to the case of K [45] and Li [46].

Stabilization of the laser frequency is also crucial for precise measurements of atomic transition frequencies and hyperfine structure of various lines. The precision measurements on the blue transition (5S → 6P) adds important input to theoretical calculations of physical quantities such as hyperfine structure constants (magnetic dipole and electric quadrupole constants) [21, 22, 47]. Accurate values of physical quantities, are useful for experimental innovations on novel ways to manipulate atomic states e.g., quantum computation and information processing with coherent Rydberg excitation of Rb atoms [48]. The Rb Rydberg atoms are commonly excited from the 5S ground state to Rydberg states via a three-level ladder scheme 5S → 5P → nS or nD (high n principal quantum numbers) using the lasers at 780 nm and 480 nm respectively. The 480 nm laser is generated using frequency doubling of 960 nm laser [49], which unfortunately limits the available laser power. An alternative and promising route for excitation of Rydberg states, is the use of the 6P state as the intermediate state via a three-level ladder scheme 5S → 6P → nS or nD using the lasers at 420 nm and

1016 nm respectively [50]. The commercially available external cavity diode lasers (ECDL) at 420 nm and 1016 nm respectively, have high power which allows high Rabi frequencies for the excitation to Rydberg states.

The precisely measured absolute frequency of the $5S_{1/2} \rightarrow 5P_{3/2}$ transition in Rb using the single-photon at 780 nm [36, 37, 38], is used as a low cost optical frequency standards for measuring unkown transitions [38]. However, the weak and narrow linewidth 5S → 6P [51] transition in the blue region (at 420 nm and 421 nm) has the advantage of high precision for frequency standards [52, 53] and is a promising candidate for metrology. The hyperfine splitting measurement of the 6P states has been carried out using saturated absorption [21] for both $6P_{1/2}$ and $6P_{3/2}$ states, or fluorescence spectroscopy [54] for $6P_{3/2}$ state on 5S → 6P transition, double resonace in a Doppler mismatched configurations for $6P_{1/2}$ [22] and using RF transition with electrical discharge [55].

The direct detection of absorption of the blue laser on 5S → 6P transition requires heating of Rb vapor cell up to $80 - 100°$C [21, 35] and using a photodiode with blue enhanced sensitivity. Heating of the cell adds further experimental complicacy such as the coating on the cell which reduces the signal to noise ratio. The heating of the Rb cell also increases atom-atom collision and can cause collisional/pressure shift [56] which can contribute to systematic shift in the hyperfine measurement. An altinative method is the use of double resonance spectroscopy [22, 33, 57, 58] which again suffers through residual (or partial) Doppler broadening for the two-photon electromagnetically induced transparency (EIT) [11, 15]. The cancellation of the Doppler broadening is only possible if the wavelength of the lasers is approximately the same [11, 59, 60, 61] otherwise suffers through partial Doppler broadening due to wavelengths mismatch of the transitions involved [24, 57, 62, 63].

The partial Doppler broadening due to wavelengths mismatch between the probe and pump lasers in the double resonance spectroscopy, is overcome using velocity induced population oscillation (VIPO) and velocity selective saturation (VSS) effects. In the atomic frame of moving atoms, the two counter-propagating laser fields (IR pump and probe) driving the same transition and have same polarization, will be beating due to opposite Doppler shift. The beating of the two laser fields causes a temporal modulation of population difference between the levels driven by the lasers and the phenomenon is called population oscillation [64, 65, 66, 67, 68, 69, 70]. Since the two beating fields have same frequency, the induced population oscillation is dependent on the velocity of the atom and hence the name velocity induced population oscillation (VIPO) [27]. The VIPO effect occurs only for a narrow range of beat frequencies (i.e., near zero velocity range) because of the inherent population inertia causing a slow response of electric dipoles to incident fields. The range of beat frequencies is determined by the inverse of population relaxation times of the upper levels [27, 70, 71]. Similarly, VSS effect is also for near zero velocity group atom (for the two scanning counter-propagating pump on the blue transition 5S → 6P). The effect of partial Doppler broadening is removed for multi-photon resonance by the subtraction of the broad transparency or absorption background.

1.3 Thesis overview

Spectroscopy and stabilization of the laser at a particular transition is key in the modern area of atomic and optical physics. The spectroscopy of weak transitions is challenging and is the main goal of this thesis. The thesis details the mechanism of induced atomic coherence between multi-level atomic system driven by lasers and their role in the absorption and fluorescence spectrum. The theoretical study is further experimentally utilized for double resonance spectroscopy at infrared (strong transition) and blue (weak) transition in Rb atom. The spectroscopy of the blue transition is very important for future goals of laser cooling and trapping at this transition and also for quantum information processing with coherent excitation of

Rydberg states in Rb atoms. The thesis consist of seven chapters with the following details.

Chapter 1 gives an introduction to atomic coherence in multilevel systems and its spectroscopic applications, the motivation of the research work and the general overview of the thesis.

Chapter 2 describes the theoretical background of atom-light interaction using a semi-classical approach. The approach, treats light as a classical field and the atom as a quantum system with discrete levels in-order to derive the Hamiltonian of light-atom interaction. The next section of the chapter discusses the density matrix formalism which is important to describe the spectral profile of the probe laser. The last section of the chapter presents the basic concepts of atomic hyperfine structure.

Chapter 3 discusses a theoretical frame work to identify the role and the nature of interference between the excitation paths associated with Autler-Townes (AT) peaks (i.e., a pair of transitions from the ground state to the dressed states) in generic multi-level system. The destructive interference between the excitation paths associated with the AT peaks, give rise to sharp transparency window known as electromagnetically induced transparency (EIT). The chapter presents a detailed analysis on the nature of interference between the excitation paths associated with the AT peaks in the three-level and four-level systems in subsequent sections.

Chapter 4 discusses the spectroscopy of the $6P_{1/2}$ state in ^{87}Rb using double resonance technique at 780 nm and 421 nm. The chapter begins with a detailed theoretical description of the double resonance technique using the EIT effect in a V-type system and enhanced absorption (EA) effect in the optical pumping system. The subsequent sections of the chapter, discusses the measurement of the hyperfine splitting of the $6P_{1/2}$ state using this techniques with precision of < 400 kHz.

Chapter 5 discusses a theoretical framework to identify the role of velocity induced coherent population oscillation in saturated fluorescence spectroscopy in a two-level system, which is a very useful spectroscopic technique for weak transitions. The fluorescence dip in a fluorescence spectra is due to the VSS and VIPO effects. The chapter further discusses the effect of the temperature of the atomic gas and the applied laser beam intensity on the linewidth and dip height of the fluorescence dip in subsequent sections. The last section of the chapter presents a detailed discussion on the fluorescence dip in the case of an atomic beam and the effects of laser beams misalignment.

Chapter 6 discusses experimental techniques to resolve the closely spaced hyperfine levels of weak transition by eliminating the residual (or partial) two-photon Doppler broadening and cross-over resonances in a wavelength mismatched double resonance spectroscopy. The first sections of the chapter presents a theoretical analysis on the VIPO and VSS effects in a V-type and optical pumping systems. The subsequent sections of chapter discuses experimental result of resolving the closely spaced hyperfine levels of the $6P_{3/2}$ state in Rb using the VIPO and VSS effects.

Chapter 7 presents the conclusions of the thesis and future work.

2

Theoretical background of light-atom interaction

This chapter reviews the formulation of light-atom interaction using a semi-classical approach. The approach, treats light as a classical field and the atom as a quantum system with discrete levels. The semi-classical theory, successfully explains most of the experimentally observed phenomena arising from light-atom interaction in quantum optics [19, 72]. The theory is used to study the various experimental observations related to light-atom interaction in the present thesis research work. To begin with, the following section gives a quantum description by considering a time-dependent Schrödinger equation and the equations of motion for the density matrix.

2.1 The Hamiltonian

The Hamiltonian H of the atomic system is given as $H = H_0 + H_I$, where H_0 is the Hamiltonian of the atom without interaction and H_I is the interaction Hamiltonian between the atom and the driving light fields. Using the complete orthonormal basis of the atomic states, $\sum_i |i\rangle\langle i| = \mathbb{1}$ and $\langle i|j\rangle = \delta_{ij}$, H will transforms as,

$$\begin{aligned} H &= \sum_{i,\ j} |i\rangle\langle i|\left(H_0 + H_I\right)|j\rangle\langle j| \\ &= \sum_{i,\ j} |i\rangle\langle i| H_0 |j\rangle\langle j| + \sum_{i,\ j} |i\rangle\langle i| H_I |j\rangle\langle j| , \end{aligned} \tag{2.1}$$

with H_0 of the atomic system given as follows:

$$\begin{aligned} H_0 &= \sum_{i,\ j} |i\rangle\langle i| H_0 |j\rangle\langle j| \\ &= \sum_{i} \hbar\omega_i |i\rangle\langle i| , \end{aligned} \tag{2.2}$$

where, $H_0 |j\rangle = \hbar\omega_j |j\rangle$ and $\langle i|j\rangle = \delta_{ij}$.

We define $H_I = E_0\hat{\boldsymbol{\varepsilon}}.\mathbf{d}\cos\left(\omega^l_{ij}t\right)$ where, E_0 is the electric field amplitude, $\hat{\boldsymbol{\varepsilon}}$ is the unit polarization vector of the light field, ω^l_{ij} is the laser frequency near resonance to $|i\rangle \rightarrow |j\rangle$ transition and $\mathbf{d}$ is the dipole operator. From Eq. 2.1 H_I is given as follows:

$$\begin{aligned} H_I = E_0\hat{\boldsymbol{\varepsilon}}.\mathbf{d}\cos\left(\omega^l_{ij}t\right) &= E_0\cos\left(\omega^l_{ij}t\right)\left(\sum_{i,\ j} |i\rangle\langle i| \hat{\boldsymbol{\varepsilon}}.\mathbf{d} |j\rangle\langle j|\right) \\ &= E_0\cos\left(\omega^l_{ij}t\right)\sum_{i,\ j} \mathrm{d}_{ij} |i\rangle\langle j| , \end{aligned} \tag{2.3}$$

where, $\mathrm{d}_{ij} = \langle i| \hat{\boldsymbol{\varepsilon}}.\mathbf{d} |j\rangle$ is a dipole matrix element. Note that the dipole matrix element $\langle i| \hat{\boldsymbol{\varepsilon}}.\mathbf{d} |i\rangle = 0$, because the dipole operator $\hat{\boldsymbol{\varepsilon}}.\mathbf{d}$ is odd parity and does not couple states of the same parity. Similarly, the dipole matrix element $\langle i| \hat{\boldsymbol{\varepsilon}}.\mathbf{d} |j\rangle = 0$ if the states i and j have same parity. We also define $\Omega_{ij} = \frac{E_0\mathrm{d}_{ij}}{\hbar}\cos\left(\omega^l_{ij}t\right)$ which is known as Rabi frequency. From the definition of the Rabi frequency, $\Omega_{ij} = \Omega^*_{ij}$ and H_I becomes:

$$H_I = \sum_{i,\ j} \frac{\Omega_{ij}}{2}\left(e^{i\omega^l_{ij}t} + e^{-i\omega^l_{ij}t}\right)|i\rangle\langle j| , \tag{2.4}$$

where, the sum is over all possible transition.

2.1.1 Rotating wave approximation

The Hamiltonian given in Eq. 2.4 is transformed into the interaction picture using a unitary matrix U_1 defined as,

$$U_1 = e^{iH_0 t/\hbar} = \sum_j e^{i\omega_j t} |j\rangle \langle j| , \tag{2.5}$$

and therefore H_I transforms as $U_1 H_I U_1^\dagger$ and is given as follows:

$$H_I = \sum_{i,\ j} \frac{\Omega_{ij}}{2} \left(e^{i\omega^l_{ij} t} + e^{-i\omega^l_{ij} t} \right) e^{-i(\omega_j - \omega_i)t} |i\rangle \langle j| . \tag{2.6}$$

The rapidly oscillating terms under this transformation will average out. The exponential terms with large imaginary arguments such as $e^{\mp i(\omega^l_{ij} + (\omega_j - \omega_i))t}$ (if $\omega_j > \omega_i$ and $\omega_i > \omega_j$ respectively) are therefore dropped out. While the slowly oscillating exponential terms with imaginary arguments of the form $e^{\pm i(\omega^l_{ij} - (\omega_j - \omega_i))t}$ are retained. This approximation is called rotating wave approximation (RWA) and is valid when $|\Omega_{ij}| \ll \omega^l_{ij}$. The detuning of the driving light field is defined as $\delta_{ij} = \omega^l_{ij} - (\omega_j - \omega_i)$ and therefore H_I is now written as follows:

$$\begin{aligned} H_I =& \frac{\hbar}{2} \Big\{ \Omega_{12} e^{i\delta_{12} t} |1\rangle \langle 2| + \Omega_{13} e^{i\delta_{13} t} |1\rangle \langle 3| + \cdots + \Omega_{23} e^{\pm i\delta_{23} t} |2\rangle \langle 3| + \\ & \Omega_{24} e^{\pm i\delta_{24} t} |2\rangle \langle 4| + \cdots + \Omega_{n-1n} e^{\pm i\delta_{n-1n} t} |n-1\rangle \langle n| + \text{H.c.} \Big\}, \end{aligned} \tag{2.7}$$

(where, H.c. is Hermitian conjugate) and the total Hamiltonian $H = H_0 + H_I$ is now written as follows:

$$\begin{aligned}H =&\frac{\hbar}{2}\Big\{\Omega_{12}e^{i\delta_{12}t}\left|1\right\rangle\left\langle 2\right| + \Omega_{13}e^{i\delta_{13}t}\left|1\right\rangle\left\langle 3\right| + \cdots + \Omega_{23}e^{\pm i\delta_{23}t}\left|2\right\rangle\left\langle 3\right| + \\ &\Omega_{24}e^{\pm i\delta_{24}t}\left|2\right\rangle\left\langle 4\right| + \cdots + \Omega_{n-1n}e^{\pm i\delta_{n-1n}t}\left|n-1\right\rangle\left\langle n\right| + \text{H.c.} + 2\sum_i \omega_i \left|i\right\rangle\left\langle i\right|\Big\}.\end{aligned} \tag{2.8}$$

2.1.2 Corotating frame

The Hamiltonian H appearing in Eq. 2.8, transforms in the rotating basis as $\tilde{H} = U_2 H U_2^\dagger$ where, U_2 is a unitary matrix defined as,

$$U_2 = 1\left|1\right\rangle\left\langle 1\right| + e^{i\delta_{12}t}\left|2\right\rangle\left\langle 2\right| + e^{i(\delta_{23}t\pm\delta_{12}t)}\left|3\right\rangle\left\langle 3\right| + e^{i(\delta_{34}t\pm\delta_{23}t\pm\delta_{12}t)}\left|4\right\rangle\left\langle 4\right| + \cdots, \tag{2.9}$$

for atomic systems such as ladder-type, lambda-type, N-type and M-type systems (the plus sign is for $\omega_j > \omega_i$ and the minus sign is for $\omega_i > \omega_j$) and

$$U_2 = 1\left|1\right\rangle\left\langle 1\right| + e^{i\delta_{12}t}\left|2\right\rangle\left\langle 2\right| + e^{i\delta_{13}t}\left|3\right\rangle\left\langle 3\right| + \cdots + e^{i\delta_{1n}t}\left|n\right\rangle\left\langle n\right|, \tag{2.10}$$

for the V-type system. The rotating basis $|\tilde{\psi}\rangle$ is related to the old basis $\left|\psi\right\rangle$ by $|\tilde{\psi}\rangle = U_2\left|\psi\right\rangle$ and the Schrödinger equation holds in the new basis as well,

$$\begin{aligned}\tilde{H}|\tilde{\psi}\rangle &= i\hbar\frac{\partial}{\partial t}|\tilde{\psi}\rangle \\ &= i\hbar\frac{\partial}{\partial t}\Big(U_2\left|\psi\right\rangle\Big) \\ &= i\hbar\Big(\frac{\partial U_2}{\partial t}\left|\psi\right\rangle + U_2\frac{\partial\left|\psi\right\rangle}{\partial t}\Big) \\ &= \Big(i\hbar\frac{\partial U_2}{\partial t}U_2^\dagger + U_2 H U_2^\dagger\Big)U_2\left|\psi\right\rangle, \\ \tilde{H}|\tilde{\psi}\rangle &= \Big(i\hbar\frac{\partial U_2}{\partial t}U_2^\dagger + U_2 H U_2^\dagger\Big)|\tilde{\psi}\rangle.\end{aligned} \tag{2.11}$$

2.2 Density matrix formalism

The atomic systems consist of discrete energy levels which are associated with a unique wave function, $|\psi\rangle$ which gives a complete information about a system in a pure state. Experimentally, the expectation value of the quantum mechanical operators is measured directly and not $|\psi\rangle$. The physical observables are represented by the Hermitian operators, $\hat{A}$ and the corresponding measured experimental value is written as the expectation value as follows,

$$\langle \hat{A} \rangle = \langle \psi | \hat{A} | \psi \rangle \, . \tag{2.12}$$

Alternatively, the state of the system is defined by the density operator $\rho = |\psi\rangle \langle \psi|$ for a pure system. The density matrix operator of a mixed ensemble of the system is

$$\rho = \sum_i P_i \, |\psi_i\rangle \langle \psi_i| \, , \tag{2.13}$$

where, P_i is the probability that the system is in state $|\psi_i\rangle$ at time t. The equation of motion for the density matrix is obtained from the time derivative of Eq. 2.13 and the time dependent Schrödinger equation ($i\hbar \frac{\partial |\psi\rangle}{\partial t} = H |\psi\rangle$) as follows:

$$\begin{aligned}
\dot{\rho} &= \sum_i P_i (|\dot{\psi}_i\rangle \langle \psi_i| + |\psi_i\rangle \langle \dot{\psi}_i|) \\
&= -\frac{i}{\hbar} \sum_i P_i (H |\psi_i\rangle \langle \psi_i| + |\psi_i\rangle \langle \psi_i| \, H) \\
&= -\frac{i}{\hbar} [H, \rho]. \qquad (2.14)
\end{aligned}$$

Equation 2.14 is the Liouville-Von Neumann equation and describes only the coherent interaction processes. The incoherent processes such as spontaneous decay, collisional relaxation and the transit relaxation rates are incorporated phenomenologically as follows:

$$\dot{\rho} = -\frac{i}{\hbar}[H, \rho] - \frac{1}{2}\{\Gamma, \rho\}, \tag{2.15}$$

where, Γ is the relaxation operator defined as $\langle i | \, \Gamma \, | j \rangle = \gamma_i \delta_{ij}$ ($\delta_{ij} = 1$ if $i = j$ and 0 if $i \neq j$) and γ_i is the decay rate of state $|i\rangle$. The equations of motion expressed in Eq. 2.15 will be used to numerically and theoretically analyze the atomic spectra for a variety of systems considered in the thesis.

2.3 The fine and hyperfine structures

In the light-atom interaction, the fine and hyperfine levels are involved for a variety of studies in quantum optics. The hyperfine levels in particular, are used to construct a variety of different atomic systems (such as Λ-type, V-type, Ξ-type, N-type and M-type) for a variety of applications. In addition, precise measurements of the hyperfine structure of various lines is particularly useful to extract key information about the properties of the nucleus (such as the electric and magnetic moments) and its influence on atomic wavefunctions [73]. Atomic spectra are useful tools for probing the different kinds of interactions in the atom. In this section we provide a brief discussion on the theory of fine and hyperfine interaction.

2.3.1 Fine structure

The fine structure is the splitting of the spectral lines of atoms which arises from the spin-orbit coupling (i.e., the coupling of orbital angular momentum **L** of the outer electron with its spin angular momentum **S**). The total electron angular momentum is related to **L** and **S** as follows:

$$\mathbf{J} = \mathbf{L} + \mathbf{S}, \tag{2.16}$$

where, the quantum number **J** lies in the range $|L - S| \leq J \leq L + S$, the magnitude of **J** is $\sqrt{J(J+1)}\hbar$ and the eigenvalue of J_z is $m_J\hbar$. In the case of Rb the outermost shell has only one unpaired electron and so $S = 1/2$. In the ground state (5S) $L = 0$ and therefore the orbital angular momentum is $J = 1/2$. For the first excited state (5P), the orbital angular momentum is $L = 1$ and therefore value of J are 1/2 or 3/2. The energy shift of the levels is dependent on the value of J and thus, the $L = 0 \rightarrow L = 1$ transition (D line) is split into two transitions (D_1 line transition $5^2S_{1/2} \rightarrow 5^2P_{1/2}$ and D_2 line transition $5^2S_{1/2} \rightarrow 5^2P_{3/2}$).

2.3.2 Hyperfine structure

Hyperfine structure arises from both the electron-nucleus interaction, and the nuclear quadrupole interaction (i.e., the coupling of total electron angular momentum **J** with the total nucleus angular momentum **I**). The total angular momentum is expressed as follows:

$$\mathbf{F} = \mathbf{J} + \mathbf{I}, \tag{2.17}$$

where, the quantum number **F** lies in the range $|J - I| \leq F \leq J + I$. For example, in ^{87}Rb the total nucleus angular momentum is $I = 3/2$, $J = 1/2$ for the ground state and F takes values 1 or 2. For the first excited state of D_1 line ($5P_{1/2}$), $J = 1/2$ and F will take values 1 or 2 while for the D_2 line ($5P_{3/2}$), $J = 3/2$ and F takes values 0, 1, 2 or 3. In ^{85}Rb the total nucleus angular momentum is $I = 5/2$, $J = 1/2$ for ground state and F takes values 2 or 3. For the first excited state of D_1 line ($5P_{1/2}$), $J = 1/2$ and F takes values 2 or 3 while for the D_2 line ($5P_{3/2}$), $J = 3/2$ and F

takes values 1, 2, 3 or 4. Note, the F values corresponding to the 6P state takes same values as the F values corresponding to the 5P state since the values of J are the same in both cases. For example, F takes values 0, 1, 2 or 3 for the $6P_{3/2}$ state in ^{87}Rb or F takes values 2 or 3 for the $6P_{1/2}$ state in ^{85}Rb.

The above hyperfine interactions for the electron-nuclear system is given by the Hamiltonian of the form:

$$\mathrm{H_{hfs}} = \mathrm{A_{hfs}}\mathbf{I.J} + \mathrm{B_{hfs}}\frac{3(\mathbf{I.J})^2 + \frac{3}{2}(\mathbf{I.J}) - I(I+1)J(J+1)}{2I(2I-1)J(2J-1)}, \tag{2.18}$$

where, $\mathrm{A_{hfs}}$ is the magnetic dipole hyperfine constant, $\mathrm{B_{hfs}}$ is the electric quadrupole hyperfine constant, I is the total nuclear angular momentum, J is the total electronic angular momentum. Note, the magnetic octupole hyperfine interaction is not included in the expression of the Hamiltonian since it is about four orders of magnitude weaker than $\mathrm{A_{hfs}}$ and $\mathrm{B_{hfs}}$ [74, 75]. The hyperfine splitting interval from F to F-1 is expressed in terms of hyperfine constants as follows:

$$\begin{aligned} \Delta\mathcal{V}_{\mathrm{hfs}}(\mathrm{F} \rightarrow \mathrm{F}-1) &= (\Delta\mathrm{E_{hfs}}(\mathrm{F}) - \Delta\mathrm{E_{hfs}}(\mathrm{F}-1))/h \\ &= \mathrm{A_{hfs}F} + \mathrm{B_{hfs}}\frac{\frac{3}{2}\mathrm{F}\{\mathrm{F}^2 - \mathrm{I(I+1)} - \mathrm{J(J+1)} + \frac{1}{2}\}}{\mathrm{I(2I-1)J(2J-1)}}, \end{aligned} \tag{2.19}$$

where, h is Planck's constant and the hyperfine energy shift $\Delta\mathrm{E_{hfs}}$ is defined as:

$$\Delta\mathrm{E_{hfs}} = \frac{1}{2}h\mathrm{A_{hfs}K} + h\mathrm{B_{hfs}}\frac{\frac{3}{2}\mathrm{K(K+1)} - 2\mathrm{I(I+1)J(J+1)}}{4\mathrm{I(2I-1)J(2J-1)}}, \tag{2.20}$$

where, $\mathrm{K = F(F+1) - I(I+1) - J(J+1)}$. The electric quadrupole hyperfine constant $\mathrm{B_{hfs}} = 0$ for $\mathrm{I,\ J} \leq 1$ and therefore, the magnetic dipole hyperfine constant $\mathrm{A_{hfs}}$ of the $\mathrm{D_1}$ line ($5\mathrm{P}_{1/2}$) is expressed as follows:

$$\mathrm{A_{hfs}} = \frac{\Delta\mathcal{V}_{\mathrm{hfs}}(\mathrm{F} \rightarrow \mathrm{F}-1)}{\mathrm{F}}, \tag{2.21}$$

where, F = 2 in the case of ^{87}Rb and F = 3 for ^{85}Rb isotopes respectively. For the

D_2 line ($5P_{3/2}$), the following set of equations are solved in the case of ^{87}Rb:

$$\begin{aligned}
\Delta\mathcal{V}_{\mathrm{hfs}}(\mathrm{F}=3\rightarrow\mathrm{F}=2) &= 3\mathrm{A}_{\mathrm{hfs}}+\mathrm{B}_{\mathrm{hfs}},\\
\Delta\mathcal{V}_{\mathrm{hfs}}(\mathrm{F}=2\rightarrow\mathrm{F}=1) &= 2\mathrm{A}_{\mathrm{hfs}}-\mathrm{B}_{\mathrm{hfs}},\\
\Delta\mathcal{V}_{\mathrm{hfs}}(\mathrm{F}=1\rightarrow\mathrm{F}=0) &= \mathrm{A}_{\mathrm{hfs}}-\mathrm{B}_{\mathrm{hfs}}. \qquad (2.22)
\end{aligned}$$

For ^{85}Rb the following are the set of equations:

$$\begin{aligned}
\Delta\mathcal{V}_{\mathrm{hfs}}(\mathrm{F}=4\rightarrow\mathrm{F}=3) &= 4\mathrm{A}_{\mathrm{hfs}}+\frac{4}{5}\mathrm{B}_{\mathrm{hfs}},\\
\Delta\mathcal{V}_{\mathrm{hfs}}(\mathrm{F}=3\rightarrow\mathrm{F}=2) &= 3\mathrm{A}_{\mathrm{hfs}}-\frac{9}{20}\mathrm{B}_{\mathrm{hfs}},\\
\Delta\mathcal{V}_{\mathrm{hfs}}(\mathrm{F}=2\rightarrow\mathrm{F}=1) &= 2\mathrm{A}_{\mathrm{hfs}}-\frac{4}{5}\mathrm{B}_{\mathrm{hfs}}. \qquad (2.23)
\end{aligned}$$

3

Nature of interference between excitation paths associated with AT peaks in multilevel system

3.1 Introduction

This chapter describes a theoretical frame work to identify the role and the nature of interference between the excitation paths associated with Autler-Townes (AT) peaks in generic multi-level system. AT peaks are spectroscopic features which arise from a transition between a pair of transitions of the dressed states. The dressed states on the other hand, refers to particular energy levels which are created by the pump/control laser(s). The destructive interference between the excitation paths associated with AT peaks, give rise to sharp transparency window known as electromagnetically induced transparency (EIT). In three-level system, the excitation paths associated with the two AT peaks interferes pair-wise, almost similar to the two-slit interference. In four-level system, the interference between the excitation paths associated with the three AT peaks is also pair-wise analogous to three-slit interference but has a bit more complicated nature of interference. However, in many practical situations in atomic systems only the simple form of interference similar to three-level system dominates. In the three-level system, the nature of interference (i.e., constructive, destructive or no interference) between the excitation paths associated with the two AT peaks is purely determined by the natural decay rate of the states coupled by the control laser. However, in four-level system the nature of interference between the excitation paths associated with the two extreme AT peaks can be tuned from constructive to destructive by tuning the power of the control laser.

The first section of the chapter discuses a generic theoretical frame work for probe absorption in the dressed state approach and the transfer of coherence approach. The derived formula of the probe absorption using the dressed state approach, is used in subsequent sections to analyze the nature of interference between the excitation paths associated with AT peaks for a variety of systems.

3.2 The theoretical model

3.2.1 Dressed state approach

We consider the generic system as shown in Fig. 3.1, in which a weak probe laser is driving the transition $|1\rangle \rightarrow |2\rangle$ with Rabi frequency Ω_{12} and the detuning δ_{12} (note, the detuning is defined as $\delta_{i-1,i} = \omega^{l}_{i-1,i} \mp (\omega_i - \omega_{i-1})$ if $\omega_i > \omega_{i-1}$ and $\omega_i < \omega_{i-1}$ respectively, where $\omega^{l}_{i-1,i}$ is the frequency of the laser, ω_i and ω_{i-1} are the frequency of the energy levels). The strong control lasers are driving the transitions $|2\rangle \leftrightarrow |3\rangle$, $|3\rangle \leftrightarrow |4\rangle, \cdots, |n-1\rangle \leftrightarrow |n\rangle$ with detunings δ_{23}, $\delta_{34}, \cdots, \delta_{n-1,n}$ and the Rabi frequencies Ω_{23}, $\Omega_{34}, \cdots, \Omega_{n-1,n}$. The Hamiltonian associated only with the control lasers in the rotating frame with rotating wave approximation is given as:

$$\begin{aligned} H_c = &-\hbar\delta_{23}|3\rangle\langle 3| - \hbar(\delta_{23} \pm \delta_{34})|4\rangle\langle 4| - \cdots - \hbar(\delta_{23} \pm \delta_{34} \pm \cdots \pm \delta_{n-1,n})|n\rangle\langle n| \\ &+ \left\{ \frac{\hbar\Omega_{23}}{2}|2\rangle\langle 3| + \frac{\hbar\Omega_{34}}{2}|3\rangle\langle 4| + \cdots + \frac{\hbar\Omega_{n-1,n}}{2}|n-1\rangle\langle n| + \mathrm{H.c.} \right\}, \end{aligned} \tag{3.1}$$

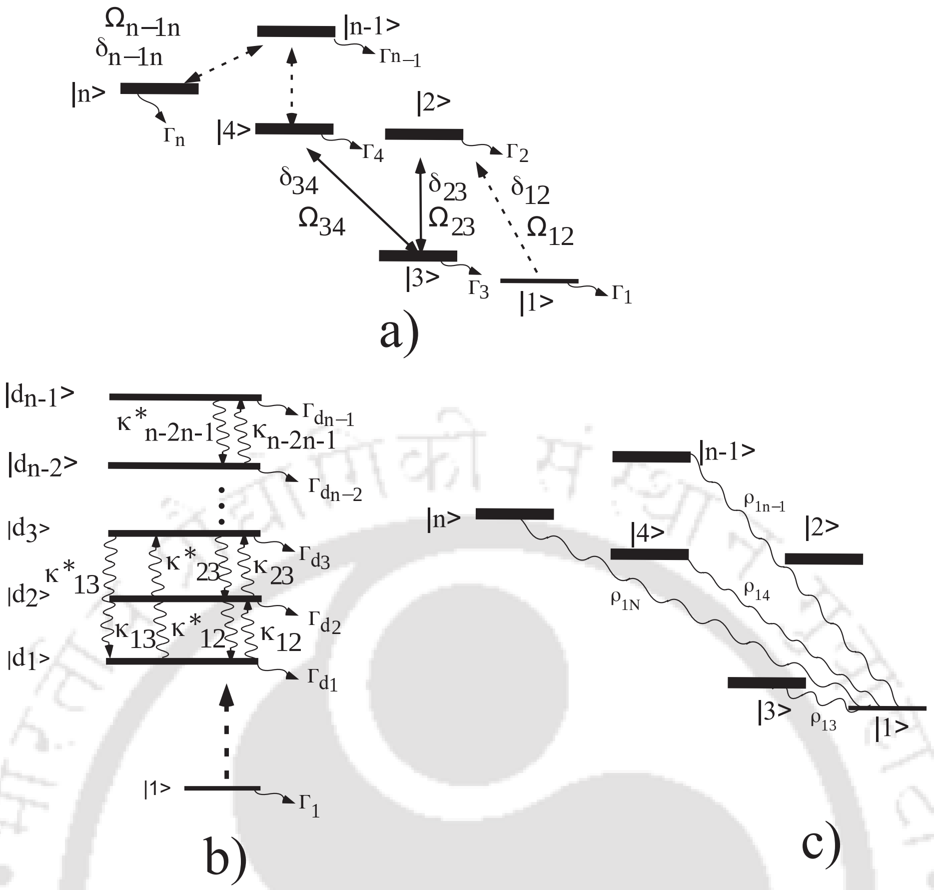

Fig. 3.1: The general n-level atomic system: a) Bare atomic state picture. b) Dressed state picture. c) Transfer of coherence shown by curly line between various levels not directly driven by the lasers

where, H.c. is Hermitian conjugate. The sign ± of $\delta_{i-1,i}$ is chosen according to the level structure. If the energy of the state $|i\rangle$ is higher than the state $|i-1\rangle$, then $\delta_{i-1,i}$ will have + sign and if the energy of the state $|i\rangle$ is lower than the state $|i-1\rangle$, then $\delta_{i-1,i}$ will have - sign. For example, if the two control lasers form a ladder system, the two photon detuning is given as $\delta_{23} + \delta_{34}$ and if they form a lambda system the two photon detuning is $\delta_{23} - \delta_{34}$. Similarly the two photon detuning of a Vee system (which is an inverted lambda system) is also $\delta_{23} - \delta_{34}$. This in general gives $\delta_{23} \pm \delta_{34}$, hence the ± sign. The eigenvalues ($E_{d_i} = \hbar\Delta_{d_i}$) of the H_c determines the position of the dressed states ($|d_i\rangle$) and hence the position of the AT absorption peaks. The eigenvectors will determine the dressed states which is a linear combination of the bare atomic states.

The transformation from the bare states, $|\Psi_B\rangle$ (i.e., $|1\rangle, |2\rangle, \cdots, |n\rangle$) to dressed state (similar to Morris-Shore transformation [76]), $|\Psi_D\rangle$ is given by the unitary matrix U of dimension $(n-1)\times(n-1)$ i.e.,

$$|\Psi_D\rangle = \hat{U}\,|\Psi_B\rangle\,. \tag{3.2}$$

The general element ij $(i = 1, \cdots, n-1,\ j = 2, \cdots, n)$ of this unitary matrix is u_{ij} and the generic form of the i^{th} $(i = 1, \cdots, n-1)$ dressed state $|d_i\rangle$ is,

$$|d_i\rangle = u_{i2}\,|2\rangle + u_{i3}\,|3\rangle + \cdots + u_{in}\,|n\rangle\,. \tag{3.3}$$

If the total decay rate of the bare atomic state $|i\rangle$ is Γ_i, the decay matrix $\hat{\Gamma}$ in the bare state can easily be written as,

$$\hat{\Gamma} = \sum_{i=2}^{n} \frac{\Gamma_i}{2}\,|i\rangle\,\langle i|\,. \tag{3.4}$$

This decay matrix, $\hat{\Gamma}$ will transform in the dressed state basis as $\hat{U}\hat{\Gamma}\hat{U}^{\dagger}$. The general ij^{th} element of this matrix, $\kappa_{ij}(=\langle i|\,\hat{U}\hat{\Gamma}\hat{U}^{\dagger}\,|j\rangle)$ will be,

$$\kappa_{ij} = \frac{1}{2}(u_{i2}^{*}u_{j2}\Gamma_2 + u_{i3}^{*}u_{j3}\Gamma_3 + \cdots + u_{in}^{*}u_{jn}\Gamma_n). \tag{3.5}$$

The diagonal elements, $\kappa_{ii}(=\Gamma_{d_i})$ of this matrix corresponds to incoherent decay of the dressed states $|d_i\rangle$ and contributes to AT absorption peaks linewidth,

$$\Gamma_{d_i} = \frac{1}{2}(|u_{i2}|^2\Gamma_2 + |u_{i3}|^2\Gamma_3 + \cdots + |u_{in}|^2\Gamma_n). \tag{3.6}$$

The coherent decay terms κ_{ij} gives rise to interference between the excitation paths of the dressed states. Note that if $\Gamma_i(=\Gamma)$ is the same for all bare states, $\kappa_{ij} = \langle i|\,\hat{U}\hat{\Gamma}\hat{U}^{\dagger}\,|j\rangle = \frac{\Gamma}{2}\,\langle i|\,\hat{U}\hat{1}\hat{U}^{\dagger}\,|j\rangle = 0$ for $i \neq j$. In this case there will be no interference between the excitation paths of the dressed states. This might not be clearly evident in the bare state density matrix approach.

The dressed states $|d_i\rangle$ couples with $|1\rangle$ through the probe laser with a coupling strength $\Omega_{p_i} = -\langle 1|\vec{D}.\vec{E}^0_{12}|d_i\rangle/\hbar$ where, $\vec{E}^0_{12}$ is the electric field amplitude associated with the probe laser and $\vec{D}$ is the electric dipole moment operator. With the rotating wave approximation $\langle 1|\vec{D}.\vec{E}^0_{12}|d_i\rangle/\hbar = \langle 1|\vec{D}.\vec{E}^0_{12}u_{i2}|2\rangle/\hbar$ and hence $\Omega_{p_i} = u_{i2}\Omega_{12}$. The amplitude of the excitation path for AT peaks corresponding to the dressed states $|d_i\rangle$ will be proportional to the Ω_{p_i}. The amplitude for the probe absorption corresponding to this peak will be proportional to $|\Omega_{p_i}|^2$.

The equation of motion for the dressed states $|d_i\rangle$ and the bare state $|1\rangle$ is:

$$i\frac{d}{dt}\begin{bmatrix} C_1 \\ C_{d_1} \\ . \\ . \\ C_{d_{n-1}} \end{bmatrix} = \begin{bmatrix} 0 & \frac{\Omega_{p_1}}{2} & \frac{\Omega_{p_2}}{2} & .. & \frac{\Omega_{p_{n-1}}}{2} \\ \frac{\Omega^*_{p_1}}{2} & -i\gamma_{d_1} & -i\kappa_{12} & .. & -i\kappa_{1,n-1} \\ & . & & & \\ & . & & & \\ \frac{\Omega^*_{p_{n-1}}}{2} & -i\kappa^*_{1n} & -i\kappa^*_{2,n-1} & .. & -i\gamma_{d_{n-1}} \end{bmatrix} \begin{bmatrix} C_1 \\ C_{d_1} \\ . \\ . \\ C_{d_{n-1}} \end{bmatrix}, \tag{3.7}$$

where, $\gamma_{d_i} = \frac{\Gamma_1}{2} + \Gamma_{d_i} + i\delta_{d_i}$ with $\delta_{d_i} = \delta_{12} + \Delta_{d_i}$. We consider the steady state for the dynamics of all the dressed states $|d_i\rangle$ i.e., $\frac{dC_{d_i}}{dt} = 0$. The absorption of the probe laser is given by the rate of loss of population in state $|1\rangle$ which is expressed as, $\frac{d|C_1|^2}{dt} = \frac{dC_1^*}{dt}C_1 + \frac{dC_1}{dt}C_1^*$. For the weak probe we consider $C_1 \approx 1$ and probe absorption is now given as $\frac{d|C_1|^2}{dt} = \frac{dC_1^*}{dt} + \frac{dC_1}{dt}$. The absorption of the probe laser is normalized as $-\{(\Gamma_1+\Gamma_2)/(2|\Omega_{12}|^2)\}(\frac{dC_1^*}{dt} + \frac{dC_1}{dt})$ so that in the absence of all the control lasers, probe absorption is 1 at resonance ($\delta_{12} = 0$). The absorption coefficient is given by the normalized absorption times the optical thickness of the medium, σnl (where, $\sigma = 3\lambda^2/2\pi$ is the on-resonance scattering cross-section, λ is the wavelength of the probe, n is the atomic density and l is the length of the medium) i.e., $-\{(\Gamma_1+\Gamma_2)/(2|\Omega_{12}|^2)\}(\frac{dC_1^*}{dt} + \frac{dC_1}{dt})\{3\lambda^2 nl/2\pi\}$.

3.2.2 Bare state TOC approach

The other approach which is commonly used to analyze the absorption of the probe laser in a multilevel system is the transfer of coherence (TOC) between the bare states using density matrix formalism [77] and is derived in appendix A for completeness. The absorption of the probe laser is written in terms of the density matrix element between level $|1\rangle$ and $|2\rangle$ (i.e., ρ_{12} given in Eq. A.6). In the weak probe regime, all the population will be pumped to state $|1\rangle$, i.e., $\rho_{11} \approx 1$ and Eq. A.6 reduces as follows:

$$\rho_{12} = \cfrac{\frac{i}{2}\frac{\Omega_{12}}{\gamma_{12}}}{1+\cfrac{\frac{1}{4}\frac{|\Omega_{23}|^2}{\gamma_{12}\gamma_{13}}}{1+\cfrac{\frac{1}{4}\frac{|\Omega_{34}|^2}{\gamma_{13}\gamma_{14}}}{1+\cfrac{\frac{1}{4}\frac{|\Omega_{45}|^2}{\gamma_{14}\gamma_{15}}}{1+\cfrac{\frac{1}{4}\frac{|\Omega_{56}|^2}{\gamma_{15}\gamma_{16}}}{1+\cfrac{.}{1+\cfrac{.}{1+\frac{1}{4}\frac{|\Omega_{n-1,n}|^2}{\gamma_{1,n-1}\gamma_{1,n}}}}}}}}}, \tag{3.8}$$

where,

$$\gamma_{1j} = \frac{\Gamma_1+\Gamma_j}{2} - i\sum_{i=1}^{j-1}(-1)^{i+1}\delta_{i,i+1} \tag{3.9}$$

is the decoherence rate of transferred coherence between $|1\rangle$ and $|j\rangle$ of ρ_{1j}. The normalized absorption of the probe laser is given as $\frac{\Gamma_1+\Gamma_2}{\Omega_{12}}\rho_{12}$ so that absorption of the resonant probe laser is 1 in the absence of the control lasers. The validity of the dressed state approach is tested by comparing the probe absorption in the two approaches. The absorption of the probe completely match in the two approaches for various number of levels and of various type of systems for different atomic and control laser parameters. For example, the probe absorption of the five-level system for the parameters given in the annotation is as shown in Fig. 3.2.

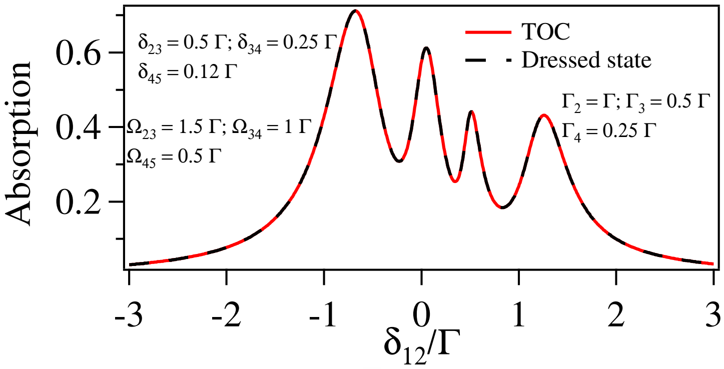

Fig. 3.2: Comparison of the probe absorption obtained using TOC and dressed state approach for a five-level atomic system.

3.3 The nature of interference in the multi-level systems

3.3.1 Three-level system

The nature of interference in the three-level system has been addressed in earlier works [13, 78, 79, 80, 81, 82, 83], however, we present this system here for completeness and in a comprehensive way for the rest of the work. We consider the three-level systems shown in Fig. 3.3, in which a strong control laser is driving the transition $|2\rangle \leftrightarrow |3\rangle$ and a weak probe laser is driving the transition $|1\rangle \rightarrow |2\rangle$. The detuning of the probe laser and the control laser is δ_{12} and δ_{23} respectively in the bare atomic state picture. The Rabi frequency of the probe laser is Ω_{12} and the control laser is Ω_{23}. The strong control laser creates dressed states whose position is determined by the eigenvalues of the Hamiltonian associated with the control laser,

$$H_c = \hbar \begin{bmatrix} 0 & \frac{\Omega_{23}}{2} \\ \frac{\Omega_{23}^*}{2} & -\delta_{23} \end{bmatrix}. \tag{3.10}$$

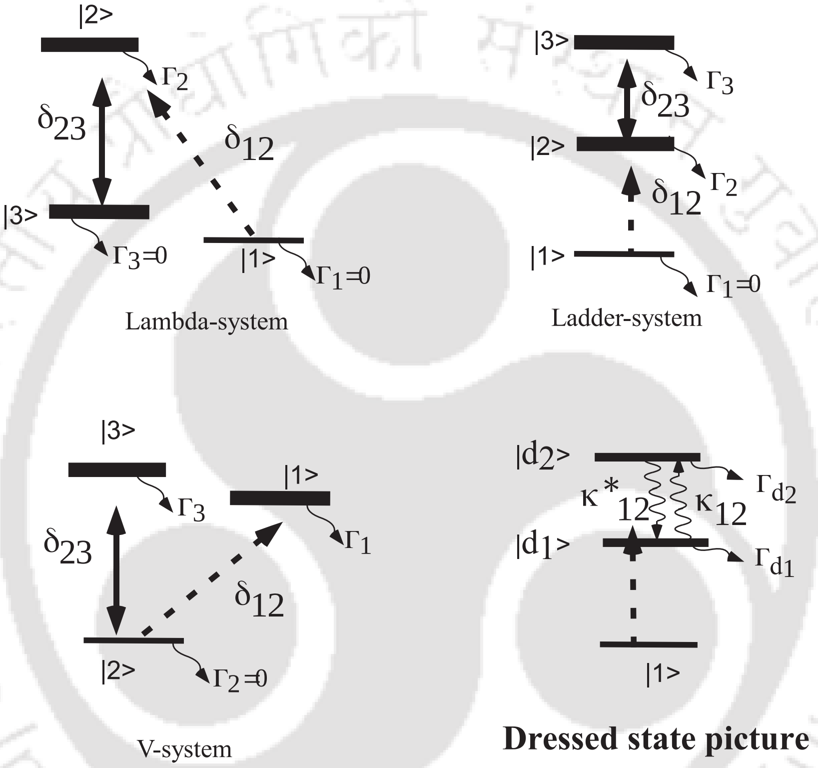

Fig. 3.3: Three level atomic system: a) Bare atomic state picture. b) Dressed state picture
.

Using Eq. 3.7, the equation of motion for the coefficients of $|1\rangle$, $|d_1\rangle$ and $|d_2\rangle$ are given as,

$$\begin{aligned} i\frac{dC_1}{dt} &= \frac{\Omega_{p1}}{2}C_{d_1} + \frac{\Omega_{p2}}{2}C_{d_2}, \\ i\frac{dC_{d_1}}{dt} &= \frac{\Omega^*_{p1}}{2}C_1 - i\gamma_{d_1}C_{d_1} - i\kappa_{12}C_{d_2}, \\ i\frac{dC_{d_2}}{dt} &= \frac{\Omega^*_{p2}}{2}C_1 - i\kappa^*_{12}C_{d_1} - i\gamma_{d_2}C_{d_2}. \end{aligned} \tag{3.11}$$

Considering the steady state case for the time evolution of the dressed states i.e., $\frac{dC_{d_1}}{dt} = \frac{dC_{d_2}}{dt} = 0$, the following equation which is proportional to probe absorption is obtained:

$$\frac{dC_1}{dt} = -\underbrace{\frac{1/4}{1-\frac{|\kappa_{12}|^2}{\gamma_{d_1}\gamma_{d_2}}}}_{\text{Normalization}}\left[\underbrace{\frac{|\Omega_{p_1}|^2}{\gamma_{d_1}} + \frac{|\Omega_{p_2}|^2}{\gamma_{d_2}}}_{\text{AT peaks}} - \underbrace{\frac{\kappa_{12}\Omega^*_{p_1}\Omega_{p_2} + c.c}{\gamma_{d_1}\gamma_{d_2}}}_{\text{Interference}}\right]. \tag{3.12}$$

The eigenvalues of the two dressed states $|d_1\rangle$ and $|d_2\rangle$ corresponding to the Hamiltonian in Eq. 3.10 and the various parameters are given as follows:

$$\begin{aligned} E_{d_1} =& \frac{\hbar}{2}[-\delta_{23} - \sqrt{\delta_{23}^2 + \Omega_{23}^2}], \\ |d_1\rangle =& \frac{1}{\sqrt{\Omega_{23}^2 + (\delta_{23} - \sqrt{\delta_{23}^2 + \Omega_{23}^2})^2}}((\delta_{23} - \sqrt{\delta_{23}^2 + \Omega_{23}^2})\,|2\rangle + \Omega_{23}\,|3\rangle) \\ =& \cos\theta\,|2\rangle + \sin\theta\,|3\rangle\,, \\ \Gamma_{d_1} =& \frac{1}{2}(\cos^2\theta\Gamma_2 + \sin^2\theta\Gamma_3), \quad E_{d_2} = \frac{\hbar}{2}[-\delta_{23} + \sqrt{\delta_{23}^2 + \Omega_{23}^2}], \\ |d_2\rangle =& \frac{1}{\sqrt{\Omega_{23}^2 + (\delta_{23} + \sqrt{\delta_{23}^2 + \Omega_{23}^2})^2}}((\delta_{23} + \sqrt{\delta_{23}^2 + \Omega_{23}^2})\,|2\rangle + \Omega_{23}\,|3\rangle) \\ =& -\sin\theta\,|2\rangle + \cos\theta\,|3\rangle\,, \\ \Gamma_{d_2} =& \frac{1}{2}(\sin^2\theta\Gamma_2 + \cos^2\theta\Gamma_3), \quad \kappa_{12} = -\frac{1}{4}(\Gamma_2 - \Gamma_3)\sin 2\theta, \\ \Omega_{p_1} =& \Omega_{12}\cos\theta, \quad \Omega_{p_2} = -\Omega_{12}\sin\theta, \end{aligned} \tag{3.13}$$

where,

$$\tan 2\theta = -\frac{\Omega_{23}}{\delta_{23}} \quad (\text{i.e.,} \quad \sin 2\theta = -\frac{\Omega_{23}}{\sqrt{\delta_{23}^2+\Omega_{23}^2}} \quad \text{and} \quad \cos 2\theta = \frac{\delta_{23}}{\sqrt{\delta_{23}^2+\Omega_{23}^2}}),$$

and the unitary transformation in Eq. 3.2 is thus expressed as:

$$\begin{pmatrix} |d_1\rangle \\ |d_2\rangle \end{pmatrix} = \begin{pmatrix} \cos\theta & \sin\theta \\ -\sin\theta & \cos\theta \end{pmatrix} \begin{pmatrix} |2\rangle \\ |3\rangle \end{pmatrix}.$$

The coherent decay κ_{ij} and the incoherent decay $\kappa_{ii} = \Gamma_{d_i}$ are determined using the unitary transformation of the decay matrix, $\hat{\Gamma}$ given in Eq. 3.4 (i.e., $\hat{U}\hat{\Gamma}\hat{U}^\dagger$) as follows,

$$\begin{pmatrix} \cos\theta & \sin\theta \\ -\sin\theta & \cos\theta \end{pmatrix} \begin{pmatrix} \Gamma_2 & 0 \\ 0 & \Gamma_3 \end{pmatrix} \begin{pmatrix} \cos\theta & -\sin\theta \\ \sin\theta & \cos\theta \end{pmatrix}$$
$$= \begin{pmatrix} \frac{1}{2}(\cos^2\theta\Gamma_2 + \sin^2\theta\Gamma_3) & -\frac{1}{4}(\Gamma_2-\Gamma_3)\sin 2\theta \\ -\frac{1}{4}(\Gamma_2-\Gamma_3)\sin 2\theta & \frac{1}{2}(\sin^2\theta\Gamma_2 + \cos^2\theta\Gamma_3) \end{pmatrix}.$$

The diagonal elements of this matrix gives $\kappa_{ii} = \Gamma_{d_i}, i = 1, 2$ and the off-diagonal elements gives κ_{12}. In terms of θ parameters given in Eq. 3.13, Eq. 3.12 is also written as follows,

$$\frac{dC_1}{dt} = -\underbrace{\frac{|\Omega_{12}|^2/4}{1-\frac{|\kappa_{12}|^2}{\gamma_{d_1}\gamma_{d_2}}}}_{\text{Normalization}} \left[\underbrace{\frac{\cos^2\theta}{\gamma_{d_1}} + \frac{\sin^2\theta}{\gamma_{d_2}}}_{\text{AT peaks}} - \underbrace{\frac{\Gamma_2-\Gamma_3}{4}\frac{\sin^2 2\theta}{\gamma_{d_1}\gamma_{d_2}}}_{\text{Interference}} \right]. \tag{3.14}$$

For the three-level system, Eq. 3.8 for TOC approach is reduced as follows,

$$\rho_{12} = \frac{\frac{i}{2}\frac{\Omega_{12}}{\gamma_{12}}}{1+\frac{1}{4}\frac{|\Omega_{23}|^2}{\gamma_{12}\gamma_{13}}} \quad . \tag{3.15}$$

The comparison of probe absorption using Eq. 3.14 (or Eq. 3.12) and Eq. 3.15 for the two approaches shows a complete match for the various parameters.

The nature of interference between the excitation paths of the two dressed states $|d_1\rangle$ and $|d_2\rangle$ is determined by the parameter κ_{12}. The interference parameter κ_{12} given in Eq. 3.13 can change its sign for a given Γ_2 and Γ_3 by tuning the control laser detuning (δ_{23}) from positive to negative and vice versa. However, in the interference term of Eq. 3.14, the minimum value of $\sin^2 2\theta$ is 0 and the maximum is 1 as the detuning of the control laser is changed. Therefore, the interference term will not change sign even though the interference parameter κ_{12} changes its sign. It is not possible therefore to change the sign of interference by changing the detuning of the control laser for a three-level system.

From Eq. 3.14, the interference between the excitation paths associated with the AT peaks is destructive when $\Gamma_2 > \Gamma_3$, or no interference when $\Gamma_2 = \Gamma_3$, or is constructive when $\Gamma_2 < \Gamma_3$ (see also Fig. 3.4). For $\Gamma_3 = 0$ which is the case for a Λ-system, the destructive interference completely cancel out the absorption of the two AT peaks at resonance (see Fig. 3.4a). In Fig. 3.4b with $\Gamma_3 = 0.5\Gamma_2$ ($\Gamma_2 - \Gamma_3 > 0$) which is valid for the ladder system, the interference is partially destructive as there is a finite absorption for the solid red curve at resonance. For $\Gamma_2 = \Gamma_3$ there is no interference between the excitation paths associated with the two AT peaks as the dashed green curve is superimposed on the solid red curve in Fig. 3.4c. For $\Gamma_2 \ll \Gamma_3$ which is valid for a V-system, the interference is constructive as the dashed green curve is lower than the solid red curve at resonance (see Fig. 3.4d). From Eq. 3.14 the minimum value of $\sin^2 2\theta$ in the interference term is 0 and the maximum value is 1 as the laser parameters (Ω_{23} and δ_{23}) are changed. Hence, the nature of interference between the excitation paths associated with the two AT peaks can not be tuned from constructive to destructive interference for the given atomic levels by tuning the laser parameters.

Note that in a V-system, the presence of the control laser will cause population transfer. However, in order to study the nature of interference we can ignore population transfer. The population transfer will modify the overall amplitude of absorption but the lineshape will remain the same. The ladder system in Sr using

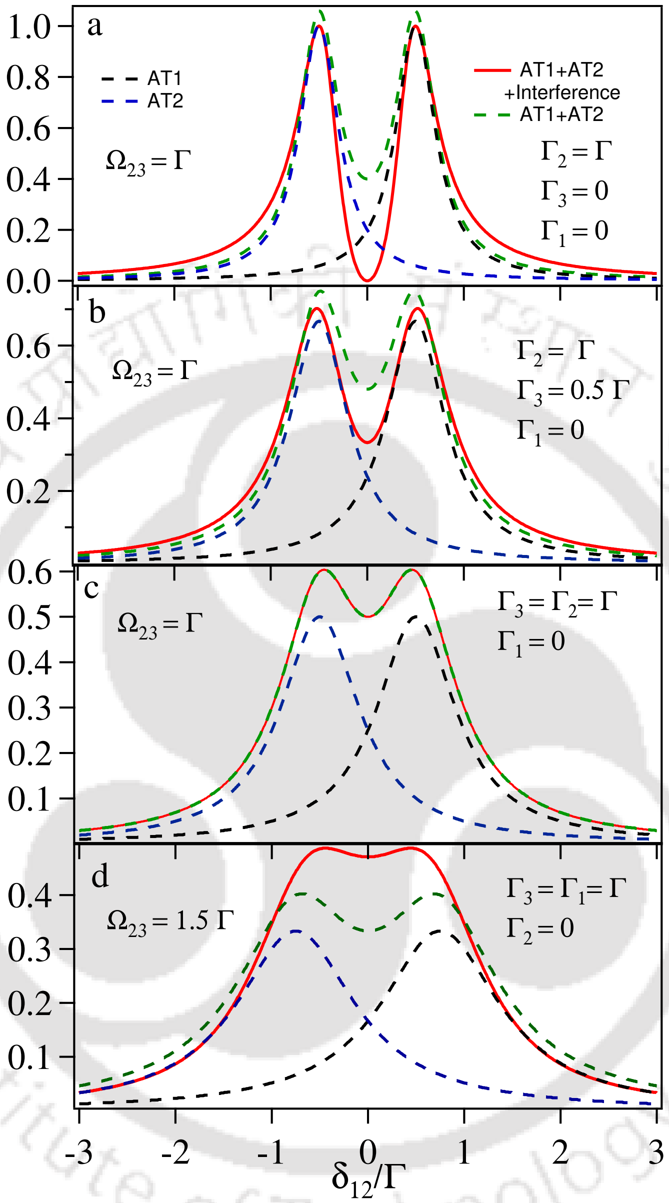

Fig. 3.4: AT peaks and the effect of interference for probe absorption vs its detuning (δ_{12}/Γ) with control laser detuning, $\delta_{23}=0$ i.e., $\theta=\frac{\pi}{4}$ and $\Omega_{p_1}=-\frac{1}{\sqrt{2}}, \Omega_{p_2}=\frac{1}{\sqrt{2}}$ a) Λ-system: $\kappa_{12}=-\frac{\Gamma}{4}, \Gamma_{d_1}=\Gamma_{d_2}=\frac{\Gamma}{4}$ b) ladder system: $\kappa_{12}=-\frac{\Gamma}{8}, \Gamma_{d_1}=\Gamma_{d_2}=\frac{3\Gamma}{8}$ c) ladder system: $\kappa_{12}=0, \Gamma_{d_1}=\Gamma_{d_2}=\frac{\Gamma}{2}$ d) V-system: $\kappa_{12}=-\frac{\Gamma}{4}, \Gamma_{d_1}=\Gamma_{d_2}=\frac{\Gamma}{4}$.

$(5s^2)^1S_0, |1\rangle \leftrightarrow (5s5p)^3P_1, |2\rangle \leftrightarrow (5s6s)^3S_1, |3\rangle$ with decay parameters $\Gamma_2 = 2\pi \times 7.5$ kHz and $\Gamma_3 = 2\pi \times 16$ MHz is having $\Gamma_2 \ll \Gamma_3$ [32]. This parameter system is very similar to a V-system. In the ladder system, population transfer due to a weak probe laser can be ignored. A similar parameter system is also possible in Yb atom.

3.3.2 Four-level system

The various four-level system have been studied for different applications in two configurations namely the chain configuration such as N [84, 85, 86], Ladder-Lambda [87, 88], Ladder [89], and the branching configuration such as Y [90], Tripod [91, 92, 93], Inverted Tripod [94] as shown in Fig. 3.5. Different names have been given for the four-level system depending upon the energy levels of $|1\rangle$, $|2\rangle$, $|3\rangle$ and $|4\rangle$ and other possible four-level systems can also be constructed by changing the energy levels. The dressed state picture of all possible four-level systems will be the same as shown in Fig. 3.5.

The response of the four level chain system to the weak probe laser in steady state is given by ρ_{12} element of the density matrix using the TOC between levels $|1\rangle$ and $|3\rangle$ and $|1\rangle$ and $|4\rangle$,

$$\rho_{12} = \frac{\frac{i}{2}\frac{\Omega_{12}}{\gamma_{12}}}{1 + \frac{\frac{1}{4}\frac{|\Omega_{23}|^2}{\gamma_{12}\gamma_{13}}}{1+\frac{1}{4}\frac{|\Omega_{34}|^2}{\gamma_{13}\gamma_{14}}}}. \tag{3.16}$$

For the branching configuration system, branching at level $|2\rangle$ the above equation will have the following form,

$$\rho_{12} = \frac{\frac{i}{2}\frac{\Omega_{12}}{\gamma_{12}}}{1 + \frac{1}{4}\frac{|\Omega_{23}|^2}{\gamma_{12}\gamma_{13}} + \frac{1}{4}\frac{|\Omega_{24}|^2}{\gamma_{12}\gamma_{13}}}. \tag{3.17}$$

The above density matrix solution given in Eq. 3.16 and 3.17 is a good cross check of

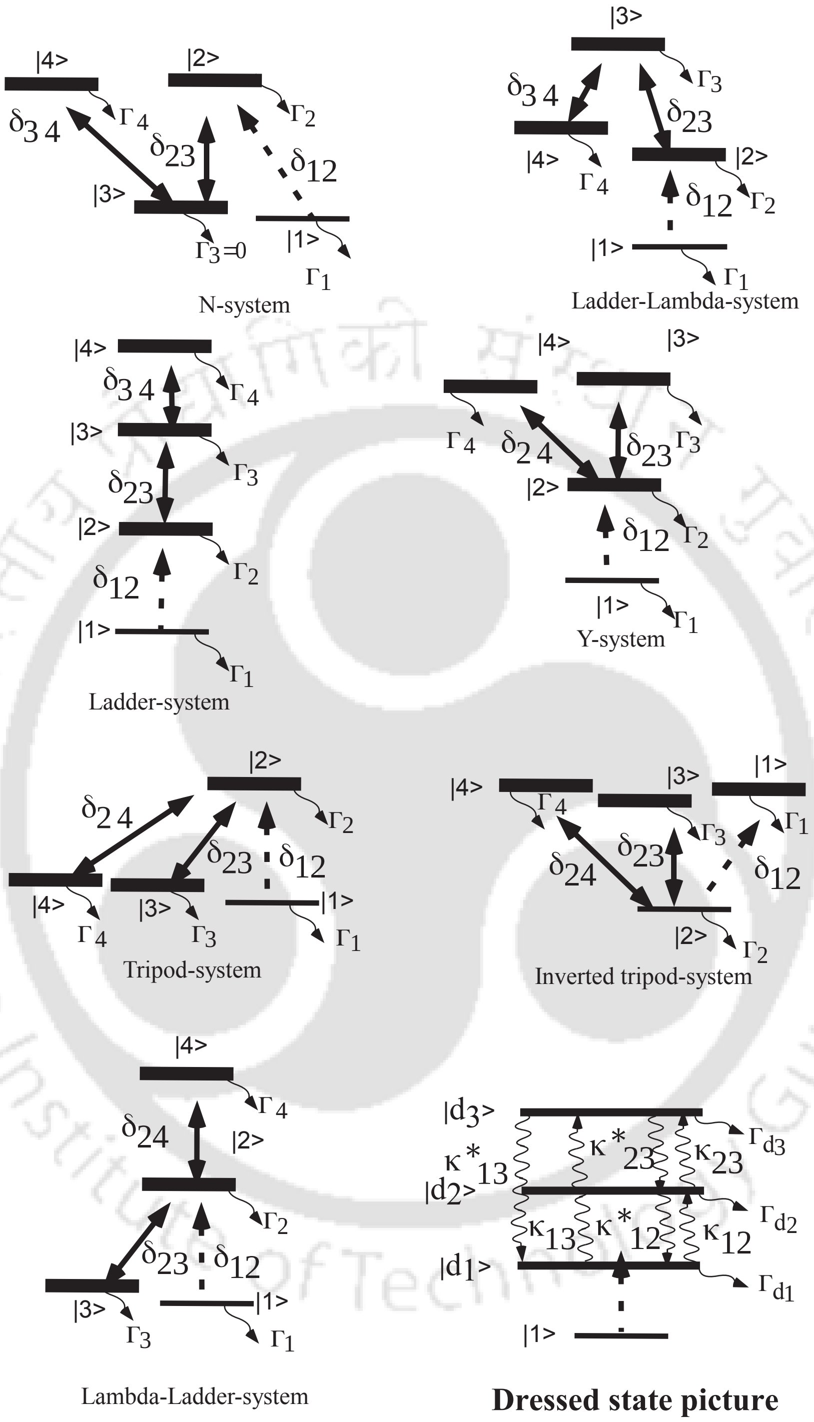

N-system

Ladder-Lambda-system

Ladder-system

Y-system

Tripod-system

Inverted tripod-system

Lambda-Ladder-system

Dressed state picture

Fig. 3.5: Four-level atomic system in bare and dressed state picture.

our calculation for the four-level system in the dressed state picture and identification of the nature of interference between the excitation paths associated with the various AT peaks. The Hamiltonian associated with the control lasers for the four-level chain system is written as,

$$H_c = \hbar \begin{bmatrix} 0 & \frac{\Omega_{23}}{2} & 0 \\ \frac{\Omega^*_{23}}{2} & -\delta_{23} & \frac{\Omega_{34}}{2} \\ 0 & \frac{\Omega^*_{34}}{2} & -(\delta_{23} \pm \delta_{34}) \end{bmatrix}. \tag{3.18}$$

Similarly, the Hamiltonian associated with the control lasers for the four-level system branching at level $|2\rangle$ such as Y, Tripod and Inverted Tripod is,

$$H_c = \hbar \begin{bmatrix} 0 & \frac{\Omega_{23}}{2} & \frac{\Omega_{24}}{2} \\ \frac{\Omega^*_{23}}{2} & -\delta_{23} & 0 \\ \frac{\Omega^*_{24}}{2} & 0 & -\delta_{24} \end{bmatrix}. \tag{3.19}$$

The rate equation for the bare state $|1\rangle$ and the dressed states $|d_1\rangle$, $|d_2\rangle$, $|d_3\rangle$ are given below:

$$\begin{aligned} i\frac{dC_1}{dt} &= \frac{\Omega_{p_1}}{2}C_{d_1} + \frac{\Omega_{p_2}}{2}C_{d_2} + \frac{\Omega_{p_3}}{2}C_{d_3}, \\ i\frac{dC_{d_1}}{dt} &= \frac{\Omega^*_{p_1}}{2}C_1 - i\gamma_{d_1}C_{d_1} - i\kappa_{12}C_{d_2} - i\kappa_{13}C_{d_3}, \\ i\frac{dC_{d_2}}{dt} &= \frac{\Omega^*_{p_2}}{2}C_1 - i\kappa^*_{12}C_{d_1} - i\gamma_{d_2}C_{d_2} - i\kappa_{23}C_{d_3}, \\ i\frac{dC_{d_3}}{dt} &= \frac{\Omega^*_{p_3}}{2}C_1 - i\kappa^*_{13}C_{d_1} - i\kappa^*_{23}C_{d_2} - i\gamma_{d_3}C_{d_3}. \end{aligned} \tag{3.20}$$

Considering the steady state case for the time evolution of the dressed states i.e., $\frac{dC_{d_1}}{dt} = \frac{dC_{d_2}}{dt} = \frac{dC_{d_3}}{dt} = 0$, the following equation which is proportional to probe absorption is obtained:

$$
\begin{aligned}
\frac{dC_1}{dt} = -\frac{1/4}{N}\Bigg[& \underbrace{\frac{|\Omega_{p_1}|^2}{\gamma_{d_1}} + \frac{|\Omega_{p_2}|^2}{\gamma_{d_2}} + \frac{|\Omega_{p_3}|^2}{\gamma_{d_3}}}_{\text{Three AT peaks}} \\
& \underbrace{-\frac{\kappa_{12}\Omega^*_{p_1}\Omega_{p_2} + c.c.}{\gamma_{d_1}\gamma_{d_2}} - \frac{\kappa_{23}\Omega^*_{p_2}\Omega_{p_3} + c.c.}{\gamma_{d_2}\gamma_{d_3}} - \frac{\kappa_{13}\Omega^*_{p_1}\Omega_{p_3} + c.c.}{\gamma_{d_1}\gamma_{d_3}}}_{\text{Interference1}} \\
& \underbrace{+\frac{\kappa_{12}\kappa_{23}\Omega^*_{p_1}\Omega_{p_3} + c.c.}{\gamma_{d_2}\gamma_{d_1}\gamma_{d_3}} + \frac{\kappa_{23}\kappa^*_{13}\Omega^*_{p_2}\Omega_{p_1} + c.c.}{\gamma_{d_3}\gamma_{d_2}\gamma_{d_1}} + \frac{\kappa^*_{13}\kappa_{12}\Omega^*_{p_3}\Omega_{p_2} + c.c.}{\gamma_{d_1}\gamma_{d_3}\gamma_{d_2}}}_{\text{Interference2}} \\
& \underbrace{-\frac{|\kappa_{12}|^2|\Omega_{p_3}|^2 + |\kappa_{23}|^2|\Omega_{p_1}|^2 + |\kappa_{13}|^2|\Omega_{p_2}|^2}{\gamma_{d_1}\gamma_{d_2}\gamma_{d_3}}}_{\text{Correction for AT peaks}}\Bigg],
\end{aligned}
\tag{3.21}
$$

where,

$$
N = 1 + \frac{[\kappa^*_{13}\kappa_{12}\kappa_{23} + c.c.]}{\gamma_{d_1}\gamma_{d_2}\gamma_{d_3}} - \frac{|\kappa_{12}|^2}{\gamma_{d_1}\gamma_{d_2}} - \frac{|\kappa_{23}|^2}{\gamma_{d_2}\gamma_{d_3}} - \frac{|\kappa_{13}|^2}{\gamma_{d_1}\gamma_{d_3}}. \tag{3.22}
$$

The above equation represents the absorption of the probe laser. The terms denoted as “Three AT peaks” represents the absorption of the probe laser due to the three individual dressed states $|d_1\rangle$, $|d_2\rangle$ and $|d_3\rangle$ giving rise to three AT peaks. The amplitude of the individual AT peaks is proportional to $|\Omega_{p_1}|^2$, $|\Omega_{p_2}|^2$ and $|\Omega_{p_3}|^2$ and is further modified by the “Correction for AT peaks” term as $-\frac{|\kappa_{23}|^2}{\gamma_{d2}\gamma_{d3}}$, $-\frac{|\kappa_{13}|^2}{\gamma_{d1}\gamma_{d3}}$ and $-\frac{|\kappa_{12}|^2}{\gamma_{d1}\gamma_{d2}}$ respectively. The interference between the excitation paths associated with the AT peaks is denoted by the terms “Interference1” and “Interference2”. The magnitude and sign of the interference is proportional to κ_{12}, κ_{23} and κ_{13} respectively. The term “Interference1” denotes pairwise interference of the excitation paths associated with the AT peaks due to coherent decay between the dressed states and is very similar to the three-slit interference. For example, $\kappa_{12}\Omega^*_{p_1}\Omega_{p_2} + c.c$ is the interference between the excitation paths of the dressed states $|d_1\rangle$ and $|d_2\rangle$ due to coherent decay κ_{12}.

We also observe the interference between the excitation paths associated with the AT peaks which are little bit more complicated and denoted as "Interference2". The "Interference2" is the interference between the excitation paths associated with the two AT peaks pair-wise only, but the magnitude and sign are dependent on the coherent decay to the other dressed state. For example, $\kappa_{12}\kappa_{23}\Omega^*_{p_1}\Omega_{p_3} + c.c$ is the interference between the excitation paths of the dressed states $|d_1\rangle$ and $|d_3\rangle$ but the magnitude and sign is dependent on coherent decay to the other dressed state $|d_2\rangle$ through the terms κ_{12} and κ_{23}. So overall, all the interference terms are pair-wise i.e., like $\Omega^*_{p_1}\Omega_{p_2} + c.c$, $\Omega^*_{p_2}\Omega_{p_3} + c.c$ and $\Omega^*_{p_1}\Omega_{p_3} + c.c$ and not like $\Omega^*_{p_1}\Omega_{p_2}\Omega_{p_3}$. This is again similar to the three-slit interference and it indicates the absence of higher order interference between the excitation paths associated with the Autler-Townes peaks. We have also done similar calculation in five-level system (and other higher levels) and we find the interference to be only pair-wise with no higher order interference.

3.3.2.1 Chain configurations with all the control lasers at resonance

The analytical expression for the eigenvalues and eigenvectors of the Hamiltonian in Eq. 3.18, are complicated for general detunings. However, when all control lasers are at resonance the expression is simple and easy to interpret the nature of interference between the excitation paths associated with the AT absorption peaks. In this particular case, the eigenvalues of the dressed states and the associated parameters are listed below:

$$
\begin{aligned}
E_{d_1} =& -\frac{\sqrt{\Omega_{23}^2+\Omega_{34}^2}}{2},\\
|d_1\rangle =& \frac{1}{\sqrt{2}}\left(\frac{\Omega_{23}}{\sqrt{\Omega_{23}^2+\Omega_{34}^2}}|2\rangle - |3\rangle + \frac{\Omega_{34}}{\sqrt{\Omega_{23}^2+\Omega_{34}^2}}|4\rangle\right) = \frac{1}{\sqrt{2}}(\cos\theta\,|2\rangle - |3\rangle + \sin\theta\,|4\rangle),\\
\Gamma_{d_1} =& \frac{1}{4}(\cos^2\theta\Gamma_2 + \Gamma_3 + \sin^2\theta\Gamma_4),\\
E_{d_2} =& 0, \quad |d_2\rangle = -\frac{\Omega_{34}}{\sqrt{\Omega_{23}^2+\Omega_{34}^2}}|2\rangle + \frac{\Omega_{23}}{\sqrt{\Omega_{23}^2+\Omega_{34}^2}}|4\rangle = -\sin\theta\,|2\rangle + \cos\theta\,|4\rangle\,,\\
\Gamma_{d_2} =& \frac{1}{2}(\sin^2\theta\Gamma_2 + \cos^2\theta\Gamma_4),\\
E_{d_3} =& \frac{\sqrt{\Omega_{23}^2+\Omega_{34}^2}}{2},\\
|d_3\rangle =& \frac{1}{\sqrt{2}}\left(\frac{\Omega_{23}}{\sqrt{\Omega_{23}^2+\Omega_{34}^2}}|2\rangle + |3\rangle + \frac{\Omega_{34}}{\sqrt{\Omega_{23}^2+\Omega_{34}^2}}|4\rangle\right) = \frac{1}{\sqrt{2}}(\cos\theta\,|2\rangle + |3\rangle + \sin\theta\,|4\rangle),\\
\Gamma_{d_3} =& \frac{1}{4}(\cos^2\theta\Gamma_2 + \Gamma_3 + \sin^2\theta\Gamma_4), \quad \kappa_{12} = -\frac{(\Gamma_2-\Gamma_4)}{2\sqrt{2}}\cos\theta\sin\theta,\\
\kappa_{13} =& \frac{1}{4}(\Gamma_2\cos^2\theta - \Gamma_3 + \Gamma_4\sin^2\theta), \quad \kappa_{23} = -\frac{(\Gamma_2-\Gamma_4)}{2\sqrt{2}}\cos\theta\sin\theta,\\
\Omega_{p_1} =& \Omega_{p_3} = \frac{1}{\sqrt{2}}\cos\theta\Omega_{12}, \quad \Omega_{p_2} = -\sin\theta\Omega_{12},
\end{aligned}
\tag{3.23}
$$

where,

$$
\tan\theta = \frac{\Omega_{34}}{\Omega_{23}} \quad (\text{i.e.,} \quad \sin\theta = \frac{\Omega_{34}}{\sqrt{\Omega_{23}^2+\Omega_{34}^2}} \quad \text{and} \quad \cos\theta = \frac{\Omega_{23}}{\sqrt{\Omega_{23}^2+\Omega_{34}^2}}),
$$

and the unitary transformation in Eq. 3.2 is similarly expressed as,

$$
\begin{pmatrix} |d_1\rangle \\ |d_2\rangle \\ |d_3\rangle \end{pmatrix} = \frac{1}{\sqrt{2}} \begin{pmatrix} \cos\theta & -1 & \sin\theta \\ -\sqrt{2}\sin\theta & 0 & \sqrt{2}\cos\theta \\ \cos\theta & 1 & \sin\theta \end{pmatrix} \begin{pmatrix} |2\rangle \\ |3\rangle \\ |4\rangle \end{pmatrix}.
$$

The coherent decay κ_{ij} and the incoherent decay $\kappa_{ii} = \Gamma_{d_i}$ are determined using the unitary transformation of the decay matrix, $\hat{\Gamma}$ given in Eq. 3.23 (i.e., $\hat{U}\hat{\Gamma}\hat{U}^{\dagger}$) as follows,

$$\frac{1}{\sqrt{2}}\begin{pmatrix}\cos\theta & -1 & \sin\theta\\ -\sqrt{2}\sin\theta & 0 & \sqrt{2}\cos\theta\\ \cos\theta & 1 & \sin\theta\end{pmatrix}\begin{pmatrix}\Gamma_2 & 0 & 0\\ 0 & \Gamma_3 & 0\\ 0 & 0 & \Gamma_4\end{pmatrix}\frac{1}{\sqrt{2}}\begin{pmatrix}\cos\theta & -\sqrt{2}\sin\theta & \cos\theta\\ -1 & 0 & 1\\ \sin\theta & \sqrt{2}\cos\theta & \sin\theta\end{pmatrix}$$

$$= \begin{pmatrix}\frac{1}{4}(\cos^2\theta\Gamma_2+\Gamma_3+\sin^2\theta\Gamma_4) & -\frac{(\Gamma_2-\Gamma_4)}{2\sqrt{2}}\cos\theta\sin\theta & \frac{1}{4}(\Gamma_2\cos^2\theta-\Gamma_3+\Gamma_4\sin^2\theta)\\ -\frac{(\Gamma_2-\Gamma_4)}{2\sqrt{2}}\cos\theta\sin\theta & \frac{1}{2}(\sin^2\theta\Gamma_2+\cos^2\theta\Gamma_4) & -\frac{(\Gamma_2-\Gamma_4)}{2\sqrt{2}}\cos\theta\sin\theta\\ \frac{1}{4}(\Gamma_2\cos^2\theta-\Gamma_3+\Gamma_4\sin^2\theta) & -\frac{(\Gamma_2-\Gamma_4)}{2\sqrt{2}}\cos\theta\sin\theta & \frac{1}{4}(\cos^2\theta\Gamma_2+\Gamma_3+\sin^2\theta\Gamma_4)\end{pmatrix}.$$

The diagonal elements of this matrix gives $\kappa_{ii}=\Gamma_{d_i}, i=1,2,3$ and the off-diagonal elements gives κ_{12}, κ_{13} and κ_{23}. This calculations are similarly applied to the branching configuration and the four-level loopy system.

For the chain configuration, Eq. 3.21 is also written in terms of θ parameters given in Eq. 3.23 as follows,

$$\begin{aligned}\frac{dC_1}{dt} = -\frac{|\Omega_{12}|^2/8}{N}\Bigg[&\underbrace{\frac{\cos^2\theta}{\gamma_{d_1}}+\frac{\sin^2\theta}{\gamma_{d_2}}+\frac{\cos^2\theta}{\gamma_{d_3}}}_{\text{Three AT peaks}}\\ &\underbrace{-\cos^2\theta\left(\frac{(\Gamma_2-\Gamma_4)\sin^2\theta}{\gamma_{d_1}\gamma_{d_2}}+\frac{(\Gamma_2-\Gamma_4)\sin^2\theta}{\gamma_{d_2}\gamma_{d_3}}+\frac{\Gamma_2\cos^2\theta-\Gamma_3+\Gamma_4\sin^2\theta}{2\gamma_{d_1}\gamma_{d_3}}\right)}_{\text{Interference1}}\\ &\underbrace{+\frac{(\Gamma_2-\Gamma_4)\cos^2\theta\sin^2\theta}{4\gamma_{d_1}\gamma_{d_2}\gamma_{d_3}}\Big(3\Gamma_2\cos^2\theta-2\Gamma_3+\Gamma_4\cos2\theta\Big)}_{\text{Interference2}}\\ &\underbrace{-\frac{\sin^2\theta}{8\gamma_{d_1}\gamma_{d_2}\gamma_{d_3}}\Big((\Gamma_2-\Gamma_4)^2\cos^2\theta+(\Gamma_2\cos^2\theta-\Gamma_3+\Gamma_4\sin^2\theta)^2\Big)}_{\text{Correction for AT peaks}}\Bigg].\end{aligned} \tag{3.24}$$

Various combinations of Γ_2, Γ_3 and Γ_4 are considered to see the nature of interference between the excitation paths associated with the AT peaks. The interference parameters $\kappa_{12}=\kappa_{23}=\kappa_{13}=0$ when $\Gamma_2=\Gamma_3=\Gamma_4$ (see Eq. 3.23) and similarly, the interference terms "Interference1" and "Interference2" and the "Correction for the

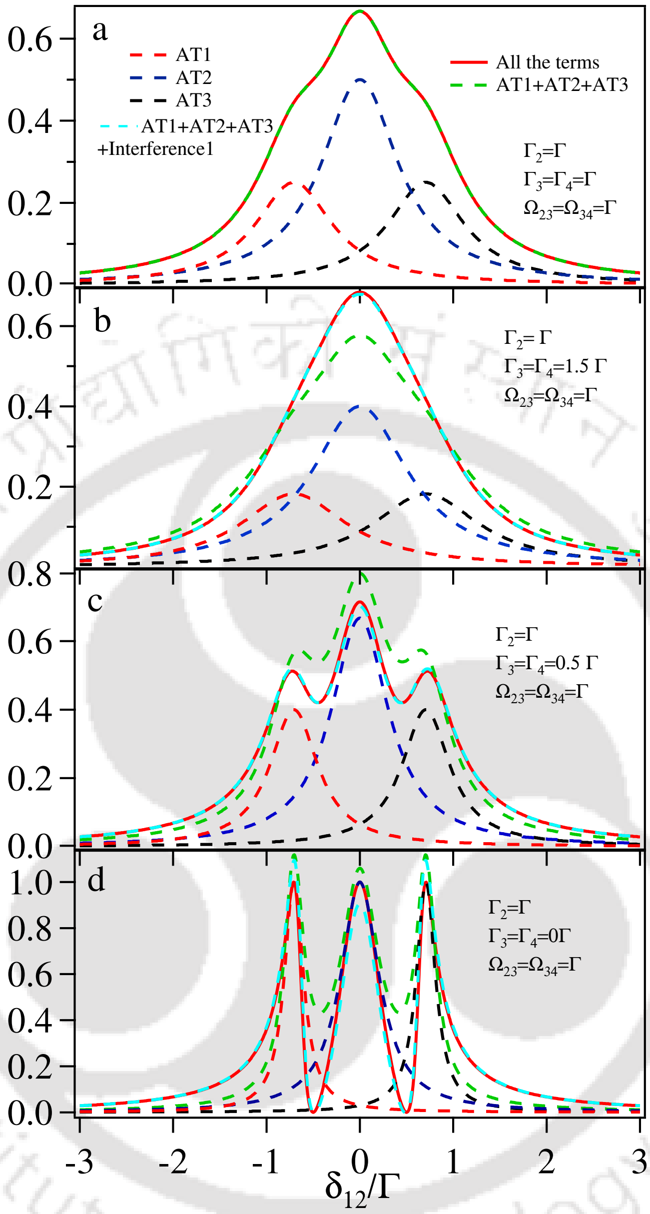

Fig. 3.6: AT peaks and the effect of interference for probe absorption vs its detuning (δ_{12}/Γ) for various four-level systems (chain configurations) with $\delta_{23} = \delta_{34} = 0$ and $\Omega_{23} = \Omega_{34}$ i.e., $\Omega_{p_1} = \Omega_{p_3} = \frac{\Omega_{12}}{2}$, $\Omega_{p_2} = -\frac{\Omega_{12}}{\sqrt{2}}$. a) $\kappa_{12} = \kappa_{23} = \kappa_{13} = 0$, $\Gamma_{d_1} = \Gamma_{d_2} = \Gamma_{d_3} = \frac{\Gamma}{2}$, b) $\kappa_{12} = \kappa_{23} = +\frac{\Gamma_2}{8\sqrt{2}}$, $\kappa_{13} = -\frac{\Gamma_2}{16}$, $\Gamma_{d_1} = \Gamma_{d_3} = \frac{11\Gamma}{16}$, $\Gamma_{d_2} = \frac{5\Gamma}{8}$ c) $\kappa_{12} = \kappa_{23} = -\frac{\Gamma_2}{8\sqrt{2}}$, $\kappa_{13} = +\frac{\Gamma_2}{16}$, $\Gamma_{d_1} = \Gamma_{d_3} = \frac{5\Gamma}{16}$, $\Gamma_{d_2} = \frac{3\Gamma}{8}$, d) $\kappa_{12} = \kappa_{23} = -\frac{\Gamma_2}{4\sqrt{2}}$, $\kappa_{13} = +\frac{\Gamma_2}{8}$, $\Gamma_{d_1} = \Gamma_{d_3} = \frac{\Gamma}{8}$, $\Gamma_{d_2} = \frac{\Gamma}{4}$.

AT peaks" are identically zero (see Eq. 3.24) which is an indication of no interference between any of the excitation paths associated with the AT absorption peaks. The complete overlap of the solid red curve (AT peaks plus interference) and the dashed green curve (AT peaks only) in Fig. 3.6a is an indication of no interference. For $\Gamma_2 < \Gamma_4 = \Gamma_3$, the terms κ_{12} and κ_{23} are positive and κ_{13} is negative for $\Omega_{23} = \Omega_{34}$ in Eq. 3.23. The overall interference terms of "Interference1" and "Interference2" are all positive (see also Eq. 3.24) and the interference between the excitation paths associated with the three AT peaks is constructive. However, the contribution of "Interference2" and "Correction for the AT peaks" are negligibly small as shown Fig. 3.6b.

For $\Gamma_2 > \Gamma_4 = \Gamma_3$, the terms κ_{12} and κ_{23} are negative and κ_{13} is positive for $\Omega_{23} = \Omega_{34}$ in Eq. 3.23. Similarly, all the interference terms in "Interference1" are negative (see Eq. 3.24) and hence the interference between the excitation paths associated with the three AT peaks is destructive. The destructive interference however, partially reduces absorption of the AT peaks at the region of overlap. The interference terms of "Interference2" are positive and the contribution of the constructive interference is very small. The correction to individual AT peaks is equally negligible as shown in Fig. 3.6c. For the decay rate parameters $\Gamma_2 > \Gamma_4 = \Gamma_3 = 0$ in Fig. 3.6d, κ_{12} and κ_{23} are negative and κ_{13} is positive. Hence, all the terms in "Interference1" are negative and in "Interference2" are positive. The destructive interference completely destruct absorption of the three AT peaks at the overlap region giving rise to a double transparency window. The correction to the individual AT peaks from the terms in "Correction for AT peaks" is significant while the interference contribution of "Interference2" is small.

In Fig. 3.7a and 3.7b with the decay rates $\Gamma_2 > \Gamma_4 \neq \Gamma_3$, κ_{12} and κ_{23} are negative and κ_{13} is positive for $\Omega_{23} = \Omega_{34}$. Hence, all the terms in "Interference1" are negative and in "Interference2" are positive. However, the contribution from "Interference2" is very small and the interference between the excitation paths associated with the AT peaks

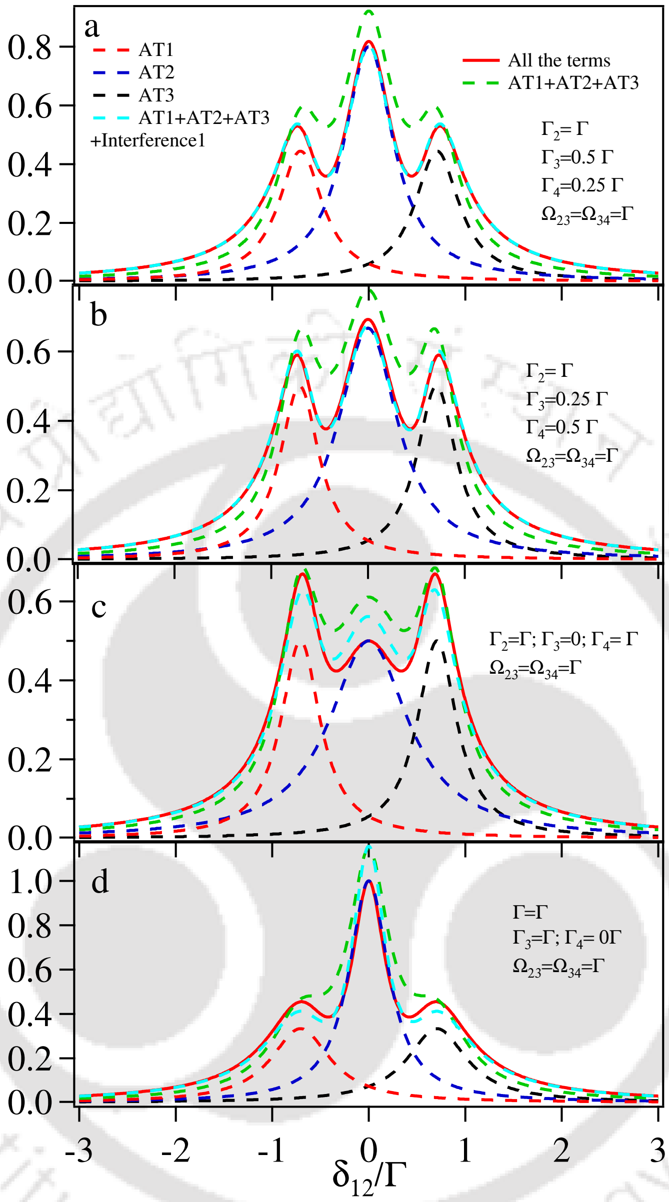

Fig. 3.7: AT peaks and the effect of interference for probe absorption vs its detuning (δ_{12}/Γ) for various four-level systems (chain configurations) with $\delta_{23} = \delta_{34} = 0$ and $\Omega_{23} = \Omega_{34}$ i.e., $\Omega_{p_1} = \Omega_{p_3} = \frac{\Omega_{12}}{2}$, $\Omega_{p_2} = -\frac{\Omega_{12}}{\sqrt{2}}$. a) ladder system: $\kappa_{12} = \kappa_{23} = -\frac{3\Gamma_2}{16\sqrt{2}}$, $\kappa_{13} = +\frac{\Gamma_2}{32}$, $\Gamma_{d_1} = \Gamma_{d_3} = \frac{9\Gamma}{32}$, $\Gamma_{d_2} = \frac{5\Gamma}{16}$ b) ladder system: $\kappa_{12} = \kappa_{23} = -\frac{\Gamma_2}{8\sqrt{2}}$, $\kappa_{13} = +\frac{\Gamma_2}{8}$, $\Gamma_{d_1} = \Gamma_{d_3} = \frac{\Gamma}{4}$, $\Gamma_{d_2} = \frac{3\Gamma}{8}$ c) N-system: $\kappa_{12} = \kappa_{23} = 0$, $\kappa_{13} = +\frac{\Gamma_2}{4}$, $\Gamma_{d_1} = \Gamma_{d_3} = \frac{\Gamma}{4}$, $\Gamma_{d_2} = \frac{\Gamma}{2}$ d) ladder-lambda system: $\kappa_{12} = \kappa_{23} = -\frac{\Gamma_2}{4\sqrt{2}}$, $\kappa_{13} = -\frac{\Gamma_2}{8}$, $\Gamma_{d_1} = \Gamma_{d_3} = \frac{3\Gamma}{8}$, $\Gamma_{d_2} = \frac{\Gamma}{2}$.

is essentially destructive. The modification of the individual AT peaks by "Correction for AT peaks" terms is also negligible. For parameters relevant to N-system in Fig. 3.7c i.e., $\Gamma_3 = 0, \Gamma_4 = \Gamma_2$, both κ_{12} and κ_{23} are zero but κ_{13} is positive. This implies, the first two terms in "Interference1" are zero and the third term is negative. All the terms in "Interference2" are zero and therefore the overall interference between the excitation paths of the dressed states $|d_1\rangle$ and $|d_3\rangle$ is destructive which partially reduce the absorption of the AT peaks. The contribution of "Correction for AT peaks" is significant as seen by the deviation of the dashed cyan curve from the solid red curve. For the parameters relevant to the ladder-lambda system i.e., $\Gamma_3 = \Gamma_2, \Gamma_4 = 0$ in Fig. 3.7d, the terms κ_{12}, κ_{23} and κ_{13} are all negative. Hence, the first two terms in "Interference1" are negative and the third term is positive. Similarly, the first two terms in "Interference2" are negative and the third term is positive. In the said figure, destructive interference between the excitation paths associated with the three AT peaks dominates and both "Interference2" and "Correction for AT peaks" have a significant contribution.

The possibility of tuning the interference from constructive to destructive by tuning the control laser parameter such as the Rabi frequencies is illustrated in Fig. 3.8. In the three-level system we noted that the nature of interference can not be tuned from negative to positive or zero by changing the laser parameters. However, if we consider a simple case in four-level-system where $\Gamma_3 < \Gamma_2$ and $\Gamma_4 = 0$ it is possible to tune the interference from negative to positive between the excitation paths of the dressed states $|d_1\rangle$ and $|d_3\rangle$. The interference between the excitation paths of the dressed states $|d_1\rangle$ and $|d_3\rangle$ is given by the third term in "Interference1" given in Eq. 3.24. In Fig. 3.8, we plot the interference parameter κ_{13} vs Ω_{34} for a system with $\Gamma_3 = 0.75\Gamma_2$ and $\Gamma_4 = 0$ and from Eq. 3.24 the interference between the excitation paths of the dressed states $|d_1\rangle$ and $|d_3\rangle$ is expressed as $(\Gamma_2 \cos^2\theta(0.75 - \cos^2\theta))/(2\gamma_{d_1}\gamma_{d_3})$. The minimum value of $\cos^2\theta$ is 0 and the maximum value is 1 as Ω_{34} changes. There is no interference between the excitation paths of the dressed states $|d_1\rangle$ and $|d_3\rangle$ when $\cos^2\theta = 0$, the interference is negative when $\cos^2\theta = 1$ and it is positive when

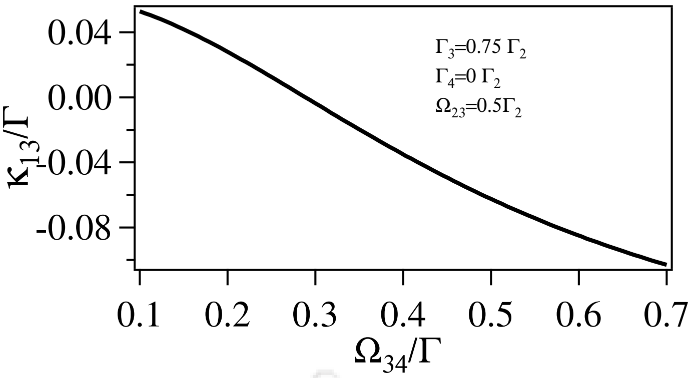

Fig. 3.8: Variation of coherent decay between dressed state $|d_1\rangle$ and $|d_3\rangle$, i.e., κ_{13} as a function of the coupling strength Ω_{34} of the control laser.

$\cos^2\theta < 0.75$. Therefore, it is possible to tune the interference between the excitation paths of the dressed states $|d_1\rangle$ and $|d_3\rangle$ from constructive, to zero and to destructive.

3.3.2.2 Branching configurations with all control lasers at resonance

We similarly consider the case when all the control lasers are at resonance for the Hamiltonian given in Eq. 3.19. In this particular case the energy of the dressed states and the related parameters are listed below:

$$
\begin{aligned}
E_{d_1} =& -\frac{\sqrt{\Omega_{23}^2+\Omega_{24}^2}}{2},\\
|d_1\rangle =& \frac{1}{\sqrt{2}}(-|2\rangle + \frac{\Omega_{23}}{\sqrt{\Omega_{23}^2+\Omega_{24}^2}}|3\rangle + \frac{\Omega_{24}}{\sqrt{\Omega_{23}^2+\Omega_{24}^2}}|4\rangle) = \frac{1}{\sqrt{2}}(-|2\rangle + \cos\theta\,|3\rangle + \sin\theta\,|4\rangle),\\
\Gamma_{d1} =& \frac{1}{4}(\Gamma_2 + \cos^2\theta\Gamma_3 + \sin^2\theta\Gamma_4,\\
E_{d_2} =& 0, \quad |d_2\rangle = -\frac{\Omega_{24}}{\sqrt{\Omega_{23}^2+\Omega_{24}^2}}|3\rangle + \frac{\Omega_{23}}{\sqrt{\Omega_{23}^2+\Omega_{24}^2}}|4\rangle = -\sin\theta\,|3\rangle + \cos\theta\,|4\rangle\,,\\
\Gamma_{d_2} =& \frac{1}{2}(\sin^2\theta\Gamma_3 + \cos^2\theta\Gamma_4),\\
E_{d_3} =& \frac{\sqrt{\Omega_{23}^2+\Omega_{24}^2}}{2},\\
|d_3\rangle =& \frac{1}{\sqrt{2}}(|2\rangle + \frac{\Omega_{23}}{\sqrt{\Omega_{23}^2+\Omega_{24}^2}}|3\rangle + \frac{\Omega_{24}}{\sqrt{\Omega_{23}^2+\Omega_{24}^2}}|4\rangle) = \frac{1}{\sqrt{2}}(|2\rangle + \cos\theta\,|3\rangle + \sin\theta\,|4\rangle),\\
\Gamma_{d_3} =& \frac{1}{4}(\Gamma_2 + \cos^2\theta\Gamma_3 + \sin^2\theta\Gamma_4), \quad \kappa_{12} = -\frac{(\Gamma_3-\Gamma_4)}{2\sqrt{2}}\cos\theta\sin\theta,\\
\kappa_{13} =& \frac{1}{4}(-\Gamma_2 + \cos^2\theta\Gamma_3 + \sin^2\theta\Gamma_4), \quad \kappa_{23} = -\frac{(\Gamma_3-\Gamma_4)}{2\sqrt{2}}\cos\theta\sin\theta,\\
\Omega_{p_1} =& -\Omega_{p_3} = \frac{\Omega_{12}}{\sqrt{2}}, \quad \Omega_{p_2} = 0,
\end{aligned}
\tag{3.25}
$$

where,

$$
\tan\theta = \frac{\Omega_{24}}{\Omega_{23}} \quad (\text{i.e.,} \quad \sin\theta = \frac{\Omega_{24}}{\sqrt{\Omega_{23}^2+\Omega_{24}^2}} \quad \text{and} \quad \cos\theta = \frac{\Omega_{23}}{\sqrt{\Omega_{23}^2+\Omega_{24}^2}}),
$$

and the unitary transformation in Eq. 3.2 is similarly expressed as,

$$
\begin{pmatrix} |d_1\rangle \\ |d_2\rangle \\ |d_3\rangle \end{pmatrix} = \frac{1}{\sqrt{2}} \begin{pmatrix} -1 & \cos\theta & \sin\theta \\ 0 & -\sqrt{2}\sin\theta & \sqrt{2}\cos\theta \\ 1 & \cos\theta & \sin\theta \end{pmatrix} \begin{pmatrix} |2\rangle \\ |3\rangle \\ |4\rangle \end{pmatrix}.
$$

For the chain configuration, Eq. 3.21 is also written in terms of θ parameters given in Eq. 3.25 as follows,

$$\frac{dC_1}{dt} = -\frac{|\Omega_{12}|^2/8}{N}\left[\underbrace{\frac{1}{\gamma_{d_1}} + \frac{1}{\gamma_{d_3}}}_{\text{Two AT peaks}} + \underbrace{\frac{\Gamma_3\cos^2\theta - \Gamma_2 + \Gamma_4\sin^2\theta}{2\gamma_{d_1}\gamma_{d_3}}}_{\text{Interference1}}\right.$$
$$\left. - \underbrace{\frac{(\Gamma_3-\Gamma_4)^2\cos^2\theta\sin^2\theta}{4\gamma_{d_1}\gamma_{d_2}\gamma_{d_3}}}_{\text{Interference2}} - \underbrace{\frac{(\Gamma_3-\Gamma_4)^2\cos^2\theta\sin^2\theta}{4\gamma_{d_1}\gamma_{d_2}\gamma_{d_3}}}_{\text{Correction for AT peaks}}\right]. \tag{3.26}$$

The central AT peak shown by the dashed blue curve (corresponding to eigenvalue 0) in Fig. 3.9 has zero amplitude as $\Omega_{p_2} = 0$. Therefore, only two dressed states $|d_1\rangle$ and $|d_3\rangle$ can be excited by the probe laser and the branching system behaves like the three-level system. For the Tripod system [92] where $\Gamma_3 = \Gamma_4 = 0$, both the terms "Interference2" and "Correction for AT peaks" vanishes. The interference between the excitation paths of the dressed states $|d_1\rangle$ and $|d_3\rangle$ is destructive (see also Eq. 3.26) and completely destructs absorption of the two AT peaks at resonance (see also Fig. 3.9a).

For the decay rate parameters $\Gamma_2 = 0$, $\Gamma_1 = \Gamma_3 = \Gamma_4 = \Gamma$ in Fig. 3.9b (valid for the inverted tripod system [94]), the terms "Interference2" and "Correction for AT peaks" vanishes and the interference between the excitation paths of the dressed states $|d_1\rangle$ and $|d_3\rangle$ is constructive which enhances absorption. For the Ladder-lambda system with $\Gamma_1 = \Gamma_3 = 0$, $\Gamma_2 = \Gamma$ and $\Gamma_4 = 0.5\Gamma$ the interference term κ_{13} is negative and the interference between the excitation paths of the dressed states $|d_1\rangle$ and $|d_3\rangle$ is destructive interference (see also Eq. 3.26). The non-zero term of "Interference2" is also negative and contribute to destructive interference. The "Correction for the AT peaks " is non-zero for the two AT peaks leading to further reduction in the absorption as shown in Fig. 3.9c. For the decay rate parameters $\Gamma_2 = \Gamma_3 = \Gamma_4 = \Gamma$ (valid for Y-system), the terms "Interference1", "Interference2" and "Correction for AT peaks" are zero as $\kappa_{12} = \kappa_{13} = \kappa_{23} = 0$. There is no interference between any of the excitation paths associated with the AT peaks as evidenced by the complete overlap between the solid red curve and the green dash curve in Fig. 3.9d.

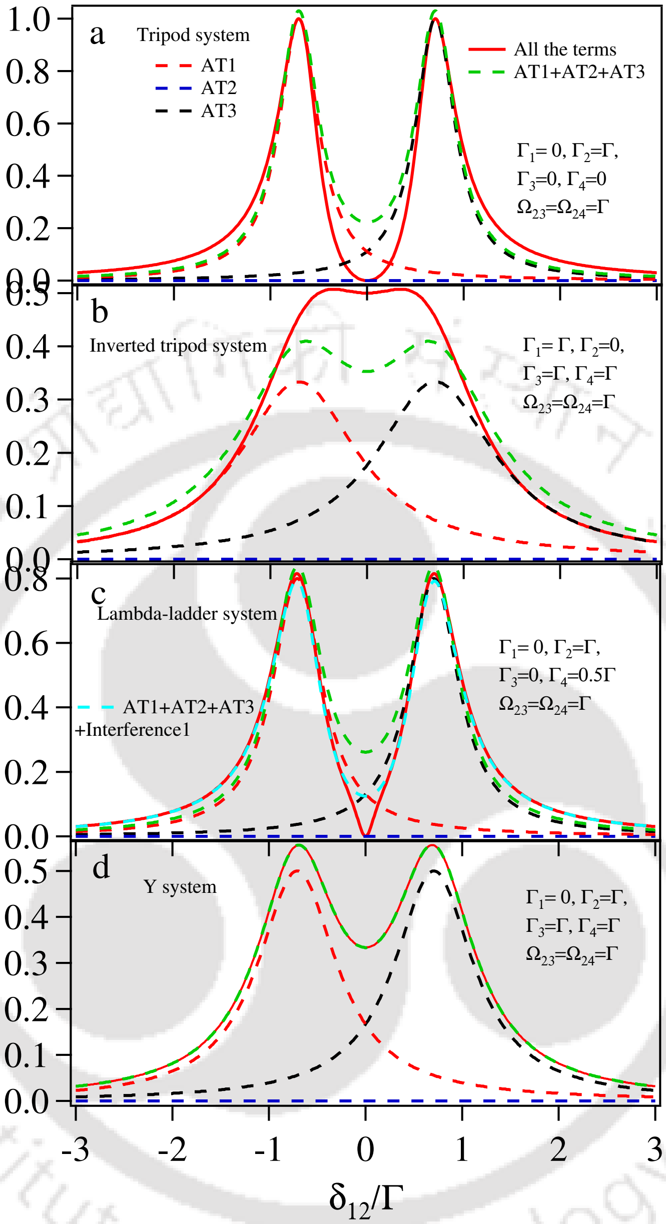

Fig. 3.9: AT peaks and the effect of interference for probe absorption vs its detuning (δ_{12}/Γ) for various four-level systems (branching configurations) with $\delta_{23} = \delta_{24} = 0$ and $\Omega_{23} = \Omega_{24}$ i.e., $\Omega_{p_1} = -\Omega_{p_3} = \frac{\Omega_{12}}{\sqrt{2}}$, $\Omega_{p_2} = 0$ a) Tripod-system: $\kappa_{12} = \kappa_{23} = 0$, $\kappa_{13} = -\frac{\Gamma}{4}$, $\Gamma_{d_1} = \Gamma_{d_3} = \frac{\Gamma}{4}$, $\Gamma_{d_2} = 0$ b) Inverted tripod system: $\kappa_{12} = \kappa_{23} = 0$, $\kappa_{13} = +\frac{\Gamma}{4}$, $\Gamma_{d_1} = \Gamma_{d_3} = \frac{\Gamma}{4}$, $\Gamma_{d_2} = \frac{\Gamma}{2}$ c) Lambda-ladder-system: $\kappa_{12} = \kappa_{23} = +\frac{\Gamma}{8\sqrt{2}}$, $\kappa_{13} = \frac{3\Gamma}{16}$, $\Gamma_{d_1} = \Gamma_{d_3} = \frac{5\Gamma}{16}$, $\Gamma_{d_2} = \frac{\Gamma}{8}$ d) Y-system: $\kappa_{12} = \kappa_{23} = \kappa_{13} = 0$, $\Gamma_{d_1} = \Gamma_{d_2} = \Gamma_{d_3} = \frac{\Gamma}{2}$.

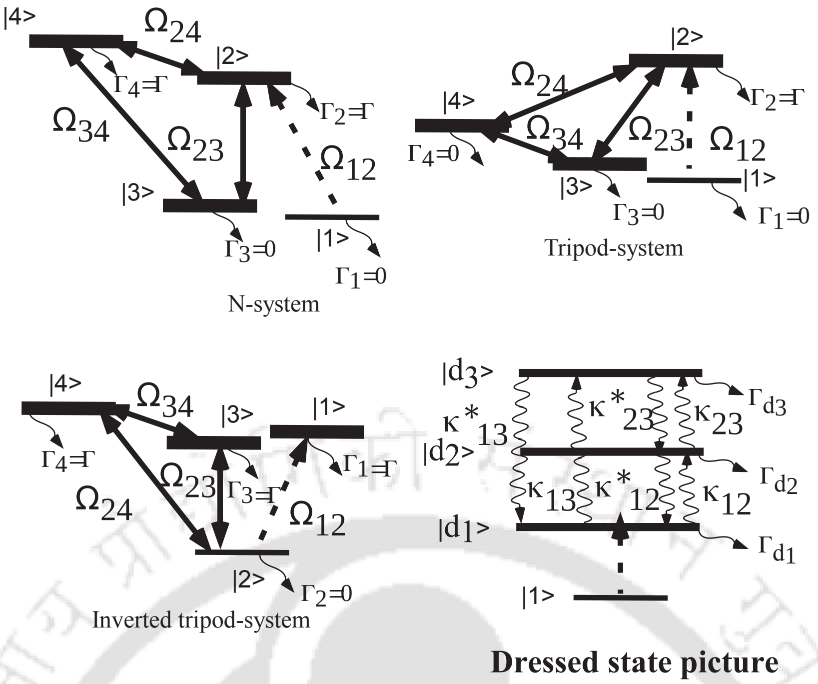

Fig. 3.10: Four-level loopy system in bare and dressed state picture.

3.3.3 Four-level loopy system

The four-level loopy system is as shown in Fig. 3.10. It can be of various types depending upon the energy level of the states $|1\rangle$, $|2\rangle$, $|3\rangle$, $|4\rangle$ as we discussed in the previous section. The study of the loopy system is very important as it further authenticates our approach for the dressed states as in this case the interference terms, $\kappa's$ and $\Omega_p's$ can be complex. The various loopy system has been discussed previously [95, 96, 97, 98]. The density matrix element for the probe absorption in the four-level loopy system shown in Fig. 3.10 is given by the following equation,

$$\rho_{12} = \frac{\frac{i}{2}\frac{\Omega_{12}}{\gamma_{12}}}{1+\frac{\frac{1}{4}\frac{|\Omega_{23}|^2}{\gamma_{12}\gamma_{13}}+\frac{1}{4}\frac{|\Omega_{24}|^2}{\gamma_{12}\gamma_{14}}+\frac{i}{8}\frac{\Omega_{23}^*\Omega_{34}^*\Omega_{24}+c.c.}{\gamma_{12}\gamma_{13}\gamma_{14}}}{1+\frac{1}{4}\frac{|\Omega_{34}|^2}{\gamma_{13}\gamma_{14}}}} . \tag{3.27}$$

The Hamiltonian associated with the control lasers for this system is given below:

$$H_c = \hbar \begin{bmatrix} 0 & \frac{\Omega_{23}}{2} & \frac{\Omega_{24}}{2} \\ \frac{\Omega_{23}^*}{2} & -\delta_{23} & \frac{\Omega_{34}}{2} \\ \frac{\Omega_{24}^*}{2} & \frac{\Omega_{34}^*}{2} & -\delta_{24} \end{bmatrix}. \tag{3.28}$$

The general control laser Rabi frequencies will be $\Omega_{23} = |\Omega_{23}|e^{i\phi_{23}}$, $\Omega_{34} = |\Omega_{34}|e^{i\phi_{34}}$ and $\Omega_{24} = |\Omega_{24}|e^{i\phi}$ which can be considered (without loss of generality) as $\Omega_{23} = |\Omega_{23}|$ and $\Omega_{34} = |\Omega_{34}|$ and $\Omega_{24} = |\Omega_{24}|e^{i\phi}$ i.e., considering Ω_{23} and Ω_{34} as real and $\Omega_{24} = |\Omega_{24}|e^{i\phi}$ as complex where $\phi = \phi_{24} - \phi_{23} - \phi_{34}$. The eigenvalue and eigenvector corresponding to general parameters in the above Hamiltonian given in Eq. 3.28 is complicated. However, it is relatively simpler for the case where all the control lasers are at resonance and $\Omega_{23} = \Omega_{34} = \Omega$ and $\Omega_{24} = \Omega_1 e^{i\phi}$ where Ω and Ω_1 are real quantities.

The eigenvalues, eigenvectors and the various other parameters for $\phi = 0$ are listed

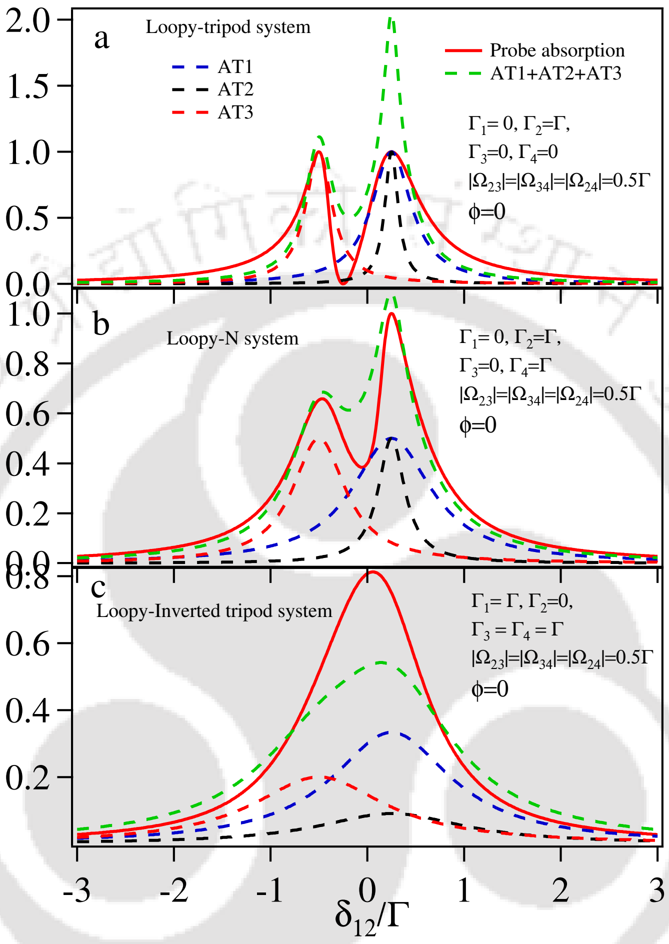

Fig. 3.11: AT peaks and the effect of interference for probe absorption vs its detuning (δ_{12}/Γ) for various four-level loopy systems with $\delta_{23} = \delta_{34} = \delta_{24} = 0$, $\Omega_{23} = \Omega_{34} = \Omega_{24}$ i.e., $\Omega_{p_1} = -\frac{\Omega_{12}}{\sqrt{2}}$, $\Omega_{p_2} = \frac{\Omega_{12}}{\sqrt{6}}$, $\Omega_{p_3} = \frac{\Omega_{12}}{\sqrt{3}}$ and $\phi = 0$. a) $\kappa_{12} = -\frac{\Gamma}{4\sqrt{3}}$, $\kappa_{23} = +\frac{\Gamma}{6\sqrt{2}}$, $\kappa_{13} = -\frac{\Gamma}{2\sqrt{6}}$, $\Gamma_{d_1} = \frac{\Gamma}{4}$, $\Gamma_{d_2} = \frac{\Gamma}{12}$ and $\Gamma_{d_3} = \frac{\Gamma}{6}$ b) $\kappa_{12} = \kappa_{13} = 0$, $\kappa_{23} = +\frac{\Gamma}{3\sqrt{2}}$, $\Gamma_{d_1} = \frac{\Gamma}{2}$, $\Gamma_{d_2} = \frac{\Gamma}{6}$ and $\Gamma_{d_3} = \frac{\Gamma}{3}$ c) $\kappa_{12} = +\frac{\Gamma}{4\sqrt{3}}$, $\kappa_{23} = -\frac{\Gamma}{6\sqrt{2}}$, $\kappa_{13} = +\frac{\Gamma}{2\sqrt{6}}$, $\Gamma_{d_1} = \frac{\Gamma}{4}$, $\Gamma_{d_2} = \frac{5\Gamma}{12}$ and $\Gamma_{d_3} = \frac{\Gamma}{3}$.

below:

$$
\begin{aligned}
E_{d_1} &= -\frac{\Omega_1}{2},\ |d_1\rangle = -\sqrt{\frac{1}{2}}\,|2\rangle + \sqrt{\frac{1}{2}}\,|4\rangle\,,\ \Gamma_{d_1} = \frac{\Gamma_2}{2} + \frac{\Gamma_4}{2},\\
E_{d_2} &= \frac{\Omega_1 - \Omega''}{4},\ |d_2\rangle = \frac{\sqrt{2}\Omega\Big[\,|2\rangle - \Big(\frac{\Omega_1+\Omega''}{2\Omega}\Big)\,|3\rangle + |4\rangle\,\Big]}{\sqrt{\Omega''(\Omega''+\Omega_1)}},\\
\Gamma_{d_2} &= \frac{2\Omega^2\Big[\Gamma_2 + \Big(\frac{\Omega_1+\Omega''}{2\Omega}\Big)^2\Gamma_3 + \Gamma_4\Big]}{\Omega''(\Omega''+\Omega_1)},\\
E_{d_3} &= \frac{\Omega_1 + \Omega''}{4},\ |d_3\rangle = \frac{\sqrt{2}\Omega\Big[\,|2\rangle + \Big(\frac{\Omega''-\Omega_1}{2\Omega}\Big)\,|3\rangle + |4\rangle\,\Big]}{\sqrt{\Omega''(\Omega''-\Omega_1)}},\\
\Gamma_{d_3} &= \frac{2\Omega^2\Big[\Gamma_2 + \Big(\frac{\Omega''-\Omega_1}{2\Omega}\Big)^2\Gamma_3 + \Gamma_4\Big]}{\Omega''(\Omega''-\Omega_1)},\\
\kappa_{12} &= -\frac{(\Gamma_2-\Gamma_4)\Omega}{2\sqrt{\Omega''(\Omega''+\Omega_1)}},\ \kappa_{23} = \frac{(+\Gamma_2 - 2\Gamma_3 + \Gamma_4)\Omega}{2\sqrt{2}\Omega''},\\
\kappa_{13} &= -\frac{(\Gamma_2-\Gamma_4)\Omega}{2\sqrt{\Omega''(\Omega''-\Omega_1)}},\ \Omega_{p_1} = -\frac{\Omega_{12}}{\sqrt{2}},\ \Omega_{p_2} = \frac{\sqrt{2}\Omega}{\sqrt{\Omega''(\Omega''+\Omega_1)}}\Omega_{12},\\
\Omega_{p_3} &= \frac{\sqrt{2}\Omega}{\sqrt{\Omega''(\Omega''-\Omega_1)}}\Omega_{12},\quad \text{where,}\ \ \Omega'' = \sqrt{8\Omega^2+\Omega_1^2}.
\end{aligned}
\tag{3.29}
$$

We consider the decay rate parameters $\Gamma_1 = \Gamma_3 = \Gamma_4 = 0$, $\Gamma_2 = \Gamma$ (valid for loopy-tripod-system) and also take $\Omega_{23} = \Omega_{34} = \Omega_{24} = 0.5\Gamma$ for the various loopy systems. For this system, all the individual terms of "Interference1" are negative and that of "Interference2" are positive but negligibly small. The destructive interference completely destructs probe absorption at the crossing regions of the AT peaks as shown in Fig. 3.11a. For the decay rate parameters $\Gamma_2 = \Gamma_4 = \Gamma$, $\Gamma_1 = \Gamma_3 = 0$ (valid for the loopy N-system), the interference terms $\kappa_{12} = \kappa_{13} = 0$ and κ_{23} is negative. Hence, corresponding to "Interference1" there is no interference between the excitation paths of the dressed states $|d_1\rangle$ and $|d_2\rangle$ and $|d_1\rangle$ and $|d_3\rangle$ while there is destructive interference between the excitation paths of the dressed states $|d_2\rangle$ and $|d_3\rangle$. For this system, all the terms corresponding to "Interference2" are zero. The probe absorption and the AT peaks of the system are shown in Fig. 3.11b. For the decay rate parameters $\Gamma_1 = \Gamma_3 = \Gamma_4 = \Gamma$, $\Gamma_2 = 0$ which is valid for loopy inverted-tripod system (see Fig. 3.11c), all the individual terms of the “Interference1” and “Interference2” are positive and hence there is constructive interference between the excitation paths associated with the AT peaks.

For $\phi = \pi/2$ the different parameters for the dressed states are given below:

$$
\begin{aligned}
E_{d_1} &= -\frac{\Omega'}{2},\ |d_1\rangle = \frac{\sqrt{\Omega_1^2+\Omega^2}}{\sqrt{2}\Omega'}\left[\frac{\Omega'-i\Omega_1}{\Omega'+i\Omega_1}|2\rangle - \frac{2\Omega}{\Omega'+i\Omega_1}|3\rangle + |4\rangle\right],\\
\Gamma_{d_1} &= \frac{\Omega_1^2+\Omega^2}{2\Omega'^2}\left[\Gamma_2 + \frac{4\Omega^2}{\Omega'^2+\Omega^2}\Gamma_3 + \Gamma_4\right],\\
E_{d_2} &= 0,\ |d_2\rangle = -\frac{\Omega}{\Omega'}|2\rangle - \frac{i\Omega_1}{\Omega'}|3\rangle + \frac{\Omega}{\Omega'}|4\rangle,\\
\Gamma_{d_2} &= \frac{\Omega^2}{\Omega'^2}\Gamma_2 + \frac{\Omega_1^2}{\Omega'^2}\Gamma_3 + \frac{\Omega^2}{\Omega'^2}\Gamma_4,\\
E_{d_3} &= \frac{\Omega'}{2},\ |d_3\rangle = \frac{\sqrt{\Omega_1^2+\Omega^2}}{\sqrt{2}\Omega'}\left[\frac{\Omega'+i\Omega_1}{\Omega'-i\Omega_1}|2\rangle + \frac{2\Omega}{\Omega'-i\Omega_1}|3\rangle + |4\rangle\right],\\
\Gamma_{d_3} &= \frac{\Omega_1^2+\Omega^2}{2\Omega'^2}\left[\Gamma_2 + \frac{4\Omega^2}{\Omega'^2+\Omega^2}\Gamma_3 + \Gamma_4\right],\\
\kappa_{12} &= -\frac{\Omega\sqrt{\Omega^2+\Omega_1^2}}{2\sqrt{2}\Omega'^2}\left[\frac{\Omega'+i\Omega_1}{\Omega'-i\Omega_1}\Gamma_2 - \frac{i2\Omega_1}{\Omega'-i\Omega_1}\Gamma_3 - \Gamma_4\right],\\
\kappa_{13} &= -\frac{\Omega^2+\Omega_1^2}{4\Omega'^2}\Big[-\left(\frac{\Omega'+i\Omega_1}{\Omega'-i\Omega_1}\right)^2\Gamma_2 + \frac{4\Omega^2}{(\Omega'-i\Omega_1)^2}\Gamma_3 - \Gamma_4\Big],\\
\kappa_{23} &= -\frac{\Omega\sqrt{\Omega^2+\Omega_1^2}}{2\sqrt{2}\Omega'^2}\left[\frac{\Omega'+i\Omega_1}{\Omega'-i\Omega_1}\Gamma_2 - \frac{i2\Omega_1}{\Omega'-i\Omega_1}\Gamma_3 - \Gamma_4\right],\\
\Omega_{p_1} &= \frac{\sqrt{\Omega_1^2+\Omega^2}}{\sqrt{2}\Omega'}\frac{\Omega'-i\Omega_1}{\Omega'+i\Omega_1}\Omega_{12},\ \Omega_{p_2} = -\frac{\Omega}{\Omega'}\Omega_{12},\\
\Omega_{p_3} &= \frac{\sqrt{\Omega_1^2+\Omega^2}}{\sqrt{2}\Omega'}\frac{\Omega'+i\Omega_1}{\Omega'-i\Omega_1}\Omega_{12},\ \text{where,}\ \ \Omega' = \sqrt{2\Omega^2+\Omega_1^2}.
\end{aligned}
\tag{3.30}
$$

Similarly we consider the case for $\Gamma_1 = \Gamma_3 = \Gamma_4 = 0$, $\Gamma_2 = \Gamma$ which is valid for the Loopy-tripod system and also take $\Omega_{23} = \Omega_{34} = \Omega_{24} = 0.5\Gamma$ for the various loopy type systems. For this case, all the individual terms of “Interference1” and “Interference2” are negative and hence there is prominent destructive interference between the excitation paths associated with the AT peaks (see Fig. 3.12a), since

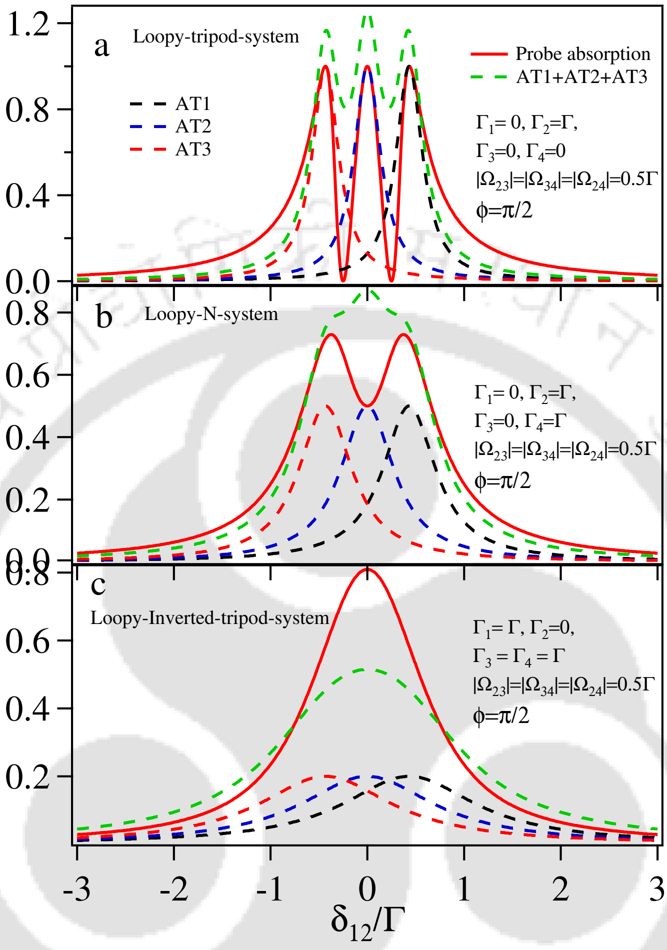

Fig. 3.12: AT peaks and the effect of interference for probe absorption vs its detuning (δ_{12}/Γ) for various four-level loopy systems with $\delta_{23} = \delta_{34} = \delta_{24} = 0$, $\Omega_{23} = \Omega_{34} = \Omega_{24}$ i.e., $\Omega_{p_1} = \frac{1}{\sqrt{3}}\frac{\sqrt{3}-i}{\sqrt{3}+i}\Omega_{12}$, $\Omega_{p_2} = -\frac{\Omega_{12}}{\sqrt{3}}$, $\Omega_{p_3} = \frac{1}{\sqrt{3}}\frac{\sqrt{3}+i}{\sqrt{3}-i}\Omega_{12}$ and $\phi = \pi/2$. a) $\kappa_{12} = \kappa_{23} = -\frac{\sqrt{3}+i}{\sqrt{3}-i}\frac{\Gamma}{6}$, $\kappa_{13} = +\left(\frac{\sqrt{3}+i}{\sqrt{3}-i}\right)^2\frac{\Gamma}{6}$, $\Gamma_{d_1} = \Gamma_{d_2} = \Gamma_{d_3} = \frac{\Gamma}{6}$ b) $\kappa_{12} = \kappa_{23} = -\frac{i}{\sqrt{3}-i}\frac{\Gamma}{3}$, $\kappa_{23} = +\left[\left(\frac{\sqrt{3}+i}{\sqrt{3}-i}\right)^2 + 1\right]\frac{\Gamma}{6}$, $\Gamma_{d_1} = \Gamma_{d_2} = \Gamma_{d_3} = \frac{\Gamma}{3}$ c) $\kappa_{12} = \kappa_{23} = +\frac{\sqrt{3}+i}{\sqrt{3}-i}\frac{\Gamma}{6}$, $\kappa_{13} = -\left[\left(\frac{2}{\sqrt{3}-i}\right)^2 - 1\right]\frac{\Gamma}{6}$, $\Gamma_{d_1} = \Gamma_{d_2} = \Gamma_{d_3} = \frac{\Gamma}{3}$.

the probe absorption goes to zero at the overlapping region of the AT peaks. This case is also similar for $\Gamma_2 = \Gamma_4 = \Gamma$, $\Gamma_1 = \Gamma_3 = 0$ which is valid for loopy N-system (see Fig. 3.12b). However, the magnitude of the interference terms are less compared to the loopy-tripod system. For $\Gamma_1 = \Gamma_3 = \Gamma_4 = \Gamma$, $\Gamma_2 = 0$ which is valid for loopy inverted-tripod system (see Fig. 3.12c), all the individual terms of the "Interference1" and "Interference2" are positive and hence there is constructive interference between the excitation paths associated with the AT peaks.

The result of this chapter appear in the following publication: The European Physical Journal D (Eur. Phys. J. D (2020) 74: 187; https://doi.org/10.1140/epjd/e2020-10187-3).

4

Hyperfine measurement of $6P_{1/2}$ state in ^{87}Rb using double resonance on blue and IR transition

4.1 Introduction

This chapter describes the spectroscopy of $6P_{1/2}$ state in ^{87}Rb using double resonance technique at 780 nm and 421 nm. The double resonance technique is implemented using electromagnetically induced transparency (EIT) and optical pumping methods. Using these spectroscopy methods, the hyperfine splitting of $6P_{1/2}$ state is measured with precision of < 400 kHz and the magnetic dipole hyperfine constant is also calculated.

The chapter begins with a detailed theoretical description of the double resonance technique using the EIT effect in a V-type system (or coherent control scheme) and the optical pumping scheme. The experimental set-up and the results are also discussed in the subsequent sections.

4.2 Measurement Schemes

4.2.1 Coherent Control Scheme

The relevant energy level diagram for coherent control scheme is given in Fig. 4.1a. The 780 nm probe laser is locked to resonance on $5S_{1/2}(F = 2) \rightarrow 5P_{3/2}(F = 3)$ cycling transition with oscillator strength, $f = 0.668$ and a lifetime, $\tau_1 = 26.23$ ns [99]. The absorption of the probe is monitored as the co-propagating 421 nm control laser beam scans $5S_{1/2}(F = 2) \rightarrow 6P_{1/2}$ weak transition with oscillator strength, $f = 0.004$ [100, 101] and a lifetime, $\tau_2 = 125.32$ ns [102]. As soon as the 421 nm scanning control laser comes to resonance (i.e., when both laser beams are addressing the zero velocity group atoms), absorption of the 780 nm probe laser is reduced giving rise to a Doppler-free dip. However, the linewidth of the transition is finite and therefore kinetic theory gives a finite range of velocities (i.e., near zero velocity groups atoms) which also contribute to the peak lineshape. There are two factor contributing to the reduction of probe absorption at the line center. One is due to coherent effect which cause EIT in a V-type system [23, 103] and the other is optical pumping to other ground hyperfine level, $5S_{1/2}(F = 1)$ [104, 105, 106] via $5S_{1/2}(F = 2) \rightarrow 6P_{1/2}$ excitation and $6P_{1/2} \rightarrow 5S_{1/2}(F = 1)$ decay channels.

We consider the effect of optical pumping on the EIT spectrum of a V-type system shown in Fig. 4.1a. This V-type of system is open as the population from the $6P_{1/2}$ state decays to the other ground state hyperfine level, $5S_{1/2}(F = 1)$ and can not be recycled. The mixing rate, $\Pi_g \approx 2\pi \times 40$ kHz, for the hyperfine ground states is due to thermal collisions and the time of fight of atoms across the laser beam [11, 107]. The contribution due to time of flight is defined as $d/\tilde{v}$ where, $\tilde{v}$ is the thermal velocity of the atoms in the atomic medium and d is the diameter of the laser beam. The Hamiltonian H of a closed V-type system under electric-dipole and rotating-wave

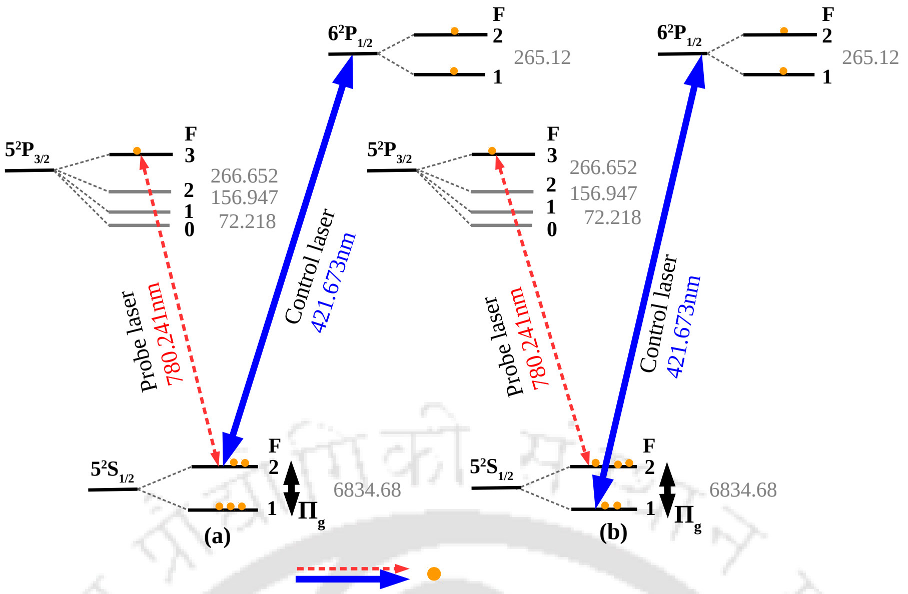

Fig. 4.1: A diagrammatic energy scheme (and hyperfine splitting in MHz) of measuring the hyperfine splitting interval of the $6P_{3/2}$ state in ^{87}Rb using (a) a V-type energy scheme and (b) optical pumping energy scheme.

approximation and in the rotating frame is obtained using Eq. 2.11 as follows:

$$\mathrm{H} = \frac{\hbar}{2}\{\Omega_p \left|1\right\rangle \left\langle 2\right| + \Omega_c \left|1\right\rangle \left\langle 3\right| - \Delta_p \left|2\right\rangle \left\langle 2\right| - \Delta_c \left|3\right\rangle \left\langle 3\right| + \mathrm{H.c.}\}, \tag{4.1}$$

where, H.c. is Hermitian conjugate, $5\mathrm{S}_{1/2}(\mathrm{F} = 2) = \left|1\right\rangle$, $5\mathrm{P}_{3/2}(\mathrm{F} = 3) = \left|2\right\rangle$, $6\mathrm{P}_{1/2}(\mathrm{F} = 1) = \left|3\right\rangle$, $\Delta_p = \omega_p - (\omega_2 - \omega_1) + k_1 v$ is the detuning of the 780 nm laser, $k_1 = 2\pi/\lambda_1$ is the wave-vector of the 780 nm laser and λ_1 is the wavelength, v is the velocity of the atom in the direction of the probe, $\Delta_c = \omega_c - (\omega_3 - \omega_1) - k_2 v$ is the detuning of the 421 nm laser, $k_2 = 2\pi/\lambda_2$ is the wave-vector of the 421 nm laser and λ_2 is the wavelength. The Rabi frequency for the fields is $\Omega_L = -\mathrm{d}_{ij}\mathrm{E}_L e^{i\phi_L}/\hbar$ where, $\mathrm{d}_{ij} = \left\langle i\right| \hat{\mathrm{d}} \left|j\right\rangle$ is the dipole matrix element, $\hat{\mathrm{d}}$ is the atomic dipole operator, ϕ_L is the phase of the fields and subscript $L = p, c$ represent the fields (i.e., p is the probe of the 780 nm laser and c is the pump of the 421 nm laser).

The dynamics of the atom-field interactions is described by Eq. 2.15. The substitution of Eq. 4.1 into Eq. 2.15 yields the following set of equations of motion:

$$
\begin{aligned}
\dot{\rho}_{12} =& \frac{i\Omega_p}{2}(\rho_{11}-\rho_{22}) - \frac{i\Omega_c}{2}\rho_{32} - \gamma_{12}\rho_{12},\\
\dot{\rho}_{13} =& \frac{i\Omega_c}{2}(\rho_{11}-\rho_{33}) - \gamma_{13}\rho_{13} - \frac{i\Omega_p}{2}\rho_{23},\\
\dot{\rho}_{22} =& \frac{i\Omega_p}{2}\rho_{21} - \frac{i\Omega_p^*}{2}\rho_{12} - \Gamma_2\rho_{22},\\
\dot{\rho}_{23} =& -\frac{i\Omega_p^*}{2}\rho_{13} + \frac{i\Omega_c}{2}\rho_{21} - \gamma_{23}\rho_{23},\\
\dot{\rho}_{33} =& -\frac{i\Omega_c^*}{2}\rho_{13} + \frac{i\Omega_c}{2}\rho_{31} - \Gamma_3\rho_{33},
\end{aligned}
\tag{4.2}
$$

where, $\gamma_{12} = i\Delta_p + \gamma_{12}^{dec}$, $\gamma_{13} = i\Delta_c + \gamma_{13}^{dec}$, $\gamma_{23} = i(\Delta_c - \Delta_p) + \gamma_{23}^{dec}$ and $\gamma_{ij}^{dec} = \frac{1}{2}(\Gamma_i + \Gamma_j)$ is the decoherence rates denoting the total coherence relaxation rates between states $|i\rangle$ and $|j\rangle$. The remaining density matrix equations are obtained using the population conservation law $\sum_{j=1}^{3}\rho_{jj} = 1$ and the complex conjugate $\dot{\rho}_{ji} = \dot{\rho}_{ij}^*$. The absorption of the probe field is obtained by considering the steady state solution of Eq. 4.2 in the weak probe approximation i.e., the absorption of the weak probe field is proportional to Ω_p ($\Omega_p^2 = \Omega_p^3, \cdots \approx 0$). The steady state solution is expressed as,

$$
\rho_{12} = \frac{\Omega_p\left(\frac{\Omega_c^2(i\Gamma_2 + 4\Delta_c - 2\Delta_p)}{\Gamma_2 + \Gamma_3 - 2i(\Delta_c - \Delta_p)} + i(\Gamma_3^2 + 4\Delta_c^2)\right)}{(\Gamma_3^2 + 4\Delta_c^2 + 2\Omega_c^2)\left(\frac{\Omega_c^2}{\Gamma_2 + \Gamma_3 - 2i(\Delta_c - \Delta_p)} + \Gamma_2 + 2i\Delta_p\right)}.
\tag{4.3}
$$

The absorption of the probe is proportional to the imaginary part of ρ_{12} and the Doppler broadened spectrum of Eq. 4.3, is accounted for by thermal average over all the velocities of the atoms in the vapor cell.

The Hamiltonian H of the open V-type system, is the same as that of the closed V-type system given in Eq. 4.1. However, the equations of motion will be modified to include optical pumping to the other hyperfine ground state and the ground state

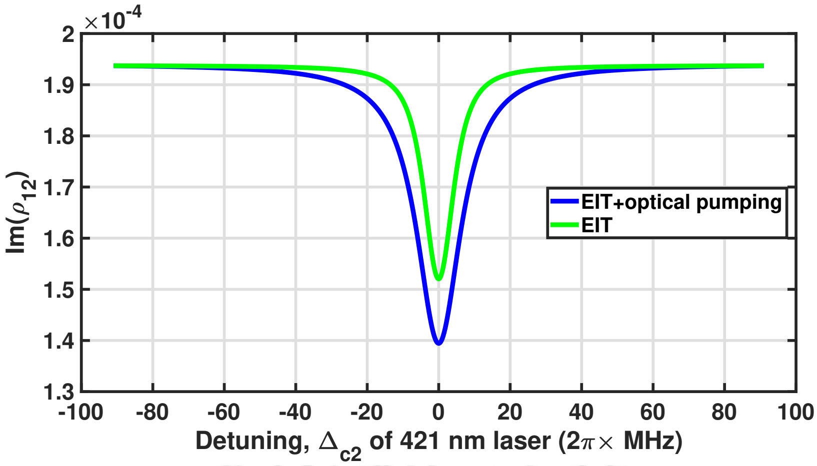

Fig. 4.2: Comparison of the transparency spectrum due to EIT plus optical pumping effects in a V-type open system (for the solution given in Eq. 4.5) and the transparency spectrum due to only EIT effect in a V-type closed system (for the solution given in Eq. 4.3). $\Omega_p = \sqrt{0.0005\Gamma_2}$, $\Omega_c = \sqrt{1.5\Gamma_3}$, $\Gamma_2 = 2\pi \times 6.065$ MHz, $\Gamma_3 = 2\pi \times 1.27$ MHz.

mixing rates as follows:

$$
\begin{aligned}
\dot{\rho}_{12} =& \frac{i\Omega_p}{2}(\rho_{11}-\rho_{22}) - \frac{i\Omega_c}{2}\rho_{32} - \gamma_{12}\rho_{12},\\
\dot{\rho}_{13} =& \frac{i\Omega_c}{2}(\rho_{11}-\rho_{33}) - \gamma_{13}\rho_{13} - \frac{i\Omega_p}{2}\rho_{23},\\
\dot{\rho}_{14} =& -\frac{i\Omega_c}{2}\rho_{34} - \gamma_{14}\rho_{14} - \frac{i\Omega_p}{2}\rho_{24},\\
\dot{\rho}_{22} =& \frac{i\Omega_{\mathrm{p}}}{2}\rho_{21} - \frac{i\Omega_p^*}{2}\rho_{12} - \Gamma_2\rho_{22},\\
\dot{\rho}_{23} =& -\frac{i\Omega_p^*}{2}\rho_{13} + \frac{i\Omega_c}{2}\rho_{21} - \gamma_{23}\rho_{23},\\
\dot{\rho}_{24} =& -\frac{i\Omega_p^*}{2}\rho_{14} - \gamma_{24}\rho_{24},\\
\dot{\rho}_{33} =& -\frac{i\Omega_c^*}{2}\rho_{13} + \frac{i\Omega_c}{2}\rho_{31} - \Gamma_3\rho_{33},\\
\dot{\rho}_{34} =& -\frac{i\Omega_c^*}{2}\rho_{14} - \gamma_{34}\rho_{34},\\
\dot{\rho}_{44} =& \Gamma_{34}\rho_{33} + \Pi_g(\rho_{11}-\rho_{44}),
\end{aligned}
\tag{4.4}
$$

where, $\gamma_{12} = i\Delta_p + \gamma_{12}^{dec}$, $\gamma_{13} = i\Delta_c + \gamma_{13}^{dec}$, $\gamma_{14} = \gamma_{14}^{dec}$, $\gamma_{23} = i(\Delta_c - \Delta_p) + \gamma_{23}^{dec}$, $\gamma_{24} = -i\Delta_p + \gamma_{24}^{dec}$, $\gamma_{34} = -i\Delta_c + \gamma_{34}^{dec}$, $\Gamma_1 = \Gamma_4 = \Pi_g$, $\gamma_{34} = i\Delta_c + \gamma_{34}^{dec}$, $\Gamma_3 = \Gamma_{31} + \Gamma_{34}$, and $\gamma_{ij}^{dec} = \frac{1}{2}(\Gamma_i + \Gamma_j)$, Γ_i is the decay rate of the i^{th} level, Γ_{31} and Γ_{34} are the decay rates of level 3 to level 1 and level 4 respectively. The remaining density matrix equations are obtained using the population conservation law $\sum_{j=1}^{4} \rho_{jj} = 1$ and the complex conjugate $\dot{\rho}_{ji} = \dot{\rho}_{ij}^{*}$. The steady state solution of Eq. 4.4 in the weak probe approximation, is expressed as follows,

$$\rho_{12} = \frac{i\Pi_g\Omega_p(\Gamma_3((\Gamma_3+\Pi_g)^2+4\Delta_c^2)+\frac{\Omega_c^2(\Gamma_2(\Gamma_3+\Pi_g)-2i\Delta_c(2\Gamma_3+\Pi_g)+2i\Delta_p(\Gamma_3+\Pi_g))}{\Gamma_2+\Gamma_3-2i(\Delta_c-\Delta_p)})}{(\Omega_c^2(\Gamma_3+\Pi_g)(\Gamma_{34}+3\Pi_g)+2\Gamma_3\Pi_g((\Gamma_3+\Pi_g)^2+4\Delta_c^2))(\frac{\Omega_c^2}{\Gamma_2+\Gamma_3-2i\Delta_c+2i\Delta_p}+\Gamma_2+\Pi_g+2i\Delta_p)}. \tag{4.5}$$

The transparency spectra of the closed V-type system (Eq. 4.3) and open V-type system (Eq. 4.5) is compared in Fig. 4.2. The transparency window due to EIT effect is further enhanced by optical pumping effect.

4.2.2 Optical Pumping Scheme

Fig. 4.1b is the energy level diagram for optical pumping scheme and the experimental setup is also given in Fig. 4.4. The 780 nm probe laser is locked to resonance on $5S_{1/2}(F = 2) \rightarrow 5P_{3/2}(F = 3)$ cycling transition and its absorption is monitored as the co-propagating 421 nm control laser beam scans around the $6P_{1/2}$ hyperfine levels on $5S_{1/2}(F = 1) \rightarrow 6P_{1/2}$ transition instead of $5S_{1/2}(F = 2) \rightarrow 6P_{1/2}$ transition. The 421 nm scanning control laser beam, partially transfers population from the lower ground hyperfine level ($5S_{1/2}(F = 1)$) to the upper ground hyperfine level ($5S_{1/2}(F = 2)$) via $5S_{1/2}(F = 1) \rightarrow 6P_{1/2}$ excitation and $6P_{1/2} \rightarrow 5S_{1/2}(F = 2)$ decay channels. Thus, optical pumping of the zero velocity group atoms to the upper ground hyperfine level [104, 105, 106] and coherence dephasing rate of the ground hyperfine levels [108, 109, 110] increases absorption of the probe giving rise to Doppler-free peaks. Since all velocity group atoms are optically pumped from $5S_{1/2}(F = 1)$ to $5S_{1/2}(F = 2)$ ground hyperfine level, extra peaks will form outside the main spectrum.

The EA spectrum is theoretically modeled by considering the Hamiltonian H of a four level optical pumping system in Fig. 4.1b under electric-dipole and rotating-wave approximation and in the rotating frame is obtained using Eq. 2.11 as follows:

$$\mathrm{H} = \frac{\hbar}{2}\{\Omega_p |1\rangle\langle 2| + \Omega_c |4\rangle\langle 3| - \Delta_p |2\rangle\langle 2| - \Delta_c |3\rangle\langle 3| + \mathrm{H.c.}\}, \tag{4.6}$$

where, $5\mathrm{S}_{1/2}(\mathrm{F}=2) = |1\rangle$, $5\mathrm{P}_{3/2}(\mathrm{F}=3) = |2\rangle$, $6\mathrm{P}_{1/2}(\mathrm{F}=1) = |3\rangle$ and $5\mathrm{S}_{1/2}(\mathrm{F}=1) = |4\rangle$. The dynamics of the atom-field interactions is similarly obtained from Eq. 2.15 and 4.6 which gives the following set of equations of motion:

$$\begin{aligned}
\dot{\rho}_{12} &= \frac{i\Omega_p}{2}(\rho_{11} - \rho_{22}) - \gamma_{12}^{dec}\rho_{12}, \\
\dot{\rho}_{13} &= -\frac{i\Omega_p}{2}\rho_{23} + \frac{i\Omega_c^*}{2}\rho_{14} - \gamma_{13}\rho_{13}, \\
\dot{\rho}_{14} &= -\frac{i\Omega_p}{2}\rho_{24} + \frac{i\Omega_c}{2}\rho_{13} - \gamma_{14}\rho_{14}, \\
\dot{\rho}_{22} &= -\frac{i\Omega_p^*}{2}\rho_{12} + \frac{i\Omega_p}{2}\rho_{21} - \Gamma_2\rho_{22}, \\
\dot{\rho}_{23} &= -\frac{i\Omega_p^*}{2}\rho_{13} - \gamma_{23}\rho_{23} + \frac{i\Omega_c^*}{2}\rho_{24}, \\
\dot{\rho}_{24} &= -\frac{i\Omega_p^*}{2}\rho_{14} - \gamma_{24}\rho_{24} + \frac{i\Omega_c}{2}\rho_{23}, \\
\dot{\rho}_{33} &= -\frac{i\Omega_c}{2}\rho_{43} + \frac{i\Omega_c^*}{2}\rho_{34} - \Gamma_3\rho_{33}, \\
\dot{\rho}_{34} &= -\frac{i\Omega_c}{2}(\rho_{33} - \rho_{44}) - \gamma_{34}\rho_{34}, \\
\dot{\rho}_{44} &= -\frac{i\Omega_c^*}{2}\rho_{34} + \frac{i\Omega_c}{2}\rho_{43} + \Gamma_{34}\rho_{33} + \Pi_g(\rho_{11} - \rho_{44}),
\end{aligned} \tag{4.7}$$

where, $\gamma_{12} = i\Delta_p + \gamma_{12}^{dec}$, $\gamma_{13} = \gamma_{13}^{dec}$, $\gamma_{14} = i\Delta_c + \gamma_{14}^{dec}$, $\gamma_{23} = -i\Delta_p + \gamma_{23}^{dec}$, $\gamma_{24} = i(\Delta_c - \Delta_p) + \gamma_{24}^{dec}$, $\gamma_{34} = i\Delta_c + \gamma_{34}^{dec}$, $\Gamma_1 = \Gamma_4 = \Pi_g$, $\Gamma_3 = \Gamma_{31} + \Gamma_{34}$ and $\gamma_{ij}^{dec} = \frac{1}{2}(\Gamma_i + \Gamma_j)$ is the decoherence rates denoting the total coherence relaxation rates between states $|i\rangle$ and $|j\rangle$. The remaining density matrix equations are similarly obtained using the population conservation law $\sum_{j=1}^{4}\rho_{jj} = 1$ and the complex conjugate $\dot{\rho}_{ji} = \dot{\rho}_{ij}^*$. The steady state solution of Eq. 4.7 in the weak probe approximation which gives enhanced absorption spectrum of the probe is expressed as follows,

$$\rho_{12} = \frac{i\Omega_p(\Omega_c^2(\Gamma_3 + \Pi_g)(\Gamma_{31} + \Pi_g) + \Gamma_3\Pi_g((\Gamma_3 + \Pi_g)^2 + 4\Delta_c^2))}{(\Gamma_2 + \Pi_g + 2i\Delta_p)(\Omega_c^2(\Gamma_3 + \Pi_g)(\Gamma_{31} + 3\Pi_g) + 2\Gamma_3\Pi_g((\Gamma_3 + \Pi_g)^2 + 4\Delta_c^2))}. \tag{4.8}$$

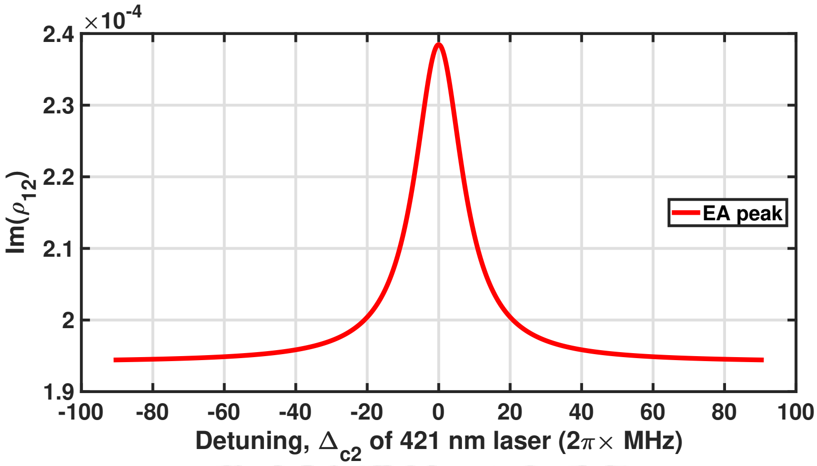

Fig. 4.3: Enhanced absorption (EA) spectrum of optical pumping system for the solution given in Eq. 4.8. $\Omega_p = \sqrt{0.0005}\Gamma_2$, $\Omega_c = \sqrt{1.5}\Gamma_3$, $\Gamma_2 = 2\pi \times 6.065$ MHz, $\Gamma_3 = 2\pi \times 1.27$ MHz.

The expression in Eq. 4.8, gives enhanced absorption (EA) line profile of the probe for the optical pumping system. The Doppler broadened spectrum of the probe, is obtained by thermal averaging of Eq. 4.8 over all the velocities of the atoms in the vapor cell and is shown in Fig. 4.3.

4.3 Experimental Details

4.3.1 Set-up and Results

The 780 nm beam is generated from (thorlab laser diode L785H1) a home-assembled extended cavity diode laser (ECDL) with typical linewidth of 500 kHz. The error signal for locking the 780 nm laser is generated by frequency modulation using the current of ECDL at 50 kHz. The error is fed to the piezo using a home-made analog PID controller for locking to the particular transition. The 421 nm beam is generated from a commercially available ECDL (TOPTICA with model no. DL PRO HP) with output power of 70 mW and linewidth of < 200 kHz.

In the experimental setup given in Fig. 4.4, the 421 nm laser beam addressing the $6P_{1/2}$ hyperfine level is divided into two laser beams. The first laser beam is passed directly through the Rb vapor cell and co-propagates with one of the 780 nm probe laser. The second 421 nm laser beam is passed through the acousto-optic modulator (AOM) twice and its frequency is shifted to be approximately the hyperfine splitting interval value. The double-pass AOM configuration has the advantage of preserving the direction of propagation of the laser beam as the frequency of AOM is changed [111]. The AOM frequency in the double-pass setup is shifted between $130-136$ MHz. The double passed laser beam through the AOM, is also passed through the same Rb vapor cell where it co-propagate with the second 780 nm probe laser. The two sets of co-propgating 421 nm and 780 nm laser are around 12 mm apart in the same cell. The single-mode operation of the 421 nm laser is monitored using a confocal Fabry-Pérot interferometer with free spectral range of 150 MHz. The beam diameter of the 780 nm probe laser is 2×3 mm with measured power of 42 μW (or peak intensity, $I = 1.8$ mW/cm^2 and corresponding Rabi frequency of $2\pi \times 4.3$ MHz). The beam diameter of the 421 nm control laser is 3×4 mm with measured power of 1.0 mW and calculated peak intensity, $I = 20.1$ mW/cm^2. The intensity corresponds to Rabi frequency of $2\pi \times 1.2$ MHz using the dipole moment in reference [51].

The transparency spectrum of $5S_{1/2}(F = 1) \rightarrow 6P_{1/2}$ weak transition and the absorption spectrum of $5S_{1/2}(F = 2) \rightarrow 6P_{1/2}$ weak transition driven by 421 nm laser is shown in Fig. 4.5a and 4.5b respectively. The spectra are recorded using a commercially available PC-based oscilloscope (i.e., USB oscilloscope which is called picoscope from Pico Technology) through the changes in the absorption spectrum of 780 nm probe laser driving $5S_{1/2}(F = 2) \rightarrow 5P_{3/2}(F = 3)$ strong transition.

Besides the two hyperfine peaks due to groups of atoms with velocities around zero, there are other extra peaks outside the main spectrum. Since the linewidth of the transition is finite, the extra peaks are caused by groups of atoms moving with velocities around 208 m/s and 330 m/s respectively. Atoms moving with ve-

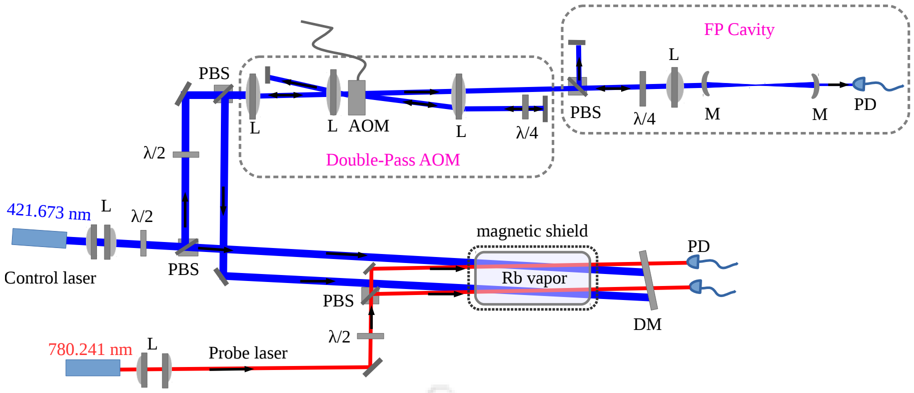

Fig. 4.4: Experimental setup for measuring hyperfine structure using coherent control and optical pumping schemes. L: Plano-convex lens; $\lambda/2$: half-wave plate; $\lambda/4$: quarter-wave plate; M: confocal mirror; DM: Dichroic mirror; PBS: polarization beam splitter; PD: photo-diode; AOM: acousto-optic modulator; FP: Fabry-Pérot cavity.

locities around 208 m/s will see the 780 nm probe laser to be on resonance with $5S_{1/2}(F = 2) \rightarrow 5P_{3/2}(F = 2)$ transition. The corresponding two extra peaks are separated by the hyperfine splitting interval of the $6P_{1/2}$ state and are located at 494 MHz from the main peaks respectively. Similarly, atoms moving with velocities around 330 m/s will be resonant for $5S_{1/2}(F = 2) \rightarrow 5P_{3/2}(F = 1)$ transition and another two fold of extra peaks are located at 783 MHz from the main peaks.

The theoretical plot in Fig. 4.5 is generated using the density matrix calculation for a seven-level system in a Doppler-broadened Rb atomic vapors at room temperature (300 K). Due to non-linearity in the scan of the laser, there is a mismatch of the extra peaks position between the experiment and theory. The linewidth of the experimental spectrum for the plot in Fig. 4.5a ranges between 29 and 31 MHz and the theoretical simulation curve has a linewidth of 26 MHz. While the linewidth of the experimental spectrum for the plot in Fig. 4.5b ranges between 29 and 34 MHz and linewidth for theoretical simulation curve is 23 and 34 MHz. However, this linewidth is larger than the natural linewidth ($6.065 + 1.27$ MHz) due to the residual (or partial) two-photon Doppler broadening in the double resonancy spectroscopy and optical pumping of

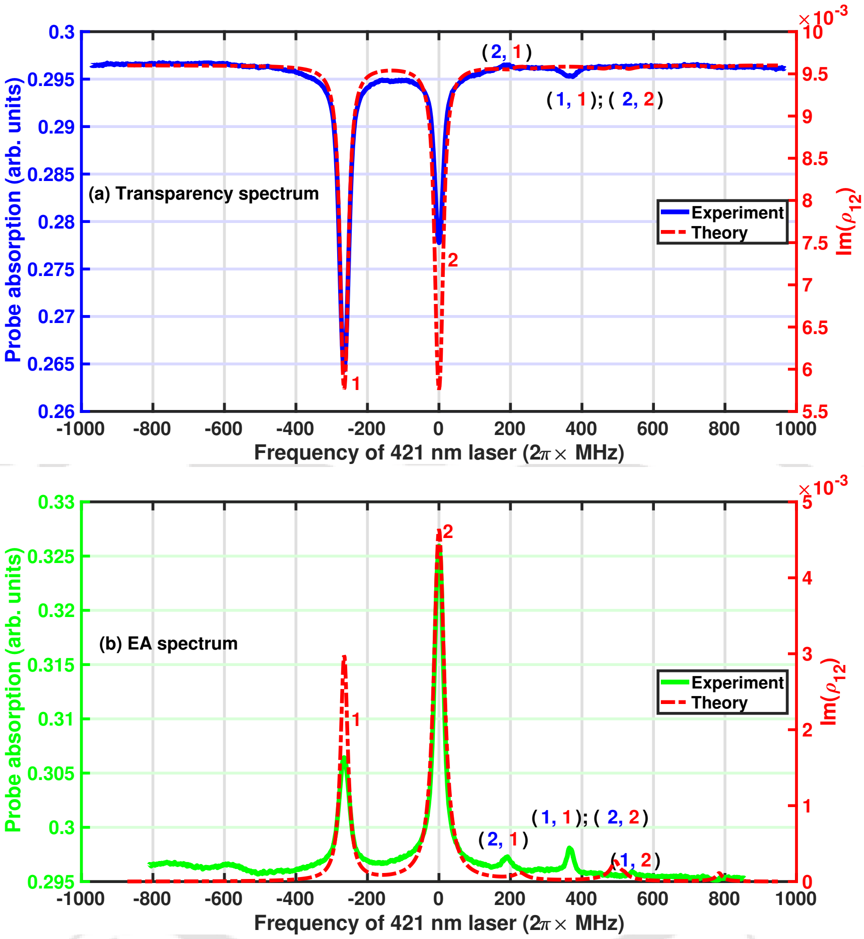

Fig. 4.5: Theoretical and experimental spectrum of the $6P_{1/2}$ hyperfine levels in ^{87}Rb. The spectra in Fig. 4.5a corresponds to the configuration of Fig. 4.1a while the spectra in Fig. 4.5b corresponds to the configuration of Fig. 4.1b.

population to the other ground state hyperfine level. The partial two-photon Doppler broadening arises from the thermal motion of the atoms and wavelength mismatch between the 780 nm probe and 421 nm control lasers [112].

The red and black traces of the experimental spectrum in Fig. 4.6 corresponds to unshifted and shifted AOM beams respectively. One of the traces is deliberately inverted to see the matching of the two hyperfine peaks for the shifted and unshifted spectrum. The matching of the peaks is a measure of shifting the frequency of the laser beam by exactly the hyperfine splitting interval. The frequency difference (Δ_{diff}) between the two peaks being matched is obtained by fitting the peaks with a Lorentzian line profile (see Fig. 4.6) and finding the difference in the peaks location. Fig. 4.7 shows a plot of frequency shift (2× AOM frequency) vs the frequency difference between the two peaks (Δ_{diff}). The hyperfine splitting interval is obtained using a linear fit on the plot of frequency shift vs Δ_{diff}. The frequency shift corresponding to zero frequency difference ($\Delta_{\text{diff}} = 0$) in the linear fit is the hyperfine splitting interval ($\mathcal{V}_{\text{hfs}}$). This method removes the error due to scan non-linearity and hence improves the precision of measurement. From the linear fit, a value of $\mathcal{V}_{\text{hfs}} = 265.13 \pm 0.040$ MHz for the coherent control scheme and $\mathcal{V}_{\text{hfs}} = 265.19 \pm 0.034$ MHz for the optical pumping scheme is obtained.

4.3.2 Errors

4.3.2.1 Systematic Errors

The main source of the systematic errors is the light shift and stray magnetic field through Zeeman shift. The systematic error arising due to stray magnetic field is minimized using a μ-metal magnetic shield around the Rb cell. The residual fields is below 1 mG which corresponds to errors less than 1 kHz. The light shift error is

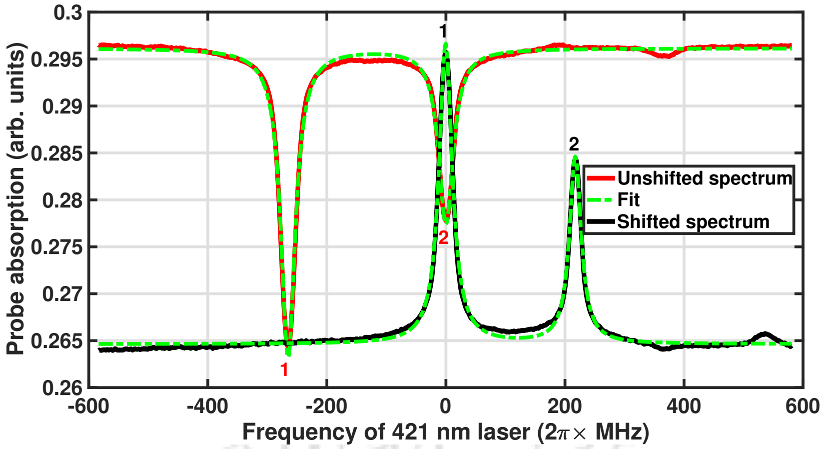

Fig. 4.6: Spectrum of shifted (black color) and unshifted (red color) beams fitted with a lorentzian line profile (dashed green color) to obtain frequency difference (Δ_{diff}) between the matched peaks.

due to presence of the hyperfine levels and the lasers driving simultaneously many levels off resonance causing the light shift of the levels driven resonantly. The locked probe laser on $5S_{1/2}(F = 2) \rightarrow 5P_{3/2}(F = 3)$ cycling transition, also drives $5S_{1/2}(F = 2) \rightarrow 5P_{3/2}(F = 2(1))$ transitions off resonance causing the light shift to the ground state $5S_{1/2}(F = 2)$ upward and excited state $5P_{3/2}(F = 3)$ downwards. However, this shift does not cause any error for hyperfine splitting interval because it will cause equal shift in the resonance for both the hyperfine levels of $6P_{1/2}$. The scanning control laser is the source of systematic error in the measurement of hyperfine splitting interval. This is because, when it is resonant on $5S_{1/2}(F = 2) \rightarrow 6P_{1/2}(F = 1)$ transition, it also driving the $5S_{1/2}(F = 2) \rightarrow 6P_{1/2}(F = 2)$ transition off resonance (negative detuning equal to hyperfine splitting interval, $\mathcal{V}_{\text{hfs}}$) causing the ground state $5S_{1/2}(F = 2)$ to shift downwards by $\Omega^2/4\mathcal{V}_{\text{hfs}}$. This effect causes resonant frequency for $5S_{1/2}(F = 2) \rightarrow 6P_{1/2}(F = 1)$ transition to shift by $+\Omega^2/4\mathcal{V}_{\text{hfs}}$. Similarly, when the control laser is resonant on $5S_{1/2}(F = 2) \rightarrow 6P_{1/2}(F = 2)$ transition, it is also driving the $5S_{1/2}(F = 2) \rightarrow 6P_{1/2}(F = 1)$ transition off resonance (positive detuning equal to hyperfine splitting interval) causing the ground state $5S_{1/2}(F = 2)$ to shift upwards by $\Omega^2/4\mathcal{V}_{\text{hfs}}$. This causes resonant frequency for $5S_{1/2}(F = 2) \rightarrow 6P_{1/2}(F = 2)$ transition to shift by $-\Omega^2/4\mathcal{V}_{\text{hfs}}$. The overall light shift error calculated using the

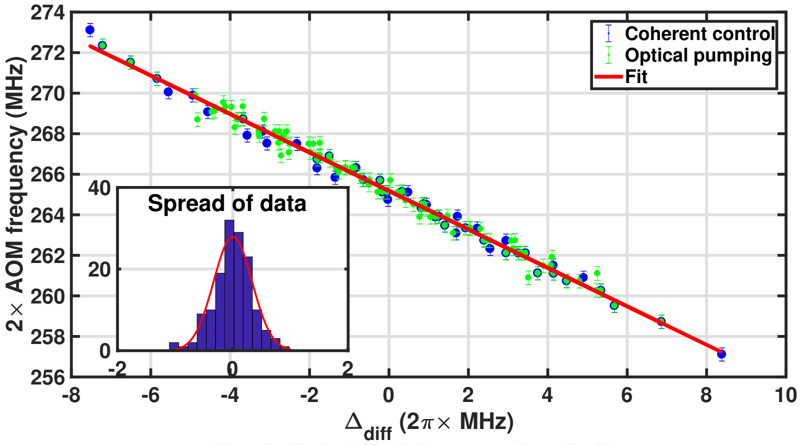

Fig. 4.7: A plot of frequency shift (2× AOM frequency) vs frequency difference (Δ_{diff}) for the two schemes. The inset shows the spread of data from the mean hyperfine splitting interval.

laser intensities in the previous section is 13 kHz and 6 kHz for the coherent control scheme and the optical pumping scheme respectively. Therefore, the total systematic errors is 14 kHz and 7 kHz for the coherent control scheme and the optical pumping scheme respectively.

4.3.2.2 Statistical Error

The above systematic error is much smaller than the statistical error in the experiment. The non-linear scan of the laser is the main cause of the statistical error. This error is minimized by shifting AOM frequency within a small range of frequencies around the neighboring hyperfine level. To quantify the statistical error, two traces (shifted and unshifted spectrum) are recorded on two input channels of the commercially available PC-based oscilloscope (called the picoscope) with averaging of 20. Three such samples are taken for each AOM frequencies and the spread of the data (Δ_{diff}) is shown by the histogram in the inset of Fig. 4.1. The spread of the data gives the statistical error in the experiment and is extracted from the histogram using a Gaussian fit [113]. The extracted statistical error and is 326 kHz for the coherent control scheme and 337 kHz for the optical pumping scheme.

Tab. 4.1: Hyperfine splitting interval ($\mathcal{V}_{\text{hfs}}$) and magnetic dipole constant A for $6P_{1/2}$ state in ^{87}Rb. The number indicated in normal bracket is the statistical plus fitting error and in curly bracket is systematic error.

	$\mathcal{V}_{\text{hfs}}$ (MHz)	A (MHz)	Reference
Coherent control	265.13(40)	132.57(20)	This work
Optical pumping	265.19(40)	132.60(20)	This work
	265.12(66)	133.24(28)	[21]
	265		[114]
		132.56(3)	[55, 73]

In summary, the statistical error is dominating over systematic errors (light shift and stray magnetic field errors) and fitting error. The total error is about 400 kHz for the coherent control scheme and the optical pumping scheme respectively. Hence the hyperfine splitting interval in the case of coherent control scheme is $\mathcal{V}_{\text{hfs}} = 265.13(40)$ MHz and optical pumping scheme is $\mathcal{V}_{\text{hfs}} = 265.19(40)$ MHz. The measured hyperfine splitting interval is related to the magnetic dipole hyperfine constant, $A = \mathcal{V}_{\text{hfs}}(F \rightarrow F-1)/F$. The values of A are 132.57(20) MHz and 132.60(20) MHz for the two schemes respectively. A comparison of hyperfine splitting interval ($\mathcal{V}_{\text{hfs}}$) and magnetic dipole constant A with the earlier works is given in Tab. 4.1. Figure 4.8 gives a graphical representation comparing the results of the hyperfine splitting interval with the earlier works given in Tab. 4.1 for the $5S_{1/2} \rightarrow 6P_{1/2}$ transition of ^{87}Rb.

The result of this chapter appear in the following publication: Journal of Physics B: Atomic, Molecular and Optical Physics (J. Phys. B: At. Mol. Opt. Phys. 53 (2020) 095001 (6pp); https://doi.org/10.1088/1361-6455/ab7670).

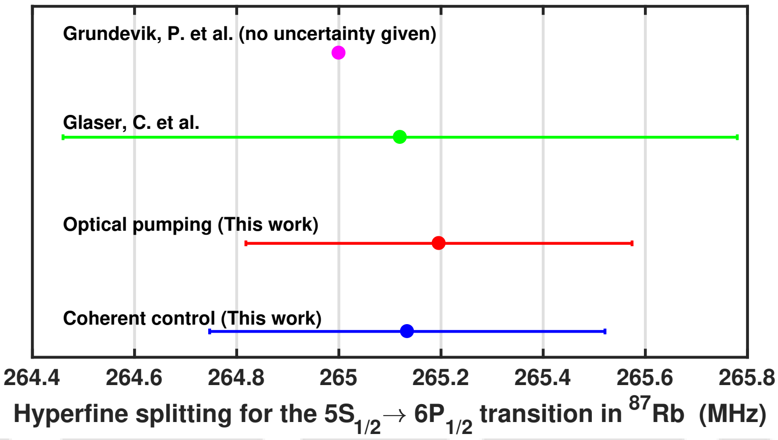

Fig. 4.8: Comparison of the measured hyperfine splitting interval for the $5S_{1/2} \rightarrow 6P_{1/2}$ transition of ^{87}Rb.

5

Role of velocity induced population oscillation in saturated fluorescence spectroscopy

5.1 Introduction

This chapter describes a theoretical framework to identify the role of velocity induced population oscillation (VIPO) in saturated fluorescence spectroscopy in a two-level system which is a very useful spectroscopic technique for weak transitions. The fluorescence dip in a fluorescence spectra is generally explained as a saturation effect (also known as velocity selective saturation, VSS). However in this work, we find that the Doppler-free dip in a fluorescence spectra is due to both the VSS and VIPO effects. The fluorescence dip is further modified by Doppler averaging and its linewidth and dip height are dependent on the temperature of the atomic gas and the applied laser beam intensity. For an atomic beam, the shift of the fluorescence dip from the line center is dependent on the average velocity of the atomic beam and the misalignment of the laser beams with respect to the atomic beam.

The chapter begins with a detailed theoretical description of the VSS and VIPO effects, which induce a dip in the fluorescence spectra. The the subsequent sections of the chapter discusses the effect of the atomic gas temperature and the applied laser intensity on the fluorescence dip profile. The last section of the chapter presents a detailed discussion on the fluorescence dip in the case of an atomic beam and the effects of laser beams misalignment.

5.2 Theoretical Formulations

Fig. 5.1 shows the schematic diagram of the saturated fluorescence spectroscopy and the energy level diagram for a two-level system (TLS). The numerical calculations for this work, considers the parameters for the intercombination line in Yb of the transition $6s^2$; $^1S_0$; m = 0 → 6s6p; $^3P_1$; m=0. However, features hold true for the other element's parameters as well. The first configuration of the saturated fluorescence spectroscopy is shown in Fig. 5.1b where the laser beam is passed through an absorption cell and retro-reflected across the cell by the mirror M1 as a counter-propagating beam. The second configuration is shown in Fig. 5.1c where the laser beam is passed through the effusive atomic source normally and retro-reflected by the mirror M1 as a counter-propagating beam. The electric field associated with the transition $|i\rangle \leftrightarrow |j\rangle$ is of the form:

$$\vec{\mathrm{E}} = \vec{\mathrm{E}}_1 \cos(\omega_1 t) + \vec{\mathrm{E}}_2 \cos(\omega_2 t), \tag{5.1}$$

where, ω_1 & ω_2 are the laser frequencies and $\vec{\mathrm{E}}_1$ & $\vec{\mathrm{E}}_2$ are the amplitudes of field 1 and 2 respectively. Field 1 is the laser beam passing through the absorption cell or effusive atomic source and field 2 is the beam retro-reflected by mirror M1 into the cell as a counter-propagating beam. The Rabi frequency for the fields is $\Omega_\mathrm{L} = -\mathrm{d}_{ij}\mathrm{E}_\mathrm{L} e^{i\phi_\mathrm{L}}/\hbar$ where, $\mathrm{d}_{ij} = \langle i|\,\hat{\mathrm{d}}\,|j\rangle$ is the dipole matrix element, $\hat{\mathrm{d}}$ is the atomic dipole operator, ϕ_L is the phase of the fields and subscript $\mathrm{L} = 1, 2$ represent the laser fields.

The Hamiltonian $\mathrm{H} = \mathrm{H}_0 + \mathrm{H}_\mathrm{I}$ of the system under electric-dipole and rotating-wave

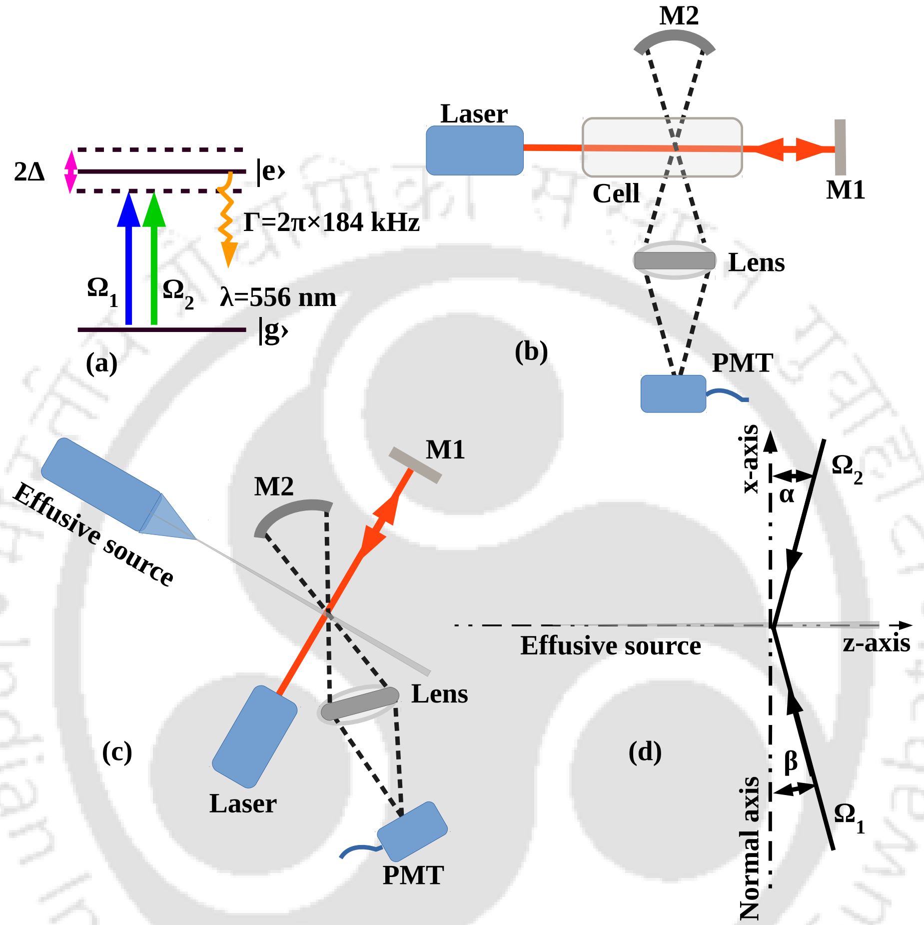

Fig. 5.1: Schematic diagram of a two-level system interacting with counter-propagating fields. (a) Energy level diagram of Yb at the intercombination line (^{1}S$_0$, m=0→ ^{3}S$_1$, m=0) similar to [30]. Schematic for saturated fluorescence in (b) a vapor cell (c) a atomic beam or effusive source and (d) illustrates the misalignment of the laser beams along the atomic beam; the misalignment of Ω_2 across the atomic beam (i.e., out of plane) by an angle ϕ is not shown.

approximation is obtained using Eq. 2.2 and 2.6 and is expressed as follows:

$$\begin{aligned}
\mathrm{H}_0 =& \hbar\omega_g |g\rangle\langle g| + \hbar\omega_e |e\rangle\langle e|, \\
\mathrm{H}_\mathrm{I} =& \frac{\hbar}{2}\Big[\{\Omega_1 + \Omega_2 e^{i((\omega_2 - kv_x)-(\omega_1+kv_x))t}\} e^{i((\omega_1+kv_x)t)} |g\rangle\langle e| + \mathrm{H.c.}\Big],
\end{aligned} \tag{5.2}$$

where, H.c. is Hermitian conjugate, H_0 is the Hamiltonian of the atom without interaction, H_I is the Hamiltonian describing atom-field interaction and $\hbar\omega_j (j = g, e)$ is the energy of state $|j\rangle$. In the rotating frame of field 1, the total Hamiltonian $\tilde{\mathrm{H}}$ of the system is calculated using Eq. 5.2 and 2.11 which is expressed as follows:

$$\tilde{\mathrm{H}} = \frac{\hbar}{2}\{(\Omega_1 + \Omega_2 e^{i\delta t}) |g\rangle\langle e| - 2\Delta_1 |e\rangle\langle e| + \mathrm{H.c.}\}, \tag{5.3}$$

where, $\delta = (\omega_2 - kv_x) - (\omega_1 + kv_x) = -2kv_x$ is the Doppler frequency difference between fields 1 and 2 since the two laser fields are from the same laser source i.e., $\omega_2 = \omega_1$, $k = 2\pi/\lambda$ is the wave-vector of the fields with wavelength λ, v_x is the velocity of the atom in the direction of field 2 and $\Delta_1 = \omega_1 - (\omega_e - \omega_g) + kv_x$ is the detuning of the fields. The dynamics of the atom-field interactions is obtained by the substitution of Eq. 5.3 into Eq. 2.15 which yields the following set of equations of motion with time-dependent coefficients:

$$\begin{aligned}
\dot{\rho}_{gg} =& \frac{i}{2}(\Omega_1^* + \Omega_2^* e^{-i\delta t})\rho_{ge} - \frac{i}{2}(\Omega_1 + \Omega_2 e^{i\delta t})\rho_{eg} + \Gamma\rho_{ee}, \\
\dot{\rho}_{ge} =& \frac{i}{2}(\Omega_1 + \Omega_2 e^{i\delta t})\rho_{gg} - (\frac{\Gamma}{2} + i\Delta_1)\rho_{ge} - \frac{i}{2}(\Omega_1 + \Omega_2 e^{i\delta t})\rho_{ee}, \\
\dot{\rho}_{eg} =& -\frac{i}{2}(\Omega_1^* + \Omega_2^* e^{-i\delta t})\rho_{gg} - (\frac{\Gamma}{2} - i\Delta_1)\rho_{eg} + \frac{i}{2}(\Omega_1^* + \Omega_2^* e^{-i\delta t})\rho_{ee}, \\
\dot{\rho}_{ee} =& -\frac{i}{2}(\Omega_1^* + \Omega_2^* e^{-i\delta t})\rho_{ge} + \frac{i}{2}(\Omega_1 + \Omega_2 e^{i\delta t})\rho_{eg} - \Gamma\rho_{ee}.
\end{aligned} \tag{5.4}$$

In the considered two level atomic system interacting with a pair of counter-propagating fields, the coupling strength is given as $\Omega_1 = \Omega_2 = \Omega$ and detuning $\Delta_1 = \Delta_2 = \Delta$ i.e., the two laser fields have equal intensity and detuning. The temporal behaviour of the coefficients in Eq. 5.4 is velocity dependent, i.e., $\delta = -2kv_x$ which is caused

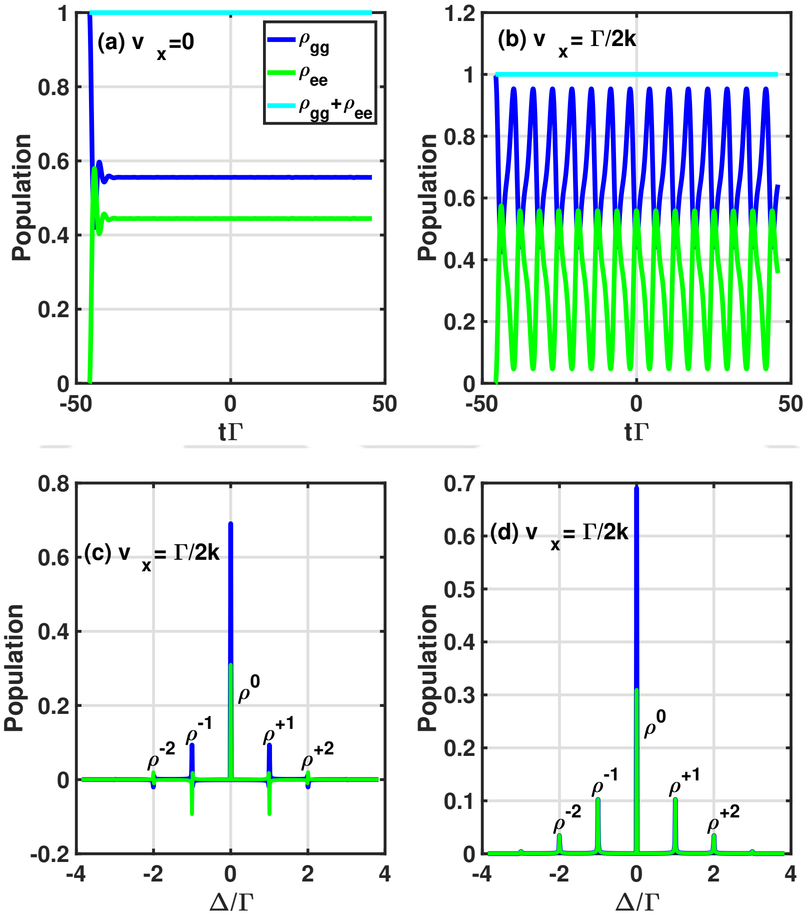

Fig. 5.2: (a) Steady state of population for atoms with velocity $v_x = 0$, (b) population oscillation for atoms with velocity $v_x = \Gamma/2k$, (c) Fourier transform of the oscillating population and (d) absolute value of Fourier transform of the oscillating population.

by the Doppler effect. For zero velocity the time evolution of the density matrix element will reach steady state behavior as shown in Fig. 5.2a. However, for the non-zero velocity a periodic behavior occurs i.e., the time evolution of the density matrix will not reach steady state but instead it will oscillate at the harmonics of the beat frequency $\delta = -2kv_x$ (see Fig. 5.2b). Mathematically, the time dependence can be ignored in the specific case of zero group velocity atoms. The oscillation of the population for non-zero velocity group atoms is due to the interference of the two fields addressing the same transition giving rise to modulation of the total field at the beat frequency [64, 65, 66, 67, 68, 69, 70]. When such beating of the fields is less than or approximately equal to the inverse of the population relaxation time of the excited state, the velocity induced population oscillations (VIPO) can lead to a decreased absorption of the fields which is the source of enhanced saturated fluorescence dip in a TLS.

The time evolution of equations of motion given in Eq. 5.4 can be studied in steady state using Floquet expansion approach. In the Floquet approach, the atomic dynamics are described in terms of Fourier harmonics of the density matrix elements as follows:

$$\rho_{ij}(t) = \sum_{n=-\infty}^{\infty} \rho_{ij}^{(n)}(t) e^{in\delta t}, \tag{5.5}$$

where, $\rho_{ij}^{(n)}(t)$ (nth order) are slowly varying harmonic amplitudes and the atomic variables for the TLS will respond at harmonics of Doppler shifted frequency δ. Substitution of Eq. 5.5 into Eq. 5.4 and comparing coefficients of the same power in $n\delta$, yields the following set of steady state equations of motion for the slowly varying

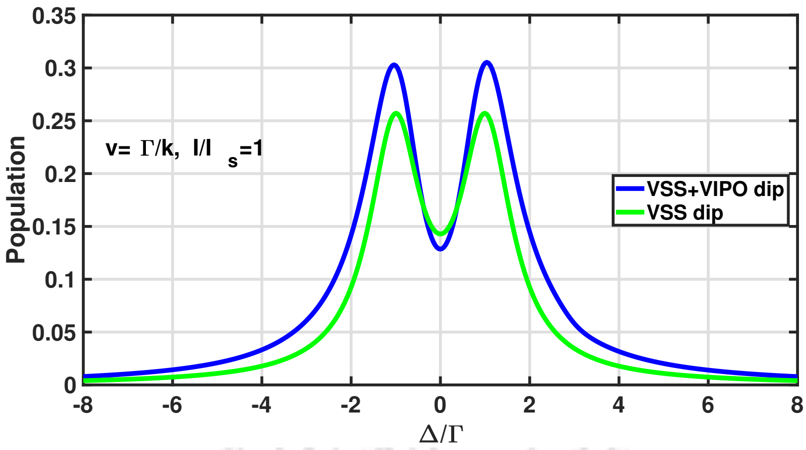

Fig. 5.3: The lineshape of the excited state population with VSS effect of the fields only (green trace) and with VSS plus VIPO effects (blue trace). The saturation parameter $\mathrm{I/I_s} = 1$ is for a single beam.

harmonic amplitudes:

$$\begin{aligned}
\dot{\rho}_{gg}^{(n)} &= -\, in\delta\rho_{gg}^{(n)} + \frac{i\Omega^*}{2}\{\rho_{ge}^{(n)} + \rho_{ge}^{(n+1)}\} - \frac{i\Omega}{2}\{\rho_{eg}^{(n)} + \rho_{eg}^{(n-1)}\} + \Gamma\rho_{ee}^{(n)}, \\
\dot{\rho}_{ge}^{(n)} &= \frac{i\Omega}{2}\{\rho_{gg}^{(n)} + \rho_{gg}^{(n-1)}\} - \{\frac{\Gamma}{2} + i\left((\Delta + kv_x) + n\delta\right)\}\rho_{ge}^{(n)} - \frac{i\Omega}{2}\{\rho_{ee}^{(n)} + \rho_{ee}^{(n-1)}\}, \\
\dot{\rho}_{eg}^{(n)} &= -\, \frac{i\Omega^*}{2}\{\rho_{gg}^{(n)} + \rho_{gg}^{(n+1)}\} + \frac{i\Omega^*}{2}\{\rho_{ee}^{(n)} + \rho_{ee}^{(n+1)}\} - \{\frac{\Gamma}{2} - i\left((\Delta + kv_x) - n\delta\right)\}\rho_{eg}^{(n)}, \\
\dot{\rho}_{ee}^{(n)} &= -\, \frac{i\Omega^*}{2}\{\rho_{ge}^{(n)} + \rho_{ge}^{(n+1)}\} + \frac{i\Omega}{2}\{\rho_{eg}^{(n)} + \rho_{eg}^{(n-1)}\} - (\Gamma + in\delta)\rho_{ee}^{(n)}.
\end{aligned} \tag{5.6}$$

The set of steady state equations of motion in Eq. 5.6 can easily be solved by numerical integration,

$$\begin{aligned}
\frac{\mathrm{d}\rho^{(n)}(v_x)}{\mathrm{dt}} &= \mathrm{A}\rho^{(n)}(v_x), \\
\rho_{ee}(v_x) &= \sum_{n=-\alpha}^{+\alpha} \rho_{ee}^{(n)}(v_x),
\end{aligned} \tag{5.7}$$

where, $\rho_{ee}(v_x)$ is the excited state population as seen in Fig. 5.3 for a single velocity group atoms and A is $n \times n$ matrix of a truncated series of the harmonic amplitudes.

In a truncated basis we replace the infinite Fourier expansion in Eq. 5.5 by a finite expansion $\rho_{ij}(t) = \sum_{n=-\alpha}^{\alpha} \rho_{ij}^{(n)}(t)e^{in\delta t}$ where α is the cut-off of the series and $\rho^{(n)} \equiv 0$ for $n > |\alpha|$.

5.2.1 Velocity selective saturation effect on fluorescence dip

In Fig. 5.2c and 5.2d the amplitude of the higher harmonics are very small for a given velocity and only a few contribute in the fluorescence spectrum. The complete match of the Doppler averaged excited state population for orders $1-5$ in Fig. 5.4a, shows that the solution of the excited state population to first order is sufficient to describe the fluorescence spectra of the TLS. The total excited state population up to first order is given as,

$$\rho_{ee} = \rho_{ee}^{(0)} + \rho_{ee}^{(+1)} + \rho_{ee}^{(-1)}. \tag{5.8}$$

The steady state analytical solution of $\rho_{ee}^{(0)}$, $\rho_{ee}^{(+1)}$ and $\rho_{ee}^{(-1)}$ are given in appendix B. The term in curly bracket in Eq. B.1 can be recognized as the excited state population in terms of saturation of the transition by the counter-propagating field for a given single velocity group atoms. The saturation of the excited state by the fields can therefore be written in terms of the saturation parameter, s, as follows:

$$\rho_{ee}^{(0)} = \frac{1}{2}\left\{\frac{\mathrm{s}_{\Delta-kv_x} + \mathrm{s}_{\Delta+kv_x}}{1 + \mathrm{s}_{\Delta-kv_x} + \mathrm{s}_{\Delta+kv_x}}\right\}, \tag{5.9}$$

where,

$$\mathrm{s}_{\Delta+kv_x} = \frac{\frac{\Omega^2}{2}}{\frac{\Gamma^2}{4} + (\Delta + kv_x)^2} \quad \text{and} \quad \mathrm{s}_{\Delta-kv_x} = \frac{\frac{\Omega^2}{2}}{\frac{\Gamma^2}{4} + (\Delta - kv_x)^2},$$

are the saturation parameter for the two beams. Similarly, in terms of the on resonance saturation parameter, $\mathrm{I}/\mathrm{I_s} = \frac{2\Omega^2}{\Gamma^2}$ (where, I & $\mathrm{I_s}$ are the laser intensity and

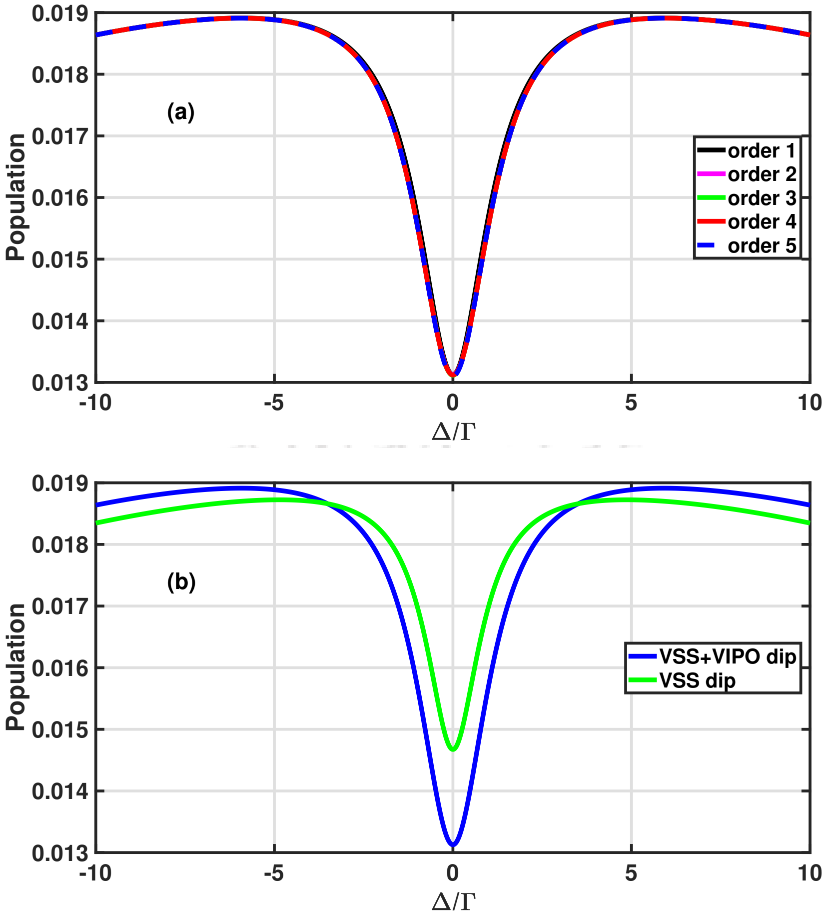

Fig. 5.4: (a) Doppler averaged excited state population for orders 1 – 5 in the density matrix. $|\Omega_2| = |\Omega_1| = 1.0\Gamma$, $\Gamma = 2\pi \times 184$ kHz [115], Temperature, $T_{tr} = 300$ mK (This is the transverse temperature corresponding to collimation of the atomic beam in the experiment [30]). (b) Doppler averaged fluorescence VSS dip (green trace) and fluorescence VSS dip enhanced by VIPO effect (blue trace).

saturation intensity respectively) the saturation of the excited state population is,

$$\rho_{ee}^{(0)} = \frac{1}{2}\left\{\frac{\frac{\mathrm{I/I_s}}{1+\frac{4(\Delta-kv_x)^2}{\Gamma^2}} + \frac{\mathrm{I/I_s}}{1+\frac{4(\Delta+kv_x)^2}{\Gamma^2}}}{1+\frac{\mathrm{I/I_s}}{1+\frac{4(\Delta-kv_x)^2}{\Gamma^2}} + \frac{\mathrm{I/I_s}}{1+\frac{4(\Delta+kv_x)^2}{\Gamma^2}}}\right\}. \tag{5.10}$$

The green trace in Fig. 5.3 shows the fluorescence dip due to VSS effect of the fields as expressed in Eq. 5.9 or 5.10. The fluorescence dip is a double peak lineshape for monokinetic atoms in counter-propagating laser beams. The scanning fields are resonant with the atom moving with velocity v_x when $\Delta + kv_x = 0$ for field 1 and $\Delta - kv_x = 0$ for field 2. The resulting excited state population lineshape is therefore a double peak spectra with peak-to-peak separation of two times the Doppler shift.

5.2.2 Velocity induced population oscillation effect on fluorescence dip

The saturation fluorescence dip in Fig. 5.3 is further modified by the VIPO effect. The effect of the VIPO is through the higher order terms such as $\rho_{ee}^{(\pm)}$. The VIPO effect leads to enhanced transparency of the fields in a narrow range of beat frequencies determined by the inverse of relaxation time of the excited state, $\delta \leq \Gamma$ [64, 65, 66, 67, 68, 69, 70]. The expression of the VIPO effect on the fluorescence dip at low power of the fields (i.e., $\mathrm{I} \ll \mathrm{I_s}$) in Eq. B.2 can be further reduced. For lower values of Ω, $\Omega^2 \gg \Omega^4$ which means in the numerator,

$$2\gamma_4\Omega^2(\gamma_2\gamma_9 + \gamma_3\gamma_8) \gg \Omega^4(2\gamma_4\gamma_5 + \gamma_2\gamma_4 + \gamma_2\gamma_6 + \gamma_3\gamma_7 + \gamma_3\gamma_4),$$

and in the denominator,

$$\begin{aligned} 2(4\gamma_1\gamma_2\gamma_3\gamma_4) \gg & 2(4\Omega^2(\gamma_2\gamma_3\gamma_{10} + \gamma_2\gamma_4\gamma_9 + \gamma_3\gamma_4\gamma_8) + \\ & \Omega^4(\gamma_2\gamma_4 + 2\gamma_2\gamma_6 + 2\gamma_4\gamma_5 + \gamma_2\gamma_3 + 2\gamma_3\gamma_7 + \gamma_3\gamma_4)). \end{aligned}$$

In this limit the terms B and C are also close to 1. The fluorescence dip due to the VIPO can then be expressed as,

$$\rho_{\mathrm{ee}}^{(+1)} = \frac{1}{2}\left\{\frac{\mathrm{I/I_s}}{1 + \frac{4(\Delta - kv_x)^2}{\Gamma^2}}\frac{\frac{\Gamma^2}{2} + 2kv_x(\Delta - kv_x)}{\Gamma^2 + (2kv_x)^2} + \frac{\mathrm{I/I_s}}{1 + \frac{4(\Delta + kv_x)^2}{\Gamma^2}}\frac{\frac{\Gamma^2}{2} - 2kv_x(\Delta + kv_x)}{\Gamma^2 + (2kv_x)^2}\right\}. \tag{5.11}$$

In general, the effect of VIPO on the fluorescence dip is well illustrated in Fig. 5.3 for single velocity and in Fig. 5.4b for the Doppler broadened media. In both cases the fluorescence dip caused by VSS effect is smaller compared to the dip caused by VSS plus VIPO effects.

The Doppler-broadened spectrum of the excited population of the atomic gas shown in Fig. 5.4 is obtained by integrating the solution of Eq. 5.8 over the velocity component along the laser beam as follows:

$$\rho_{\mathrm{ee}} = \frac{1}{\sqrt{2\pi}\tilde{v}_{tr}} \sum_{n=-\alpha}^{\alpha} \int \rho_{ee}^{(n)}(v_x) e^{-(\frac{v_x}{2\tilde{v}_{tr}})^2} \mathrm{d}v_x, \tag{5.12}$$

where, $\tilde{v}_{tr} = \sqrt{k_B T_{tr}/m}$, m is the atomic mass and T_{tr} is the temperature corresponding to velocity spread of the atomic gas along the laser beams. The limit of v_x for numerical integration in the above equation is from -$3\sqrt{2}\tilde{v}_{tr}$ to $+3\sqrt{2}\tilde{v}_{tr}$ which corresponds to a velocity distribution amplitude of $1/e^9$. In steady-state, the scattering rate, Γ_{sc}, of light from the laser fields is given as $\Gamma_{\mathrm{sc}} = \Gamma\rho_{\mathrm{ee}}$ where, ρ_{ee} is the total excited state population and Γ is the decay rate.

5.2.3 Effect of laser intensity and temperature

The important parameters of the lineshape of the saturated fluorescence dip is, its height and the linewidth which depend upon the laser intensity and temperature (i.e., the spread of the atomic velocity components along the laser beam) of the atomic gas. The saturated fluorescence dip as a function of intensity is compared for VSS plus VIPO effect (solid line) and VSS effect only (dashed line) for various temperatures (see Fig. 5.5). For the case of VSS effect only, the dip height increases with intensity and saturates for large laser intensity. However, for VSS plus VIPO effect the dip height increases with intensity, attains a maximum value and gradually decreases as the intensity is further increased. When the power broadened linewidth

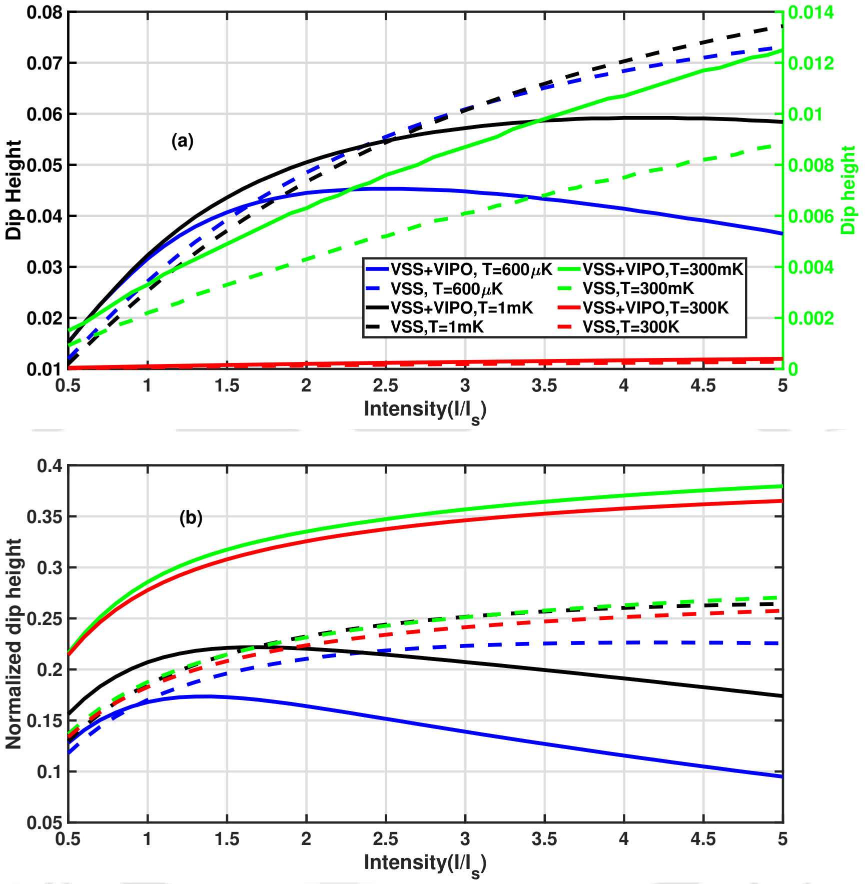

Fig. 5.5: Comparison of saturated fluorescence dip height vs laser intensity between VSS plus VIPO dip and only VSS dip given in Eq. 5.9 and 5.10. (a) Fluorescence dip before normalizing the fluorescence spectrum, (b) Fluorescence dip after normalizing the fluorescence spectrum. I/I_s is a single beam saturation parameter.

is roughly comparable to the transverse Doppler broadening i.e., $2k\sqrt{2k_BT_{tr}/m}$ is $\mathrm{O}(\Gamma\sqrt{1+\mathrm{I}/\mathrm{I_s}})$, the saturated fluorescence dip will attain a maximum value before decreasing which is a typical case at lower atomic temperature for the plotted intensity range in Fig. 5.5.

The variation of the saturated fluorescence linewidth with the applied laser intensity is plotted in Fig. 5.6. The linewidth increases with intensity of the laser beams for each atomic temperature. The power broadened natural linewidth $\Gamma\sqrt{1+\mathrm{I}/\mathrm{I_s}}$ is equal to $\sqrt{2}\Gamma$ (or 1.414Γ) when $\mathrm{I}/\mathrm{I_s} = 1$ where, $\Gamma = 2\pi \times 184$ kHz [115]. At 300 mK, the the linewidth of the VSS dip and VSS plus VIPO dip is 1.525Γ and 1.868Γ respectively when $\mathrm{I}/\mathrm{I_s} = 1$. At 300 mK, the Doppler broadening due to thermal velocity of the atoms is much higher than the power broadened linewidth for the plotted intensity range i.e., $2k\sqrt{2k_BT_{tr}/m} = 2\pi \times 19.2\ \mathrm{MHz} \gg 2\pi \times 184\sqrt{1+\mathrm{I}/\mathrm{I_s}}$ kHz. This means, the variation of the linewidth of the fluorescence dip with the applied laser intensity at room temperature (300 K) does not show any significant difference with the corresponding linewidth at 300 mK (see also Fig. 5.6 the red and green traces). However, the overall amplitude of the fluorescence dip is much lower because there is a small number of zero velocity group atoms for high temperatures(see also Fig. 5.5 the red traces before and after normalizing the fluorescence spectrum). The dip height also increases with the applied laser intensity and shows a similar behavior as the corresponding dip heights at 300 mK.

5.2.4 Effect of laser beams misalignment

The effect of the misalignment of the two laser beams with respect to the atomic beam is considered in this section. Ideally the two laser beams should be perpendicular to the atomic beam, however, the general case can be represented in Fig. 5.1d which includes the misalignment of the two laser beams. The complete Doppler-broadened spectrum of the excited population in the case of the atomic beam is obtained by inte-

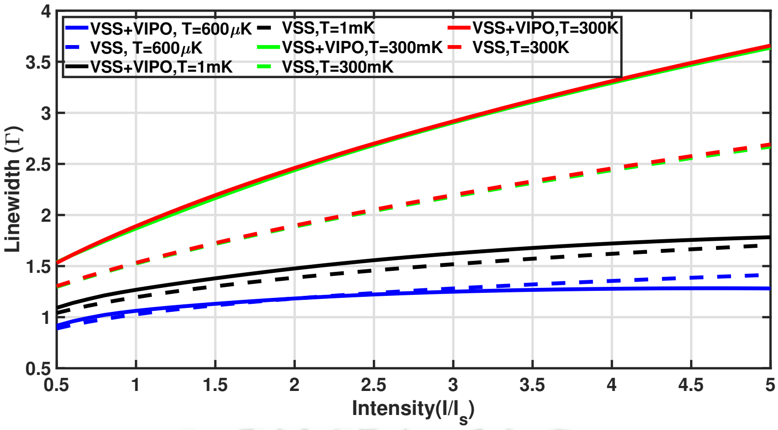

Fig. 5.6: Comparing saturated fluorescence dip linewidth vs laser intensity between VSS plus VIPO dip for various temperatures and only VSS dip given in Eq. 5.9 and 5.10. I/I$_s$ is a single beam saturation parameter.

grating the solution of Eq. 5.8 over two velocity components i.e., velocity component along the laser beam and velocity component along the atomic beam as follows:

$$\rho_{\mathrm{ee}} = \frac{1}{2\sqrt{2\pi}\tilde{v}_{tr}\tilde{v}_l^4}\sum_{n=-\alpha}^{\alpha}\iint \rho_{ee}^{(n)}(v_x, v_z)v_z^3 \times e^{-(\frac{v_x}{2\tilde{v}_{tr}})^2} e^{-(\frac{v_z}{2\tilde{v}_l})^2}\mathrm{d}v_x\mathrm{d}v_z, \qquad (5.13)$$

where, $\tilde{v}_{tr} = \sqrt{k_B T_{tr}/m}$, $\tilde{v}_l = \sqrt{k_B T_l/m}$, T_l is the temperature corresponding to the longitudinal velocity spread along the atomic beam and T_{tr} is the temperature corresponding to the transverse velocity spread along the laser beams, v_z is velocity of the atom along atomic beam (or longitudinal velocity w.r.t atomic beam) and v_x is the velocity of the atom along the laser beam (or transverse velocity w.r.t atomic beam). The limit of v_z for numerical integration in Eq. 5.13 is from 0.005m/s($\approx$ 0 and corresponds to a velocity distribution amplitude of $1/e^{32}$) to $+3\sqrt{3}\tilde{v}_l$ which corresponds to a velocity distribution amplitude of $1/e^9$. The value of T_l and T_{tr} are 673K and 200mK in the above numerical calculation. The diameter, d$_{\mathrm{beam}}$, of both laser beams are taken to be 10mm which gives a transit time broadening of $\delta_{tt} = 2(v_z^{ave}/\mathrm{d_{beam}})\sqrt{2\ln 2} = 2\pi \times 12.6$ kHz [116] where, $v_z^{ave} = \sqrt{9\pi k_B T_l/8m}$ is the average longitudinal velocity of the atomic beam. With two components of velocities (v_x and v_z), the frequency difference between Ω_2 and Ω_1 becomes $\delta = -kv_x\{\cos(\beta) +$

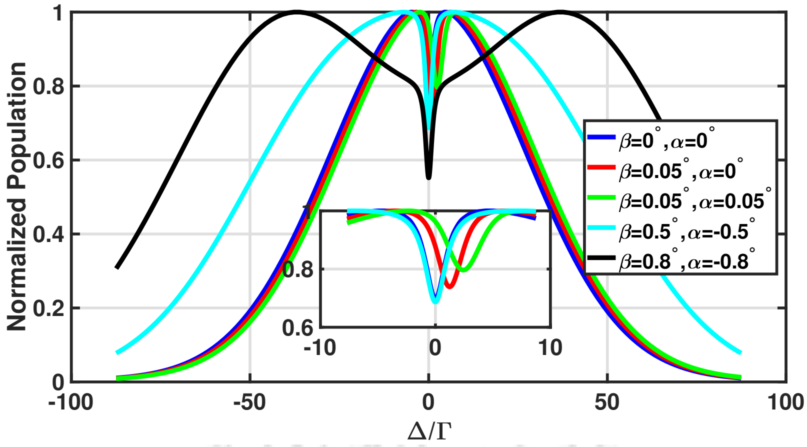

Fig. 5.7: Excited state population spectra of the atomic beam at various angles of counter-propagating laser fields. The shift of the saturated fluorescence dip is calculated from the full density matrix which includes the VSS and VIPO effects. $|\Omega_2| = |\Omega_1| = 1.0\Gamma$, $\Gamma = 2\pi \times 184$ kHz.

$\cos(\alpha)\} - kv_z\{\sin(\beta) - \sin(\alpha)\}$ in the atomic frame and the detuning, Δ_1 of Ω_1 is $\Delta + kv_x\cos(\beta) - kv_z\sin(\beta)$ where, β and α are respectively the angles made by the laser fields Ω_1 and Ω_2 with respect to the normal of the atomic beam. In an ideal situation both the laser beams should be exactly counter-propagating to each other and aligned normal to the atomic beam ($\beta = \alpha = 0$). The saturated fluorescence dip is exactly at $\Delta_1 = 0$ (the line-center) as is shown with the blue curve in Fig. 5.7.

However, there is a significant shift of the fluorescence dip in the case where only one of the laser beam Ω_2 is misaligned by a small angle e.g., $\alpha = 0.05°$ and no misalignment of Ω_1 ($\beta = 0$). The saturated fluorescence dip shift from the line-center a shown by the red curve with a decreased amplitude. If both the laser beams are misaligned by the same angle e.g., $\alpha = \beta = 0.05°$ the shift of the fluorescence dip is doubled with a decreased amplitude a shown by the green curve. The effect of misalignment of the laser beams results in the shift of the saturated fluorescence dip from resonance by $\Delta_{shift} = \frac{1}{2}kv_z^{ave}\{\sin(\beta) + \sin(\alpha)\}$ with a decreased dip height for each shift. The frequency shift of the VSS dip with misalignment given in Fig. 5.7 includes both VSS and VIPO effects. We have also considered calculation with the

VSS effect only and the shifts are precisely the same, however, the dip amplitude is higher when the VIPO effect is included. The shifts of the fluorescence dip depends on the average velocity of the atomic beam and the angles of misalignment of the laser beams, which means both the VSS dip and VSS plus VIPO dip will shift equally. In the case where both the laser beams are misaligned by same amount (e.g., 0.8°) but exactly counter-propagating ($\beta = -\alpha$), the fluorescence dip is comprised of a wide dip due to the longitudinal velocity and the narrow dip due to the transverse velocity as shown with black curve. For large misalignment w.r.t the atomic beam but exactly counter-propagation of the two laser beams, the narrow fluorescence dip due to the transverse velocity disappear and only the wide dip is observed. This is because Doppler broadening effect due to the longitudinal velocity dominates over Doppler broadening of the transverse velocity since $v_z \gg v_x$.

The laser beams can also be misaligned across the atomic beam rather than along the direction of the atomic beam. With regard to Fig. 5.1d, this would mean inclining one of the beams out of the plane of the page at an angle ϕ (in this case we consider the misalignment of Ω_2). The misalignment introduces an additional Doppler shift due to the velocity component v_y across the atomic beam in a direction which is perpendicular to v_x. With the three velocity components (v_x, v_y and v_z), the frequency difference between Ω_2 and Ω_1 becomes $\delta = -kv_x\{\cos(\beta)+\cos(\alpha)\cos(\phi)\}-kv_y\sin(\phi)-kv_z\{\sin(\beta)-\sin(\alpha)\}$ in the atomic frame and the detuning, Δ_1 of Ω_1 is $\Delta+kv_x\cos(\beta)-kv_z\sin(\beta)$. The Doppler-broadened spectrum of the excited population in Eq. 5.13 is now integrated over the three velocity components (v_x, v_y and v_z) as follows,

$$\rho_{\mathrm{ee}} = \frac{1}{4\pi\tilde{v}_{tr}^2\tilde{v}_l^4}\sum_{n=-\alpha}^{\alpha}\iiint \rho_{ee}^{(n)}(v_x, v_y, v_z)v_z^3 \times e^{-\frac{v_x^2+v_y^2}{(2\tilde{v}_{tr})^2}} e^{-(\frac{v_z}{2\tilde{v}_l})^2}\mathrm{d}v_x\mathrm{d}v_y\mathrm{d}v_z. \tag{5.14}$$

The additional misalignment of the laser beams a cross the atomic beam results in the shift of the saturated fluorescence dip from resonance by $\Delta_{shift} = \frac{1}{2}[kv_z^{ave}\{\sin(\beta) + \sin(\alpha)\} + kv_y^{ave}\sin(\phi)]$ where, v_y^{ave} is the average transverse velocity across the atomic beam in the y-direction. For symmetric divergent atomic beam along x- and y-direction (which is the case considered in Fig. 5.7), the average velocity along the x- and y-direction are all zeros i.e., $v_x^{ave} = v_y^{ave} = 0$ and the ϕ dependent frequency shift vanishes. The saturated fluorescence dip broadens and the dip height decreases as the value of ϕ is increased and vanishes for large misalignment cross the atomic beam. For asymmetric divergent atomic beam along x- and y-direction, the average velocity along the respective axes is not zero and the ϕ dependent frequency shift does not vanish. The asymmetry can arise due to the misalignment between the atomic source and the mechanical collimators used.

The result of this chapter appear in the following publication: The European Physical Journal D (Eur. Phys. J. D (2020) 74: 96; https://doi.org/10.1140/epjd/e2020-100519-0).

6

Resolving closely spaced levels for Doppler mismatched double resonance

6.1 Introduction

This chapter describes experimental techniques to resolve the closely spaced hyperfine levels of a weak transition by eliminating the residual (or partial) two-photon Doppler broadening in a wavelength mismatched double resonance spectroscopy. The partial Doppler broadening is caused by the thermal motion of the atoms in the vapor cell. The elimination of the partial Doppler broadening is based on velocity induced population oscillation (VIPO) and velocity selective saturation (VSS) effects followed by the subtraction of the broad background of the two-photon spectrum. Since the VIPO and VSS effect are the phenomena for near zero velocity group atoms, the subtraction gives rise to Doppler-free peaks and the closely spaced hyperfine levels of the $6P_{3/2}$ state in Rb are well resolved. The double resonance experiment is conducted on $5S_{1/2} \rightarrow 5P_{3/2}$ strong transition (at 780 nm) and $5S_{1/2} \rightarrow 6P_{3/2}$ weak transition (at 420 nm) at room temperature.

The chapter begins with a description of the relevant energy levels and transitions for the various configurations and the experimental setup. The subsequent sections of the chapter, describe the density matrix formalism for the various systems considered and the numerical simulation for the probe absorption profile. The experimental results on resolving the closely spaced hyperfine levels of the $6P_{3/2}$ state in Rb is presented in last sections of the chapter.

6.2 Energy level schemes and configurations

The relevant energy levels and transitions is illustrated in Fig. 6.1 for a V-type system. The propagation direction of the probe and pump lasers at 780 nm (IR) and 420 nm (blue) transitions in various configurations is shown below the energy level scheme. The probe and the counter-propagating pump lasers at 780 nm are locked to resonance on $5S_{1/2}(F = 3) \leftrightarrow 5P_{3/2}(F = 4)$ transition. The lifetime, τ_1 of the $5P_{3/2}$ state is 26.25 ns [99, 117, 118]. The absorption of the probe is monitored as the 420 nm pump laser scans across the $6P_{3/2}$ hyperfine levels on $5S_{1/2}(F = 3) \leftrightarrow 6P_{3/2}$ weak transition for a V-type system or $5S_{1/2}(F = 2) \leftrightarrow 6P_{3/2}$ weak transition for the optical pumping system. The lifetime, τ_2 of the $6P_{3/2}$ state is 120.7 ns [44].

6.2.1 Transparency for a V-type open system

6.2.1.1 V-type open system

This corresponds to the energy level configuration shown in Fig. 6.1a and has been extensively studied [57, 119]. The V-type system is open because the population from the $6P_{3/2}$ state also decays to the other ground state hyperfine level, $5S_{1/2}(F = 2)$ and can not be recycled. In the presence of the blue pump laser, c2, there is transparency of the IR probe laser due to two effects. One is coherence effect causing EIT in a

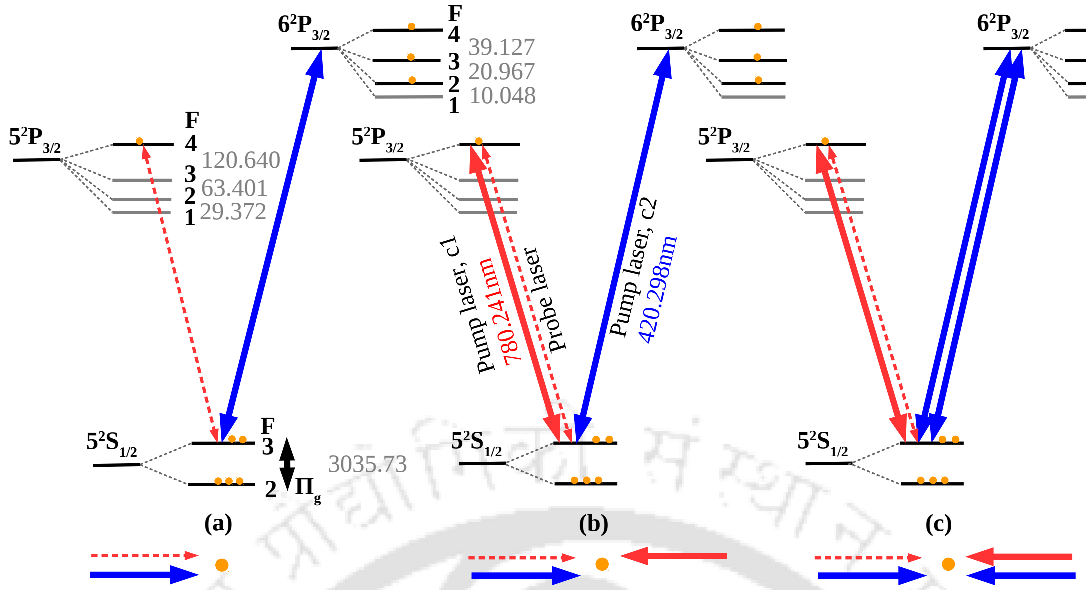

Fig. 6.1: Energy levels (^{85}Rb) with hyperfine splitting (in MHz) and the various transitions in different configurations for EIT. (a) V-type open system, (b) V-type open system with the VIPO effect at IR transition (c) V-type open system with the VIPO effect at IR transition and VSS effect at blue transition. $\Pi_g \approx 40$ kHz [11] is the ground state mixing rate.

V-type atomic system [23, 103] and the other is optical pumping effect [104, 105, 106] to the other ground hyperfine level $5S_{1/2}(F = 2)$.

Theoretically, the V-type open system is modeled by considering optical pumping of population to the other ground hyperfine level and the non-radiative mixing rate of the ground state (to allow for thermalization of the ground state hyperfine levels), Π_g [11, 108, 110]. The mixing rate, Π_g, for the hyperfine ground states is due to thermal collisions and the time of fight of atoms across the laser beam. The contribution due to time of flight is defined as $d/\tilde{v}$ where, $\tilde{v}$ is the thermal velocity of the atoms in the atomic medium and d is the diameter of the laser beam.

The transparency spectrum of the closed and open V-type system is discussed in chapter 4 subsection 4.2.1 for the case of the D1 line. The numerically simulated absorption spectrum of the IR probe laser locked to resonance on $5S_{1/2}(F = 3) \leftrightarrow$

$5P_{3/2}(F = 4)$ cycling transition vs detuning of the blue pump laser (for the case of the D2 line) is plotted in Fig. 6.2 (see the blue trace). The Lorentzian fitting to this curve gives a linewidth of 16 MHz compared to a linewidth of 11 MHz if the pump laser wavelength is 780 nm instead of 420 nm. This broadening by a factor of about 1.5 is due to the residual or partial Doppler broadening caused by wavelength mismatch between the probe and pump laser.

6.2.1.2 VIPO at IR transition for a V-type open system

The configuration of the VIPO at IR transition, corresponds to the energy scheme given in Fig. 6.1b. In this scheme a 780 nm counter-propagating pump laser is locked to resonance on $5S_{1/2}(F = 3) \leftrightarrow 5P_{3/2}(F = 4)$ transition with the probe laser. The absorption of the probe is monitored as the co-propagating 420 nm pump laser scans the $5S_{1/2}(F = 3) \leftrightarrow 6P_{3/2}$ transition.

Theoretically, the VIPO at IR transition for a V-type open system is modeled by considering the Hamiltonian H of the configuration shown in Fig. 6.1b. The Hamiltonian of the system under electric-dipole and rotating-wave approximation and in the rotating frame is obtained using Eq. 2.11 which is expressed as follows:

$$\mathrm{H} = \frac{\hbar}{2}\left\{(\Omega_{c1} + \Omega_{p} e^{i\delta_1 t})\left|1\right\rangle\left\langle 2\right| + \Omega_{c2}\left|1\right\rangle\left\langle 3\right| - \Delta_{c1}\left|2\right\rangle\left\langle 2\right| - \Delta_{c2}\left|3\right\rangle\left\langle 3\right| + \mathrm{H.c.}\right\}, \quad (6.1)$$

where, H.c. is Hermitian conjugate, $5S_{1/2}(F = 3) = |1\rangle$, $5P_{3/2}(F = 4) = |2\rangle$, $6P_{3/2}(F = 2) = |3\rangle$, $5S_{1/2}(F = 2) = |4\rangle$, $\delta_1 = (\omega_p - k_1 v) - (\omega_{c1} + k_1 v) = -2k_1 v$ is the Doppler frequency difference between 780 nm probe and pump beams (since the two laser fields are from the same laser source i.e., $\omega_p = \omega_{c1}$), $k_1 = 2\pi/\lambda_1$ is the wave-vector of the 780 nm laser and λ_1 is the wavelength, v is the velocity of the atom in the direction of the probe, $\Delta_{c1} = \omega_{c1} - (\omega_2 - \omega_1) + k_1 v$ is the detuning of the 780 nm laser, $\Delta_{c2} = \omega_{c2} - (\omega_3 - \omega_1) - k_2 v$ is the detuning of the 420 nm laser,

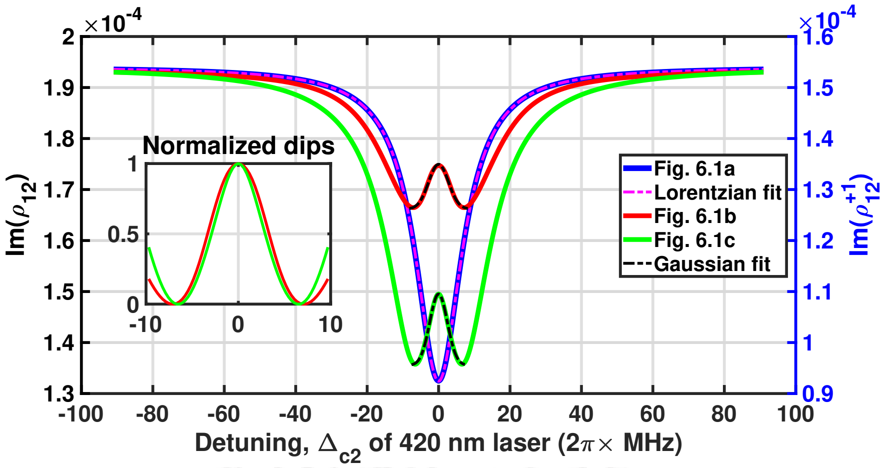

Fig. 6.2: Numerically calculated thermal averaged probe absorption vs detuning of 420 nm pump laser for V-type open system with various configurations shown in Fig. 6.1 (where $\Omega_p = \sqrt{0.0005}\Gamma_2$). The blue curve corresponds to Fig. 6.1a with $\Omega_{c2} = \sqrt{1.5}\Gamma_3$. The red curve corresponds to Fig. 6.1b with $\Omega_{c1} = \Gamma_2$ and $\Omega_{c2} = \sqrt{1.5}\Gamma_3$. The green curve corresponds to Fig. 6.1c with $\Omega_{c1} = \sqrt{0.5}\Gamma_2$, $\Omega_{c2} = \sqrt{1.5}\Gamma_3$, $\Gamma_2 = 2\pi \times 6.065$ MHz and $\Gamma_3 = 2\pi \times 1.32$ MHz. The vertical axis of the blue trace is on left and the red and green trace on the right.

$k_2 = 2\pi/\lambda_2$ is the wave-vector of the 420 nm laser and λ_2 is the wavelength. The Rabi frequency for the fields is $\Omega_{\mathrm{L}} = -\mathrm{d}_{ij}\mathrm{E}_{\mathrm{L}}/\hbar$ where, $\mathrm{d}_{ij} = \langle i|\,\hat{\mathrm{d}}\,|j\rangle$ is the dipole matrix element, $\hat{\mathrm{d}}$ is the atomic dipole operator and subscript $\mathrm{L} = \mathrm{p}, \mathrm{c1}, \mathrm{c2}$ represent the fields (i.e., p is the probe and c1 is the pump of the 780 nm laser and c2 is the pump of the 420 nm laser).

The dynamics of the atom-field interactions is given by Eq. 2.15. The substitution of Eq. 6.1 into Eq. 2.15 gives the following set of equations of motion with time-dependent coefficients:

$$
\begin{aligned}
\dot{\rho}_{12} =& \frac{i}{2}(\Omega_{\mathrm{c1}} + \Omega_{\mathrm{p}} e^{i\delta_1 t})(\rho_{11} - \rho_{22}) - \frac{i\Omega_{\mathrm{c2}}}{2}\rho_{32} - \gamma_{12}\rho_{12}, \\
\dot{\rho}_{13} =& \frac{i\Omega_{\mathrm{c2}}}{2}(\rho_{11} - \rho_{33}) - \gamma_{13}\rho_{13} - \frac{i}{2}(\Omega_{\mathrm{c1}} + \Omega_{\mathrm{p}} e^{i\delta_1 t})\rho_{23}, \\
\dot{\rho}_{14} =& -\frac{i\Omega_{\mathrm{c2}}}{2}\rho_{34} - \gamma_{14}\rho_{14} - \frac{i}{2}(\Omega_{\mathrm{c1}} + \Omega_{\mathrm{p}} e^{i\delta_1 t})\rho_{24}, \\
\dot{\rho}_{22} =& \frac{i}{2}(\Omega_{\mathrm{c1}} + \Omega_{\mathrm{p}} e^{i\delta_1 t})\rho_{21} - \frac{i}{2}(\Omega_{\mathrm{c1}}^* + \Omega_{\mathrm{p}}^* e^{-i\delta_1 t})\rho_{12} - \Gamma_2\rho_{22}, \\
\dot{\rho}_{23} =& -\frac{i}{2}(\Omega_{\mathrm{c1}}^* + \Omega_{\mathrm{p}}^* e^{-i\delta_1 t})\rho_{13} + \frac{i\Omega_{\mathrm{c2}}}{2}\rho_{21} - \gamma_{23}\rho_{23}, \\
\dot{\rho}_{24} =& -\frac{i}{2}(\Omega_{\mathrm{c1}}^* + \Omega_{\mathrm{p}}^* e^{-i\delta_1 t})\rho_{14} - \gamma_{24}\rho_{24}, \\
\dot{\rho}_{33} =& -\frac{i\Omega_{\mathrm{c2}}^*}{2}\rho_{13} + \frac{i\Omega_{\mathrm{c2}}}{2}\rho_{31} - \Gamma_3\rho_{33}, \\
\dot{\rho}_{34} =& -\frac{i\Omega_{\mathrm{c2}}^*}{2}\rho_{14} - \gamma_{34}\rho_{34}, \\
\dot{\rho}_{44} =& \Gamma_{34}\rho_{33} + \Pi_g(\rho_{11} - \rho_{44}),
\end{aligned}
\tag{6.2}
$$

where, $\gamma_{12} = i\Delta_{\mathrm{c1}} + \gamma_{12}^{dec}$, $\gamma_{13} = i\Delta_{\mathrm{c2}} + \gamma_{13}^{dec}$, $\gamma_{14} = \gamma_{14}^{dec}$, $\gamma_{23} = i(\Delta_{\mathrm{c2}} - \Delta_{\mathrm{c1}}) + \gamma_{23}^{dec}$, $\gamma_{24} = -i\Delta_{\mathrm{c1}} + \gamma_{24}^{dec}$, $\gamma_{34} = -i\Delta_{\mathrm{c2}} + \gamma_{34}^{dec}$, $\Gamma_1 = \Gamma_4 = \Pi_g$, $\gamma_{34} = i\Delta_{\mathrm{c2}} + \gamma_{34}^{dec}$, $\Gamma_3 = \Gamma_{31} + \Gamma_{34}$, and $\gamma_{ij}^{dec} = \frac{1}{2}(\Gamma_i + \Gamma_j)$, Γ_{31} and Γ_{34} are the decay rates of level 3 to level 1 and level 4 respectively. The remaining density matrix equations are obtained using the population conservation law $\sum_{j=1}^{4} \rho_{jj} = 1$ and the complex conjugate $\dot{\rho}_{ji} = \dot{\rho}_{ij}^*$.

The temporal behavior of the coefficients in Eq. 6.2 is velocity dependent due to the Doppler effect. The time evolution of the density matrix will therefore oscillate at the harmonics of the beat frequency $\delta_1 = -2k_1 v$. The oscillation is caused by interference (or beating) of the two fields addressing the same transition $5\mathrm{S}_{1/2}(\mathrm{F} = 3) \leftrightarrow 5\mathrm{P}_{3/2}(\mathrm{F} = 4)$ in Fig. 6.1a. The beating of the two fields causes a temporal modulation of population difference between the lower level $5\mathrm{S}_{1/2}(\mathrm{F} = 3)$ and upper level $5\mathrm{P}_{3/2}(\mathrm{F} = 4)$ [64, 65, 66, 67, 68, 69, 70] a phenomenon which is known as velocity induced population oscillations (VIPO). The VIPO effect occurs only for a narrow range of beat frequencies because of the inherent population inertia i.e., the slow response of electric dipoles to incident fields. The range of beat frequencies is determined by the inverse of population relaxation times of the upper levels 5P$_{3/2}$ and 6P$_{3/2}$ [27, 70, 71]. The contribution of the population oscillation is significant when $2k_1v \leq 1/\tau_2$ and $\tau_1 \ll \tau_2$.

The harmonically oscillating density matrix elements at beat frequency can be written in the Floquet expansion [72, 120, 121] given in Eq. 5.5 by replacing the beat frequency δ with δ_1. The imaginary part of the zeroth harmonic, $\rho_{12}^{(0)}$ corresponds to the IR pump absorption, while the imaginary part of the first harmonic, $\rho_{12}^{(+1)}$ is proportional to IR probe absorption in first order and all the others are for wave-mixing [25]. This explanation is considered in detail in appendix E for a two-level system driven by pump and probe laser fields. In the steady state condition ($\dot{\rho}_{ij}^{(n)} = 0$ for all n, i and j), the absorption of the probe laser ($\rho_{12}^{(+1)}$) is obtained by substituting the truncated series of the Floquet expansion given in Eq. 5.5 up to first-order into Eq. 6.2. The coefficients of the same power in $n\delta_1$ are then compared (for details on the Floquet expansion see appendix C section C.1). The $\rho_{12}^{(+1)}$ element of the density matrix is expressed as follows:

$$\rho_{12}^{(+1)} = \underbrace{\frac{i\Omega_p}{2(\gamma_{12}+i\delta_1)}(\rho_{11}^{(0)}-\rho_{22}^{(0)})}_{\text{I}} + \underbrace{\frac{i\Omega_{c1}}{2(\gamma_{12}+i\delta_1)}(\rho_{11}^{(+1)}-\rho_{22}^{(+1)})}_{\text{II}} - \underbrace{\frac{i\Omega_{c2}}{2(\gamma_{12}+i\delta_1)}\rho_{32}^{(+1)}}_{\text{III}}, \tag{6.3}$$

where, $\gamma_{12} = i\Delta_p + \gamma_{12}^{dec}$, $\Delta_p = \Delta_{c1} = 0$, $\gamma_{ij}^{dec} = \frac{1}{2}(\Gamma_i + \Gamma_j)$ and Γ_i is the decay rate of the i^{th} level. The quantity $(\rho_{11}^{(0)} - \rho_{22}^{(0)})$ in term I is the population inversion created by the pump lasers at IR and blue transition. The quantity $(\rho_{11}^{(+1)} - \rho_{22}^{(+1)})$ in term II is the population oscillation difference and its contribution is significant for the velocity group atoms in the range of $|v| \sim \Gamma_2/k_1$ and forms a dip inside the transparency window. The density matrix element $\rho_{32}^{(+1)}$ in term III is the coherence oscillation which further modifies the lineshape of the dip inside the transparency window. The role of individual terms for the probe absorption is shown in Fig. 6.3.

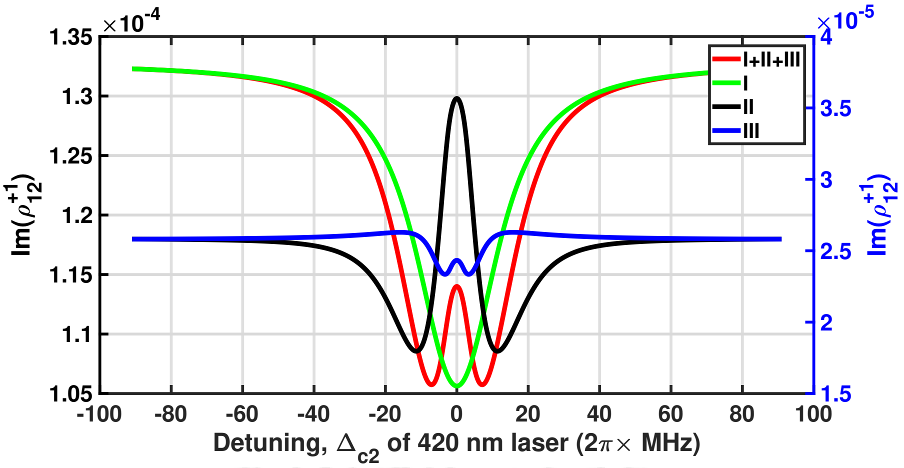

Fig. 6.3: Graphical representation of the individual terms I, II and III given in Eq. 6.3. $\Omega_{c1} = \Gamma_2$, $\Omega_{c2} = \sqrt{1.5}\Gamma_3$, $\Gamma_2 = 2\pi \times 6.065$ MHz, $\Gamma_3 = 2\pi \times 1.32$ MHz and $\Pi_g = 2\pi \times 40$ kHz. The vertical axis of the red and green trace is on left and the blue and black trace on the right

The absorption of the probe laser is obtained by thermal averaging of Eq. 6.3 at room temperature as follows, $\frac{1}{\sqrt{2\pi}\tilde{v}} \int \rho_{12}^{(+1)} e^{-(\frac{v}{2\tilde{v}})^2} dv$, where, $\tilde{v} = \sqrt{k_B T/m}$, m (= 85 a.m.u) is the atomic mass and T (= 300 K) is the temperature. The lineshape of the probe absorption after thermal averaging is shown in Fig. 6.2 (see the red trace). The linewidth of the dip inside the transparency window is around 7 MHz which is less than the linewidth for a V system if the pump laser wavelength is 780 nm instead of 420 nm. The linewidth of the dip is determined by fitting with a Gaussian line-profile (which fits better than a Lorentzian line-profile). The FWHM of a Gaussian fit (i.e., $Ae^{-(x-x_0)^2/(2\sigma^2)}$), is $2\sqrt{2\ln 2}\sigma$ where A, x_0 and σ are the fitting parameters and x is the frequency detuning.

6.2.1.3 VIPO at IR and VSS at blue transition for a V-type system

The energy scheme for this configuration is given in Fig. 6.1c where the probe and IR pump are similarly locked to resonance on $5S_{1/2}(F = 3) \leftrightarrow 5P_{3/2}(F = 4)$ cycling transition. The blue pump scans across the hyperfine levels of the $6P_{3/2}$ state on

$5S_{1/2}(F = 3) \leftrightarrow 6P_{3/2}$ weak transition and is retro-reflected by mirror M into the Rb vapor cell to counter-propagate with the incident blue laser beam. The VIPO on $5S_{1/2}(F = 3) \leftrightarrow 5P_{3/2}(F = 4)$ transition will induce a dip on the transparency peak as previously explained in section 6.2.1.2. This dip is further enhanced by the VSS effect of the two counter-propagating blue pump laser fields.

The VSS effect can be understood in the following simple way. We consider population dynamics between the two states, $|1\rangle$ ($5S_{1/2}$, F=2) and $|3\rangle$ ($6P_{3/2}$) due to two counter-propagating blue pump laser fields only in the absence of the IR laser. For simplicity, consider three velocity group of atoms, $+v$, 0 and $-v$. For detuned case of the blue pump laser, (Δ_{c2}) both the non-zero velocity group of atom $\pm v = \Delta_{c2}/k_2$ will be resonant with either of the two counter-propagating blue pump laser fields and hence the number of atoms in the excited state will be doubled. For zero detuning case, the near-zero velocity ($< \Gamma_3/k_2$) group of atom will be resonant with both the blue pump laser fields and the intensity seen by this group of atoms will be doubled. However, the excited state population will be less than double due to saturation effect, thus inducing a dip in the absorption spectrum of the probe beam with the scan of the blue pump laser. The linewidth of this dip is in the range of Γ_3. This qualitative picture is also presented in [26]. Mathematically, the population transfer due to blue pump lasers is expressed as follows [27],

$$\rho_{33}^{(0)} = \frac{1}{2}\left\{\frac{\frac{\Omega_{c2}^2/2}{\frac{\Gamma_3^2}{4}+(\Delta_{c2}-k_2v)^2} + \frac{\Omega_{c2}^2/2}{\frac{\Gamma_3^2}{4}+(\Delta_{c2}+k_2v)^2}}{1 + \frac{\Omega_{c2}^2/2}{\frac{\Gamma_3^2}{4}+(\Delta_{c2}-k_2v)^2} + \frac{\Omega_{c2}^2/2}{\frac{\Gamma_3^2}{4}+(\Delta_{c2}+k_2v)^2}}\right\}. \tag{6.4}$$

For a given velocity v there is also a beating of the two counter-propagating blue pump lasers in the atomic frame with the beat frequency ($\delta_2 = -2k_2v$). Therefore, the Hamiltonian H of a V-type system given in Fig. 6.1c under electric-dipole and rotating-wave approximation and in the rotating frame (which is obtained using Eq.

2.11) will have two different time dependence:

$$\mathrm{H} =\frac{\hbar}{2}\{(\Omega_{\mathrm{c1}}+\Omega_{\mathrm{p}}e^{i\delta_1 t})\left|1\right\rangle\left\langle 2\right| + (\Omega_{\mathrm{c2}}+\Omega_{\mathrm{c2}}e^{i\delta_2 t})\left|1\right\rangle\left\langle 3\right| - \Delta_{\mathrm{c1}}\left|2\right\rangle\left\langle 2\right| - \Delta_{\mathrm{c2}}\left|3\right\rangle\left\langle 3\right| + \mathrm{H.c.}\}. \tag{6.5}$$

The dynamics of the atom-field interactions is obtained from Eq. 2.15 and 6.5 which gives the following set of equations of motion with time-dependent coefficients:

$$\begin{aligned}
\dot{\rho}_{12} =& \frac{i}{2}(\Omega_{\mathrm{c1}}+\Omega_{\mathrm{p}}e^{i\delta_1 t})(\rho_{11}-\rho_{22}) - \gamma_{12}\rho_{12} - \frac{i\Omega_{\mathrm{c2}}}{2}(1+e^{i\delta_2 t})\rho_{32}, \qquad (6.6)\\
\dot{\rho}_{13} =& \frac{i\Omega_{\mathrm{c2}}}{2}(1+e^{i\delta_2 t})(\rho_{11}-\rho_{33}) - \gamma_{13}\rho_{13} - \frac{i}{2}(\Omega_{\mathrm{c1}}+\Omega_{\mathrm{p}}e^{i\delta_1 t})\rho_{23},\\
\dot{\rho}_{14} =& -\frac{i\Omega_{\mathrm{c2}}}{2}(1+e^{i\delta_2 t})\rho_{34} - \gamma_{14}\rho_{14} - \frac{i}{2}(\Omega_{\mathrm{c1}}+\Omega_{\mathrm{p}}e^{i\delta_1 t})\rho_{24},\\
\dot{\rho}_{22} =& \frac{i}{2}(\Omega_{\mathrm{c1}}+\Omega_{\mathrm{p}}e^{i\delta_1 t})\rho_{21} - \frac{i}{2}(\Omega^*_{\mathrm{c1}}+\Omega^*_{\mathrm{p}}e^{-i\delta_1 t})\rho_{12} - \Gamma_2\rho_{22},\\
\dot{\rho}_{23} =& -\frac{i}{2}(\Omega^*_{\mathrm{c1}}+\Omega^*_{\mathrm{p}}e^{-i\delta_1 t})\rho_{13} + \frac{i\Omega_{\mathrm{c2}}}{2}(1+e^{i\delta_2 t})\rho_{21} - \gamma_{23}\rho_{23},\\
\dot{\rho}_{24} =& -\frac{i}{2}(\Omega^*_{\mathrm{c1}}+\Omega^*_{\mathrm{p}}e^{-i\delta_1 t})\rho_{14} - \gamma_{24}\rho_{24},\\
\dot{\rho}_{33} =& -\frac{i\Omega^*_{\mathrm{c2}}}{2}(1+e^{-i\delta_2 t})\rho_{13} + \frac{i\Omega_{\mathrm{c2}}}{2}(1+e^{i\delta_2 t})\rho_{31} - \Gamma_3\rho_{33},\\
\dot{\rho}_{34} =& -\frac{i\Omega^*_{\mathrm{c2}}}{2}(1+e^{-i\delta_2 t})\rho_{14} - \gamma_{34}\rho_{34},\\
\dot{\rho}_{44} =& \Gamma_{34}\rho_{33} + \Pi_g(\rho_{11}-\rho_{44}).
\end{aligned}$$

The coefficients of the harmonically oscillating density matrix elements have two different time dependence, which is also the case for the Hamiltonian in Eq. 6.5. The Floquet expansion for the density matrix elements in such a case is modified and written as follows:

$$\rho_{ij}(t) = \sum_{m=-\infty}^{\infty}\Big(\sum_{n=-\infty}^{\infty}\rho_{ij}^{(n,m)}(t)e^{i(n\delta_1+m\delta_2)t}\Big), \tag{6.7}$$

where, n is the n^{th} harmonic component due the beating of the IR laser beams and m

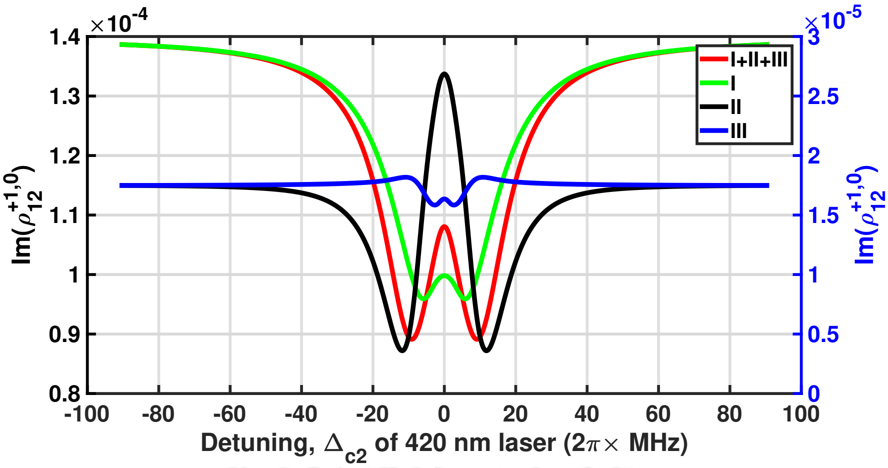

Fig. 6.4: Graphical representation of the individual terms I, II and III given in Eq. 6.8. $\Omega_{c1} = \Gamma_2$, $\Omega_{c2} = \sqrt{1.5}\Gamma_3$, $\Gamma_2 = 2\pi \times 6.065$ MHz, $\Gamma_3 = 2\pi \times 1.32$ MHz and $\Pi_g = 2\pi \times 40$ kHz. The vertical axis of the red and green trace is on left and the blue and black trace on the right

is the m^{th} harmonic component due the beating of the blue pump laser beams. The imaginary part of $\rho_{12}^{(0,0)}$ corresponds to the IR pump absorption, while the imaginary part of $\rho_{12}^{(+1,0)}$ is proportional to IR probe absorption and all the others are for wave-mixing. In the steady state condition (i.e., $\dot{\rho}_{ij}^{(n,m)} = 0$ for all n, m, i and j), $\rho_{12}^{(+1,0)}$ is obtained by substituting the truncated series of the Floquet expansion given in Eq. 6.7 up to first-order into Eq. 6.6. The coefficients of the same power in $(n\delta_1, m\delta_2)$ are similarly compared (for details on the Floquet expansion see appendix C section C.2). The $\rho_{12}^{(+1,0)}$ element of the density matrix is expressed as follows,

$$\rho_{12}^{(+1,0)} = \underbrace{\frac{i\Omega_p(\rho_{11}^{(0,0)} - \rho_{22}^{(0,0)})}{2(\gamma_{12} + i\delta_1)}}_{\text{I}} + \underbrace{\frac{i\Omega_{c1}(\rho_{11}^{(+1,0)} - \rho_{22}^{(+1,0)})}{2(\gamma_{12} + i\delta_1)}}_{\text{II}} - \underbrace{\frac{i\Omega_{c2}(\rho_{32}^{(+1,0)} + \rho_{32}^{(+1,-1)})}{2(\gamma_{12} + i\delta_1)}}_{\text{III}}. \quad (6.8)$$

In Eq. 6.8, the quantity $(\rho_{11}^{(0,0)} - \rho_{22}^{(0,0)})$ in term I is the population inversion induced by the IR pump and the saturation of the counter-propagating blue pumps and $(\rho_{11}^{(+1,0)} - \rho_{22}^{(+1,0)})$ in term II is the population oscillation induced by the beating of the IR probe and pump laser beams and the saturation of the counter-propagating blue pumps. The density matrix elements, $\rho_{32}^{(+1,0)}$ and $\rho_{32}^{(+1,-1)}$ in term III, are the oscillating coherence terms due to the beating of the fields on IR and blue transitions. The contribution of individual terms (I, II and III) to probe absorption is shown in Fig. 6.4. The thermal averaged probe absorption, $\frac{1}{\sqrt{2\pi}\tilde{v}} \int \rho_{12}^{(+1,0)} e^{-(\frac{v}{2\tilde{v}})^2} \mathrm{d}v$ is calculated numerically and is plotted in Fig. 6.2 (see the green trace). The linewidth of the induced dip is around 6 MHz.

6.2.2 Enhanced absorption for optical pumping system

6.2.2.1 Optical pumping system

The energy level scheme and configuration of the optical pumping system is given in Fig. 6.5. In this scheme, the 780 nm probe laser is locked to resonance on $5S_{1/2}(F = 3) \leftrightarrow 5P_{3/2}(F = 4)$ transition. The absorption of the probe is monitored as the co-propagating 420 nm pump laser scans around the $6P_{3/2}$ hyperfine levels on $5S_{1/2}(F = 2) \rightarrow 6P_{3/2}$ transition instead of $5S_{1/2}(F = 3) \rightarrow 6P_{3/2}$ transition. The absorption of the probe is increased by optical pumping of population to the upper ground hyperfine level $5S_{1/2}(F = 3)$ [104, 105, 106] via $5S_{1/2}(F = 2) \rightarrow 6P_{3/2}(F = 1, 2, 3)$ excitation and various decay channels (i.e., direct, $6P_{3/2}(F = 2, 3) \rightarrow 5S_{1/2}(F = 3)$ and indirect decay channels [122] such as $6P_{3/2}(F = 1) \rightarrow 6S_{1/2} \rightarrow 5P_{3/2} \rightarrow 5S_{1/2}(F = 3)$). Therefore, optical pumping [108, 110] gives rise to enhanced absorption (EA) Doppler-free peaks of the $6P_{3/2}$ hyperfine levels. The numerically simulated absorption spectrum considering only one hyperfine level is plotted in Fig. 6.6 (see the blue trace) and is well discussed in chapter 4 subsection 4.2.2 for the D1 line. The Lorentzian fitting to this curve gives a linewidth of 17 MHz, while it is 11 MHz if we consider the pump laser wavelength to be 780 nm instead of 420 nm. This broadening by 1.5 times is again due to residual or partial Doppler broadening caused by wavelength mismatch between the probe and the pump laser.

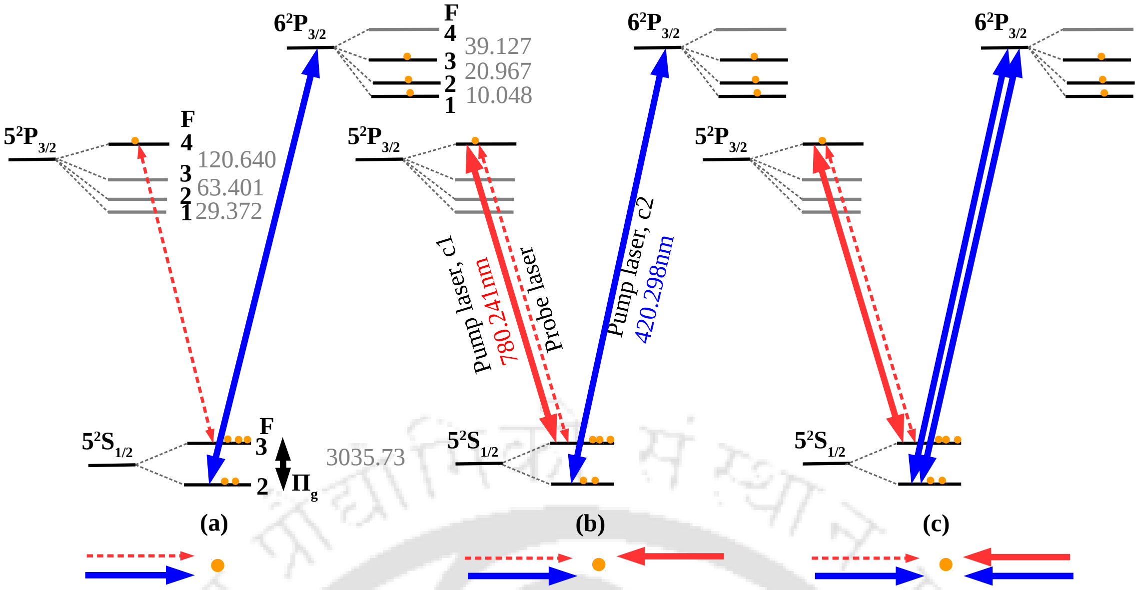

Fig. 6.5: Energy levels (^{85}Rb) with hyperfine splitting (in MHz) and the various transitions in different configurations for EA scheme. (a) optical pumping system, (b) optical pumping system with the VIPO effect at IR transition (c) optical pumping system with the VIPO effect at IR transition and VSS effect at blue transition. $\Pi_g \approx$ 40 kHz [11] is the ground state mixing rate.

6.2.2.2 VIPO at IR transition for optical pumping system

This corresponds to the energy level and the configuration given in Fig. 6.5b. It is theoretically modeled by considering the Hamiltonian H of a four level optical pumping system in Fig. 6.5b. The Hamiltonian of the system under electric-dipole and rotating-wave approximation and in rotating frame is obtained using Eq. 2.11 which is expressed as follows:

$$\mathrm{H} = \frac{\hbar}{2}\{(\Omega_{\mathrm{c1}} + \Omega_{\mathrm{p}} e^{i\delta_1 t})\,|1\rangle\langle 2| + \Omega_{\mathrm{c2}}\,|4\rangle\langle 3| - \Delta_{\mathrm{c1}}\,|2\rangle\langle 2| - \Delta_{\mathrm{c2}}\,|3\rangle\langle 3| + \mathrm{H.c.}\}, \qquad (6.9)$$

where, $5S_{1/2}(F = 3) = |1\rangle$, $5P_{3/2}(F = 4) = |2\rangle$, $6P_{3/2}(F = 1) = |3\rangle$ and $5S_{1/2}(F = 2) = |4\rangle$. The dynamics of the atom-field interactions is obtained from Eq. 2.15 and 6.9 which gives the following set of equations of motion with time-dependent coefficients:

$$\begin{aligned}
\dot{\rho}_{12} =& \frac{i}{2}(\Omega_{c1} + \Omega_p e^{i\delta_1 t})(\rho_{11} - \rho_{22}) - \gamma_{12}\rho_{12}, \\
\dot{\rho}_{13} =& -\frac{i}{2}(\Omega_{c1} + \Omega_p e^{i\delta_1 t})\rho_{23} + \frac{i\Omega_{c2}^*}{2}\rho_{14} - \gamma_{13}\rho_{13}, \\
\dot{\rho}_{14} =& -\frac{i}{2}(\Omega_{c1} + \Omega_p e^{i\delta_1 t})\rho_{24} + \frac{i\Omega_{c2}}{2}\rho_{13} - \gamma_{14}\rho_{14}, \\
\dot{\rho}_{22} =& -\frac{i}{2}(\Omega_{c1}^* + \Omega_p^* e^{-i\delta_1 t})\rho_{12} + \frac{i}{2}(\Omega_{c1} + \Omega_p e^{i\delta_1 t})\rho_{21} - \Gamma_2\rho_{22}, \\
\dot{\rho}_{23} =& -\frac{i}{2}(\Omega_{c1}^* + \Omega_p^* e^{-i\delta_1 t})\rho_{13} - \gamma_{23}\rho_{23} + \frac{i\Omega_{c2}^*}{2}\rho_{24}, \\
\dot{\rho}_{24} =& -\frac{i}{2}(\Omega_{c1}^* + \Omega_p^* e^{-i\delta_1 t})\rho_{14} - \gamma_{24}\rho_{24} + \frac{i\Omega_{c2}}{2}\rho_{23}, \\
\dot{\rho}_{33} =& -\frac{i\Omega_{c2}}{2}\rho_{43} + \frac{i\Omega_{c2}^*}{2}\rho_{34} - \Gamma_3\rho_{33}, \\
\dot{\rho}_{34} =& -\frac{i\Omega_{c2}}{2}(\rho_{33} - \rho_{44}) - \gamma_{34}\rho_{34}, \\
\dot{\rho}_{44} =& -\frac{i\Omega_{c2}^*}{2}\rho_{34} + \frac{i\Omega_{c2}}{2}\rho_{43} + \Gamma_{34}\rho_{33} + \Pi_g(\rho_{11} - \rho_{44}),
\end{aligned} \tag{6.10}$$

where, $\gamma_{12} = i\Delta_{c1} + \gamma_{12}^{dec}$, $\gamma_{13} = \gamma_{13}^{dec}$, $\gamma_{14} = i\Delta_{c2} + \gamma_{14}^{dec}$, $\gamma_{23} = -i\Delta_{c1} + \gamma_{23}^{dec}$, $\gamma_{24} = i(\Delta_{c2} - \Delta_{c1}) + \gamma_{24}^{dec}$, $\gamma_{34} = i\Delta_{c2} + \gamma_{34}^{dec}$, $\Gamma_3 = \Gamma_{31} + \Gamma_{34}$, and $\gamma_{ij}^{dec} = \frac{1}{2}(\Gamma_i + \Gamma_j)$.

The equations of motion (Eq. 6.10) are solved in steady state after the Floquet expansion given in Eq. 5.5 and the imaginary part of the density matrix element $\rho_{12}^{(+1)}$ is proportional to the absorption of the probe and is expressed as follows,

$$\rho_{12}^{(+1)} = \underbrace{\frac{i\Omega_p}{2(\gamma_{12} + i\delta_1)}(\rho_{11}^{(0)} - \rho_{22}^{(0)})}_{\text{I}} + \underbrace{\frac{i\Omega_{c1}}{2(\gamma_{12} + i\delta_1)}(\rho_{11}^{(+1)} - \rho_{22}^{(+1)})}_{\text{II}}. \tag{6.11}$$

Equation 6.11 is similar to Eq. 6.3 except the coherence term. The first term, I in Eq. 6.11 is due to population inversion created by the pump laser at IR and blue transition and gives only the EA line-shape. The second term, II in Eq. 6.11 is due to VIPO at IR transition and gives a dip inside the EA spectrum as shown Fig. 6.6 (see the red trace). The linewidth of the dip is 9 MHz using Gaussian line profile fit. The contribution of each of the terms I and II is given in Fig. 6.7 and the solutions

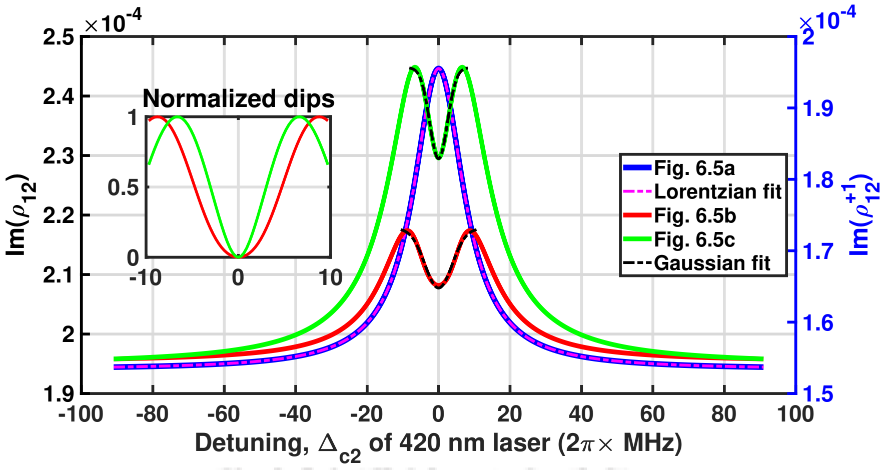

Fig. 6.6: Numerically calculated thermal averaged probe absorption vs detuning of 420 nm pump laser for optical system with various configurations shown in Fig. 6.5 (where $\Omega_p = \sqrt{0.0005}\Gamma_2$). The blue curve corresponds to Fig. 6.5a with $\Omega_{c2} = \sqrt{1.5}\Gamma_3$. The red curve corresponds to Fig. 6.5b with $\Omega_{c1} = \Gamma_2$ and $\Omega_{c2} = \sqrt{1.5}\Gamma_3$. The green curve corresponds to Fig. 6.5c with $\Omega_{c1} = \sqrt{0.5}\Gamma_2$, $\Omega_{c2} = \sqrt{1.5}\Gamma_3$, $\Gamma_2 = 2\pi \times 6.065$ MHz and $\Gamma_3 = 2\pi \times 1.32$ MHz. The vertical axis of the blue trace is on left and the red and green trace on the right.

of the density matrix elements $\rho_{11}^{(0)}$, $\rho_{22}^{(0)}$, $\rho_{11}^{(+1)}$ and $\rho_{22}^{(+1)}$ are given in appendix D.

6.2.2.3 VIPO at IR and VSS at blue transition for optical pumping system

The energy levels and configuration of of the system is given in Fig. 6.5c. The probe and the IR pump lasers are similarly locked to resonance on $5S_{1/2}(F = 3) \leftrightarrow 5P_{3/2}(F = 4)$ cycling transition. The blue pump laser is scanning across the hyperfine levels of $6P_{3/2}$ on the weak transition, $5S_{1/2}(F = 2) \leftrightarrow 6P_{3/2}$ and is retro-reflected to generate the two counter-propagating beams inside the Rb vapor cell. The Hamiltonian H for this system (see Fig. 6.5c) under electric-dipole and rotating-wave approximation

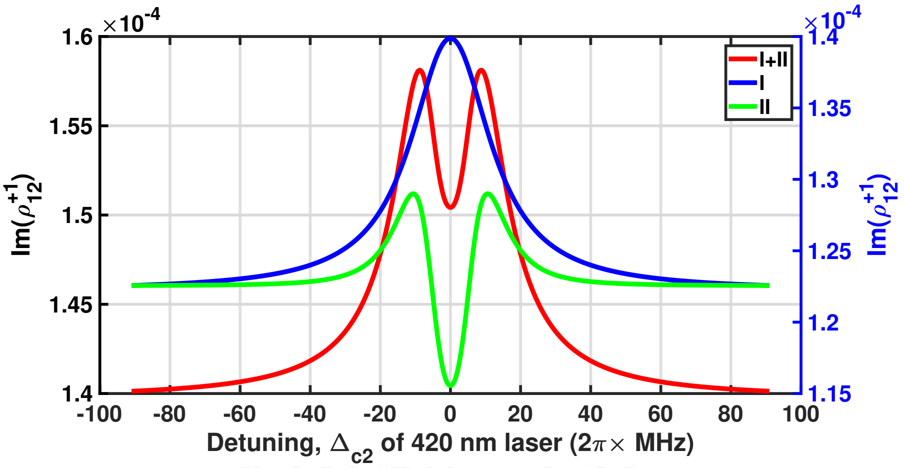

Fig. 6.7: The graphical representation of the individual terms I and II given in Eq. 6.11. $\Omega_{c1} = \Gamma_2$, $\Omega_{c2} = \sqrt{1.5}\Gamma_3$, $\Gamma_2 = 2\pi \times 6.065$ MHz, $\Gamma_3 = 2\pi \times 1.32$ MHz. The vertical axis of the red trace is on left and the blue and green trace on the right.

and in the rotating frame is given as follows,

$$\begin{aligned} \mathrm{H} =& \frac{\hbar}{2}\Big\{(\Omega_{\mathrm{c1}} + \Omega_{\mathrm{p}}e^{i\delta_1 t})\,|1\rangle\,\langle 2| + (\Omega_{\mathrm{c2}} + \Omega_{\mathrm{c2}}e^{i\delta_2 t})\,|4\rangle\,\langle 3| \\ & - \Delta_{\mathrm{c1}}\,|2\rangle\,\langle 2| - \Delta_{\mathrm{c2}}\,|3\rangle\,\langle 3| + \mathrm{H.c.}\Big\}. \end{aligned} \tag{6.12}$$

The dynamics of the atom-field interactions is similarly obtained from Eq. 2.15 and 6.12 which gives the following set of equations of motion with time-dependent coefficients:

$$\begin{aligned}
\dot{\rho}_{12} =& \frac{i}{2}(\Omega_{c1}+\Omega_p e^{i\delta_1 t})(\rho_{11}-\rho_{22})-\gamma_{12}^{dec}\rho_{12}, \\
\dot{\rho}_{13} =& -\frac{i}{2}(\Omega_{c1}+\Omega_p e^{i\delta_1 t})\rho_{23}+\frac{i}{2}(\Omega_{c2}^{*}+\Omega_{c2}^{*}e^{-i\delta_2 t})\rho_{14}-\gamma_{13}\rho_{13}, \\
\dot{\rho}_{14} =& -\frac{i}{2}(\Omega_{c1}+\Omega_p e^{i\delta_1 t})\rho_{24}+\frac{i}{2}(\Omega_{c2}+\Omega_{c2}e^{i\delta_2 t})\rho_{13}-\gamma_{14}\rho_{14}, \\
\dot{\rho}_{22} =& -\frac{i}{2}(\Omega_{c1}^{*}+\Omega_p^{*}e^{-i\delta_1 t})\rho_{12}+\frac{i}{2}(\Omega_{c1}+\Omega_p e^{i\delta_1 t})\rho_{21}-\Gamma_2\rho_{22}, \\
\dot{\rho}_{23} =& -\frac{i}{2}(\Omega_{c1}^{*}+\Omega_p^{*}e^{-i\delta_1 t})\rho_{13}+\frac{i}{2}(\Omega_{c2}^{*}+\Omega_{c2}^{*}e^{-i\delta_2 t})\rho_{24}-\gamma_{23}\rho_{23}, \\
\dot{\rho}_{24} =& -\frac{i}{2}(\Omega_{c1}^{*}+\Omega_p^{*}e^{-i\delta_1 t})\rho_{14}+\frac{i}{2}(\Omega_{c2}+\Omega_{c2}e^{i\delta_2 t})\rho_{23}-\gamma_{24}\rho_{24}, \\
\dot{\rho}_{33} =& -\frac{i}{2}(\Omega_{c2}+\Omega_{c2}e^{i\delta_2 t})\rho_{43}+\frac{i}{2}(\Omega_{c2}^{*}+\Omega_{c2}^{*}e^{-i\delta_2 t})\rho_{34}-\Gamma_3\rho_{33}, \\
\dot{\rho}_{34} =& -\frac{i}{2}(\Omega_{c2}+\Omega_{c2}e^{i\delta_2 t})(\rho_{33}-\rho_{44})-\gamma_{34}\rho_{34}, \\
\dot{\rho}_{44} =& -\frac{i}{2}(\Omega_{c2}^{*}+\Omega_{c2}^{*}e^{-i\delta_2 t})\rho_{34}+\frac{i}{2}(\Omega_{c2}+\Omega_{c2}e^{i\delta_2 t})\rho_{43}+\Gamma_{34}\rho_{33}+\Pi_g(\rho_{11}-\rho_{44}).
\end{aligned} \tag{6.13}$$

The probe absorption is obtained in the steady state condition using the equations of motion given in Eq. 6.13 and the Floquet expansion given in Eq. 6.7. The imaginary part of the density matrix element $\rho_{12}^{(+1,0)}$ in the Floquet expansion is proportional to probe absorption and is expressed as follows,

$$\rho_{12}^{(+1,0)} = \underbrace{\frac{i\Omega_p(\rho_{11}^{(0,0)}-\rho_{22}^{(0,0)})}{2(\gamma_{12}+i\delta_1)}}_{\text{I}} + \underbrace{\frac{i\Omega_{c1}(\rho_{11}^{(+1,0)}-\rho_{22}^{(+1,0)})}{2(\gamma_{12}+i\delta_1)}}_{\text{II}}. \tag{6.14}$$

In Eq. 6.14, the quantity $(\rho_{11}^{(0,0)}-\rho_{22}^{(0,0)})$ in term I is the population inversion induced by the 780 nm and 420 nm pump lasers. The quantity $(\rho_{11}^{(+1,0)}-\rho_{22}^{(+1,0)})$ in term II is the population oscillation induced by the beating of the 780 nm laser beams and saturation effect induced by the counter-propagating 420 nm pump beams. The contribution of each of the terms I and II is given in Fig. 6.8. The thermal averaged absorption in this configuration is shown in Fig. 6.6 (see the green trace). The linewidth of the induced dip on the EA peak is about 6 MHz.

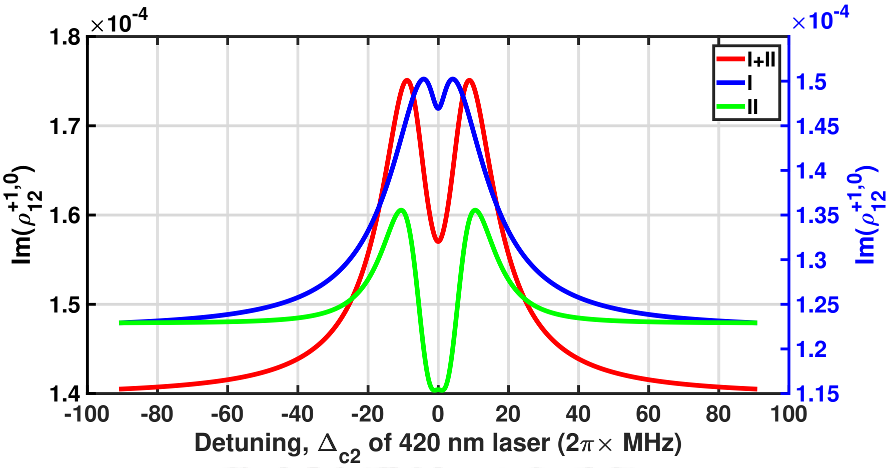

Fig. 6.8: The graphical representation of the individual terms I and II given in Eq. 6.14. $\Omega_{c1} = \Gamma_2$, $\Omega_{c2} = \sqrt{1.5}\Gamma_3$, $\Gamma_2 = 2\pi \times 6.065$ MHz, $\Gamma_3 = 2\pi \times 1.32$ MHz. The vertical axis of the red trace is on left and the blue and green trace on the right.

6.3 Experimental results

6.3.1 Set-up description

The 780 nm laser beam is generated from the thorlab laser diode L785H1 which is a home-assembled extended cavity diode laser (ECDL) with typical linewidth of 500 kHz. This laser is locked to resonance on $5S_{1/2}(F = 3) \leftrightarrow 5P_{3/2}(F = 4)$ transition shown in Figs. 6.1 and 6.5 using saturated absorption spectroscopy (SAS) set-up. The error signal for locking the laser is generated by frequency modulation using the current of ECDL at 50 kHz. The recorded experimental spectra is frequency scaled using the resolved peaks location of the green trace (in each of the configurations) for the hyperfine splitting values given in reference [21].

The 420 nm laser beam is generated from a commercially available ECDL from TOPTICA of model no. DL PRO HP with a typical linewidth of $<$ 200 kHz and output power of 70 mW. A portion of the beam is fed to Fabry-Pérot interferometer for monitoring the single-mode operation of the blue laser. The beam diameter of the

780 nm probe and pump beams is 2×3 mm and that of 420 nm pump beams is 3×4 mm. The power of the probe beam used in the experiment is 42 μW (or peak intensity, $I = 1.8$ mW/cm^2).

The detailed experimental set up is shown in Fig. 6.9. In order to extract the narrow linewidth, the probe laser beam is divided into two beams with same polarization and power and propagating in the Rb cell with a spatial separation of about 1 cm. The blue beam is also divided into two beams with the same polarization as the IR beams and co-propagates with the two probes as shown in the experimental set-up of Fig. 6.9. The IR pump beam which counter-propagates with one of the probe beam, has the same polarization as the probe beam since same polarization is key for the interference (or beating) of the two fields. The beating of the fields requires the polarization of the two fields to be identical and this aspect has been verified experimentally by rotating the polarization of one of the fields. When the polarization of the two fields are orthogonal, the VIPO dip disappear. There is a retro-mirror for reflecting the blue beam (which is overlapping with IR pump beam) back into the Rb cell to counter-propagate with the incident blue beam, when shutter 2 is open. It is very important to keep the angle between the beams as small as possible (i.e., near zero angles with the help of dichroic mirrors, DM) and the use a magnetic shield to minimize broadening of the spectrum.

There are three shutters which are used to generate various conditions and configurations in the experiment. The configuration represented by Fig. 6.1a or 6.5a is generated with all the shutters closed. The configuration represented by Fig. 6.1b or 6.5b is generated with shutter 1 open and shutter 2 closed. The configuration represented by Fig. 6.1c or 6.5c is generated with shutter 1 and shutter 2 open. Opening the shutter 3 removes the broad background of the transparency and EA peaks. The broad background is removed by the subtraction of the absorption (or transparency) spectra of the two probes using two identical IR photo-detectors (PD1 and PD2) in the differential transimpedance amplifier.

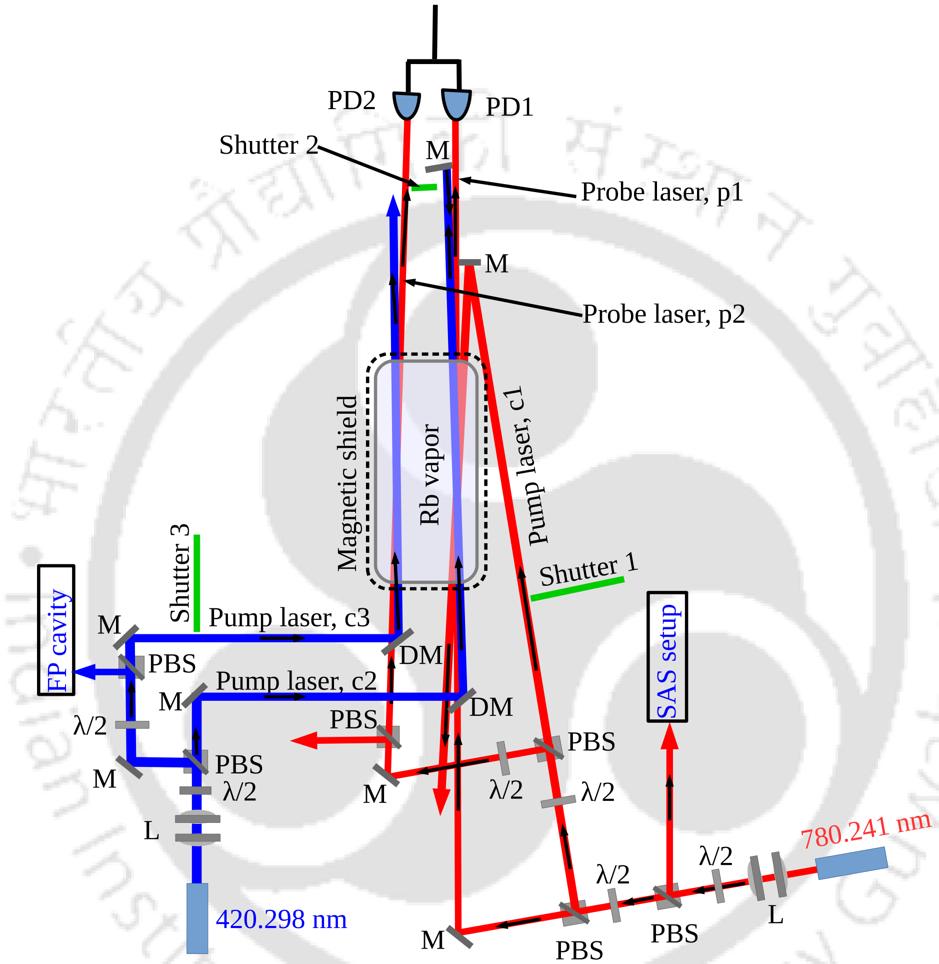

Fig. 6.9: The experimental setup for for resolving the closely spaced hyperfine levels of the $6P_{3/2}$ state in Rb atom using the VIPO and VSS effects

6.3.2 Resolving the $6P_{3/2}$ hyperfine levels in ^{85}Rb

6.3.2.1 The V-type system

The transparency spectrum of the energy scheme in Fig. 6.1a is shown by the red trace of Fig. 6.10a. This spectrum is obtained when all the three shutters in the experimental set-up of Fig. 6.9 are closed. The three peaks of the $6P_{3/2}(F = 2, 3, 4)$ hyperfine levels are merged forming a broad transparency spectrum due to the residual Doppler broadening effect. When shutter 1 is open, dips corresponding to three hyperfine levels are induced inside the broad transparency peaks caused by VIPO at IR transition (see the blue trace of Fig. 6.10a). However, the dips appear very small due to the broad transparency background. The effect is removed when shutter 3 is open to subtract the broad transparency profile and the spectrum of the resolved hyperfine levels is shown by the green trace of Fig. 6.10a. The linewidth of the resolved peaks are as follows: $F = 4$ is 13.3 MHz, $F = 3$ is 14.1 MHz and $F = 2$ is 12.1 MHz. The power of the pump beams labeled c1, c2 and c3 used for optimal signal-to-noise ratio of the spectrum are 276 μW (or peak intensity I=11.7 mW/cm^2), 5.0 mW (or peak intensity I=106.5 mW/cm^2) and 3.6 mW (or peak intensity I=77.2 mW/cm^2) respectively.

Further line narrowing of the resolved peaks is achieved using the configuration shown in Fig. 6.1c i.e., VIPO at IR and VSS at blue transition. The energy configuration scheme in Fig. 6.1c (i.e., VIPO at IR and VSS at blue transition) is implemented in the experimental set-up given in Fig. 6.9, when shutter 1 and shutter 2 are open. Lower power of IR pump beam is used in this configuration since the induced dips by VIPO at IR are enhanced by VSS effect at blue transition. The transparency spectrum of this configuration is shown by the blue trace of Fig. 6.10b. The broad transparency background is removed when shutter 3 is open and the well resolved peaks of the $6P_{3/2}(F = 2, 3, 4)$ hyperfine levels is shown by the green trace of Fig.

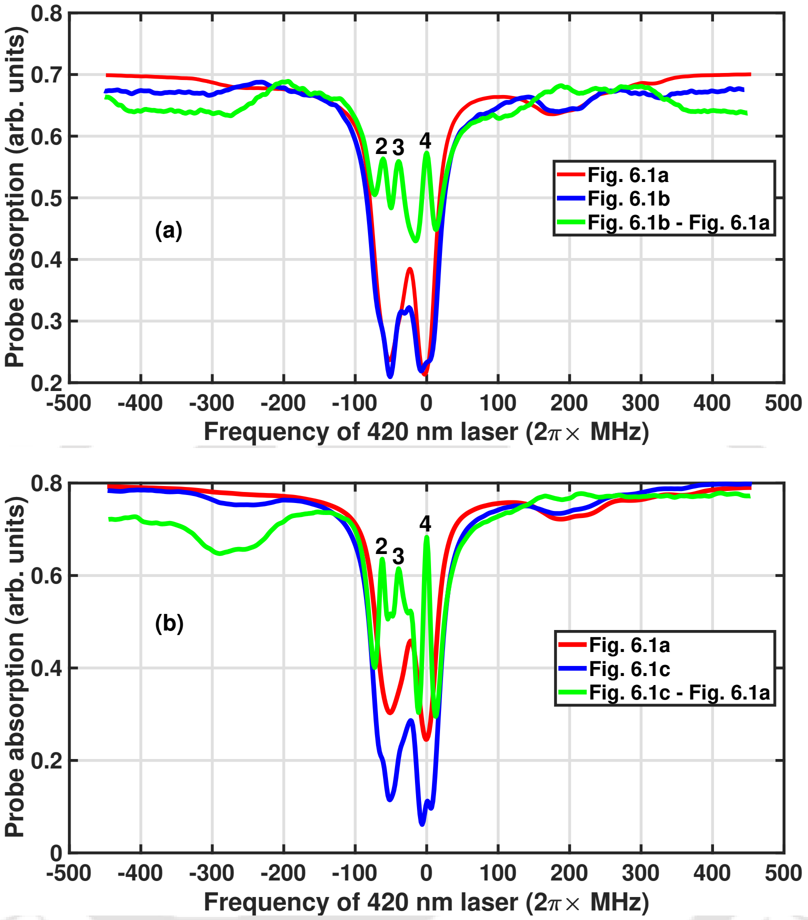

Fig. 6.10: The transparency spectrum of the $6P_{3/2}$ hyperfine levels in ^{85}Rb under various configurations shown in Fig. 6.1. The red trace is for the V-type open system (Fig. 6.1a), the blue trace in Fig. 6.10a is for the V-type open system with VIPO effect at IR transition (Fig. 6.1b) while the blue trace in Fig. 6.10b is for V-type open system with VIPO effect at IR and VSS effect at blue transition (Fig. 6.1c). The green trace is the final result after removing the broad transparency background and it is magnified 3 times for visibility purpose.

6.10b. The linewidth of the resolved peaks are as follows: F = 4 is 10.8 MHz, F = 3 is 9.1 MHz and F = 2 is 11.4 MHz. The power of the pump beams labeled c1, c2 and c3 used for optimal signal-to-noise ratio of the spectrum are 176 μW (or peak intensity I=7.5 mW/cm^2), 6.0 mW (or peak intensity I=127.5 mW/cm^2) and 8.6 mW (or peak intensity I=182.9 mW/cm^2) respectively.

In the final result of the resolved peaks (see the green trace of Fig. 6.10b), there are small peaks between the main peaks of F = 3 and F = 4 and between F = 2 and F = 3. These are not cross-over peaks (or real peaks), but the residue due to incomplete removal of the broad transparency background in the overlapped regions. The effect also occur for the optical pumping system when the broad absorption background is removed (see the green trace of Fig. 6.11b the small peak between F = 2 and F = 3).

6.3.2.2 The optical pumping system

The EA spectrum of the optical pumping system is shown by the red trace in Fig. 6.11. This spectrum is obtained when all the three shutters in the experimental set-up of Fig. 6.9 are closed. The absorption peaks corresponding to the $6P_{3/2}(F = 1, 2, 3)$ hyperfine levels are completely merged. The levels $6P_{3/2}(F = 2, 3)$ are detected by the probe via both the direct decay and indirect decay channels [122] while level $6P_{3/2}(F = 1)$ is detected via the indirect decay channels to $5S_{1/2}(F = 3)$ only. When shutter 1 is open, dips corresponding to the hyperfine levels are induced inside the broad EA peaks due to VIPO at IR transition (see the blue trace of Fig. 6.11a). The dips appear small due to broad EA background caused by the residual Doppler broadening effect. The broad EA background is removed when shutter 3 is open and the dips corresponding to the hyperfine levels $6P_{3/2}(F = 1, 2)$ are still not resolved while the $6P_{3/2}(F = 3)$ peak is resolved (see the green trace of Fig. 6.11a). The linewidth of the resolved peak F = 3 is 13.9 MHz. The power of the pump beams labeled c1, c2 and c3 used for optimal signal-to-noise ratio of the spectrum are 806 μW (or peak intensity I=34.2 mW/cm^2), 5.0 mW (or peak intensity I=106.3 mW/cm^2) and 1.8 mW (or peak intensity I=39.0 mW/cm^2) respectively.

The peaks corresponding to the $6P_{3/2}(F = 1, 2, 3)$ hyperfine levels, can be completely resolved using the configuration shown in Fig. 6.5c i.e., VIPO at IR and VSS at blue transition. This configuration is implemented when shutter 1 and shutter 2 are open in the experimental set-up of Fig. 6.9. The broad EA spectrum is removed when shutter 3 is open and the green trace of Fig. 6.11b shows well resolved peaks of the $6P_{3/2}(F = 1, 2, 3)$ hyperfine levels. Note, the frequency scaling of the spectra in Fig. 6.11 is assigned using the peak locations of F = 2 and F = 3 after the complete resolution of all the three peaks of $6P_{3/2}(F = 1, 2, 3)$ hyperfine levels. The linewidth of the resolved peaks are as follows: F = 3 is 9.8 MHz, F = 2 is 10.1 MHz and F = 1 is 7.2 MHz. The power of the pump beams labeled c1, c2 and c3 used for optimal signal-to-noise ratio of the spectrum are 276 μW (or peak intensity I=11.7 mW/cm^2), 5.0 mW (or peak intensity I=106.7 mW/cm^2) and 15.2 mW (or peak intensity I=322.3 mW/cm^2) respectively.

Besides the main peaks due to near zero-velocity groups atoms in Fig. 6.11a, the extra peaks outside the main spectrum are caused by groups of atoms moving with velocities around 94 m/s and 143 m/s respectively (since the linewidth of the transition is finite, a finite range of velocities contributes). Atoms moving with velocities around 94 m/s and 143 m/s along the propagation direction of the IR probe, will see the probe laser to be on resonance with the $5S_{1/2}(F = 3) \rightarrow 5P_{3/2}(F = 3)$ and $5S_{1/2}(F = 3) \rightarrow 5P_{3/2}(F = 2)$ transitions respectively. The corresponding extra peaks location will be at 224 MHz and 342 MHz from the main peaks. In Fig. 6.11b, the counter-propagating blue laser beams will form extra peaks on both the left and right side of the main peaks. Ideally the extra peak on the right side of the green spectrum should vanish, but it is still visible due to incomplete subtraction.

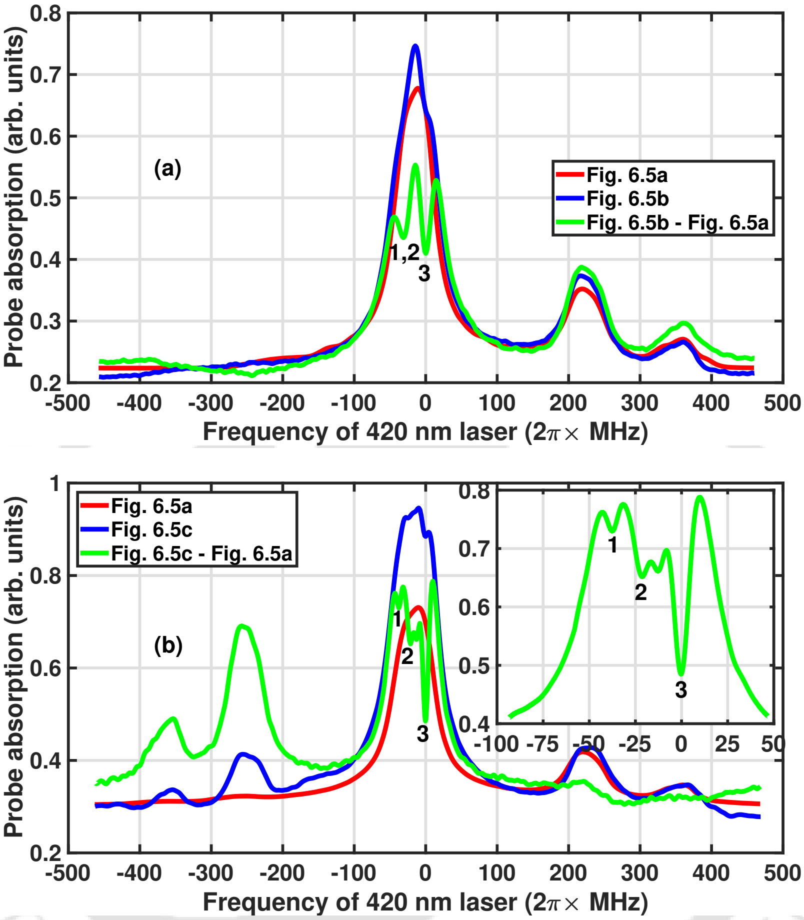

Fig. 6.11: The EA spectrum of the $6P_{3/2}$ hyperfine levels in ^{85}Rb under various configurations shown in Fig. 6.5. The red trace is for the optical pumping system (Fig. 6.5a), the blue trace in Fig. 6.11a is for the optical pumping system with VIPO effect at IR transition (as shown in Fig. 6.5b) while the blue trace in Fig. 6.11b is for the optical pumping system with VIPO effect at IR and VSS effect at blue transition (Fig. 6.5c). The green trace is the final result after removing broad absorption background and it is magnified 3 time for visibility purpose.

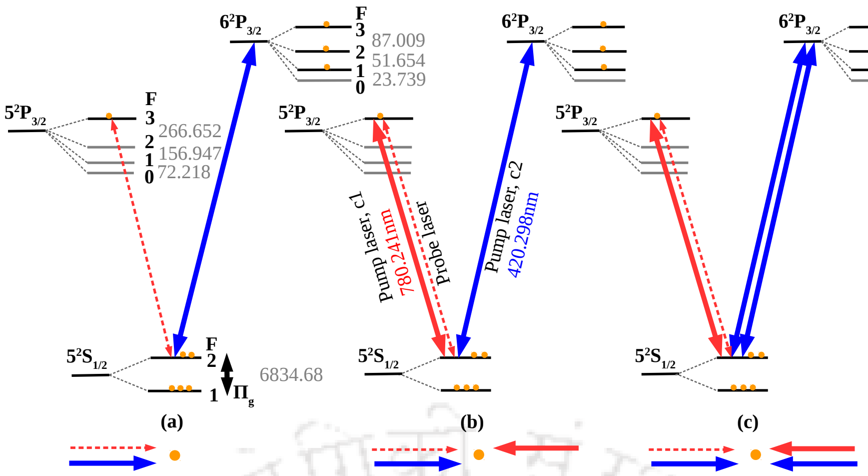

Fig. 6.12: Energy levels (^{87}Rb) with hyperfine splitting (in MHz) and the various transitions in different configurations for EIT. (a) V-type open system, (b) V-type open system with the VIPO effect at IR transition (c) V-type open system with the VIPO effect at IR transition and VSS effect at blue transition. $\Pi_g \approx 40$ kHz [11] is the ground state mixing rate.

6.3.3 Resolving the $6P_{3/2}$ hyperfine levels in ^{87}Rb

6.3.3.1 The V-type system

The $6P_{3/2}$ hyperfine levels of ^{87}Rb is resolved using the configurations shown in Fig. 6.12. The 780 nm probe beam and the counter-propagating pump are locked to resonance on $5S_{1/2}(F = 2) \leftrightarrow 5P_{3/2}(F = 3)$ cycling transition which has a lifetime, $\tau_1 = 26.25$ ns [99, 102, 117, 118]. The absorption of the probe is monitored as the co-propagating 420 nm pump laser scans the $5S_{1/2}(F = 2) \leftrightarrow 6P_{3/2}$ weak transition which has a lifetime, $\tau_2 = 112$ ns [51, 102].

The transparency spectrum of the $6P_{3/2}(F = 1, 2, 3)$ hyperfine levels (when all the three shutters are closed) is shown by the red trace in Fig. 6.13a. The peaks of the $6P_{3/2}(F = 2, 3)$ hyperfine levels are well resolved but the peaks of $6P_{3/2}(F = 1, 2)$ are partially resolved due to the residual Doppler broadening effect. The peaks corresponding to the $6P_{3/2}(F = 1, 2, 3)$ hyperfine levels are resolved using the configuration shown in Fig. 6.12b (i.e., VIPO at IR transition). The configuration is implemented when the shutter 1 is open in the experimental set-up of Fig. 6.9. The dips induced inside the broad transparency peaks (by VIPO at IR transition) corresponds to the three hyperfine levels of the $6P_{3/2}(F = 1, 2, 3)$ state (see the blue trace of Fig. 6.13a). The broad transparency spectrum is removed when shutter 3 and the well resolved hyperfine levels $6P_{3/2}(F = 1, 2, 3)$ are shown by the green trace of Fig. 6.13a. The linewidth of the resolved peaks are as follows: F = 3 is 16.4 MHz, F = 2 is 17.6 MHz and F = 1 is 17.1 MHz. The power of the pump beams labeled c1, c2 and c3 used for optimal signal-to-noise ratio of the spectrum are 601 μW (or peak intensity I=25.5 mW/cm^2), 4.8 mW (or peak intensity I=101.8 mW/cm^2) and 3.7 mW (or peak intensity I=78.5 mW/cm^2) respectively.

Further line narrowing is achieved using the configuration shown in Fig. 6.12c for ^{87}Rb. When shutters 1 and 2 are open, the dips induced by VIPO at IR and VSS at blue transition inside the broad transparency peaks corresponds to the three hyperfine levels of the $6P_{3/2}(F = 1, 2, 3)$ state (see the blue trace of Fig. 6.13b). The residual Doppler broadening effect is removed when shutter 3 is open and the spectrum of the resolved hyperfine levels is shown by the green trace of Fig. 6.13b. The linewidth of the resolved peaks are as follows: F = 3 is 14.4 MHz, F = 2 is 15.7 MHz and F = 1 is 15.8 MHz. The power of the pump beams labeled c1, c2 and c3 used for optimal signal-to-noise ratio of the spectrum are 302 μW (or peak intensity I=12.8 mW/cm^2), 4.8 mW (or peak intensity I=102.3 mW/cm^2) and 13.2 mW (or peak intensity I=280.1 mW/cm^2) respectively.

6.3.3.2 The optical pumping system

The energy level scheme of this system is given in Fig. 6.14a and the 780 nm laser beams (probe and pump) are locked to resonance on $5S_{1/2}(F = 2) \leftrightarrow 5P_{3/2}(F = 3)$ transition. The absorption of the probe is monitored as the co-propagating 420 nm

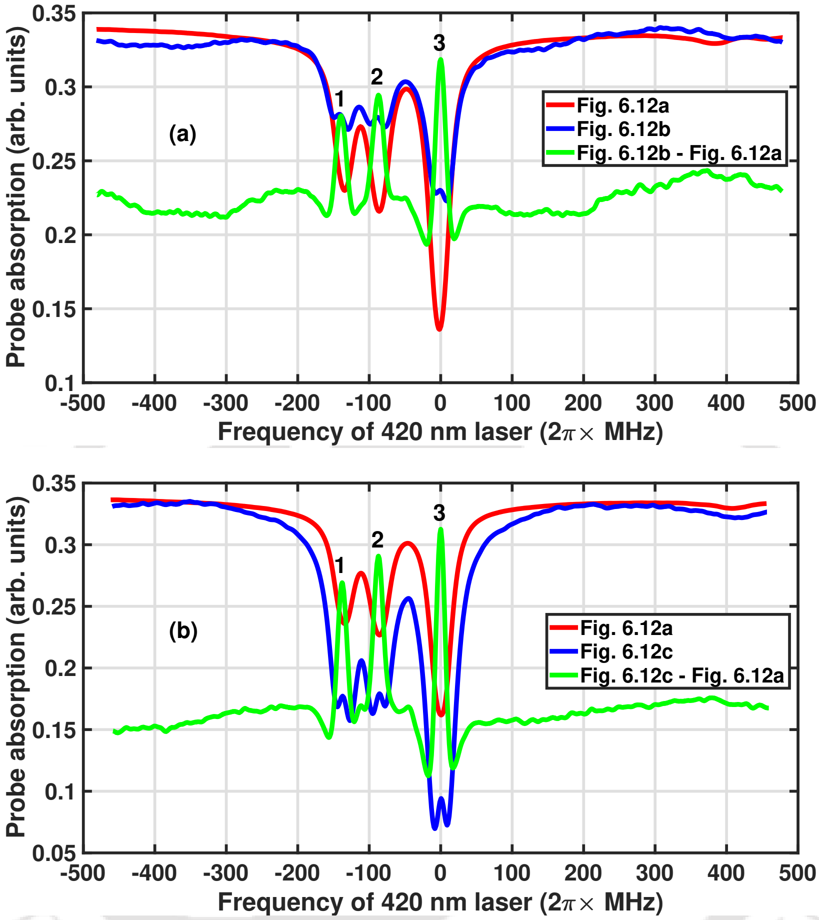

Fig. 6.13: The transparency spectrum of the $6P_{3/2}$ hyperfine levels in ^{87}Rb under various configurations shown in Fig. 6.12. The red trace is for the V-type open system (Fig. 6.12a), the blue trace in Fig. 6.13a is for the V-type open system with VIPO effect at IR transition (Fig. 6.12b) while the blue trace in Fig. 6.13b is for V-type open system with VIPO effect at IR and VSS effect at blue transition (Fig. 6.12c). The green trace is the final result after removing the broad transparency background and it is magnified 3 times for visibility purpose.

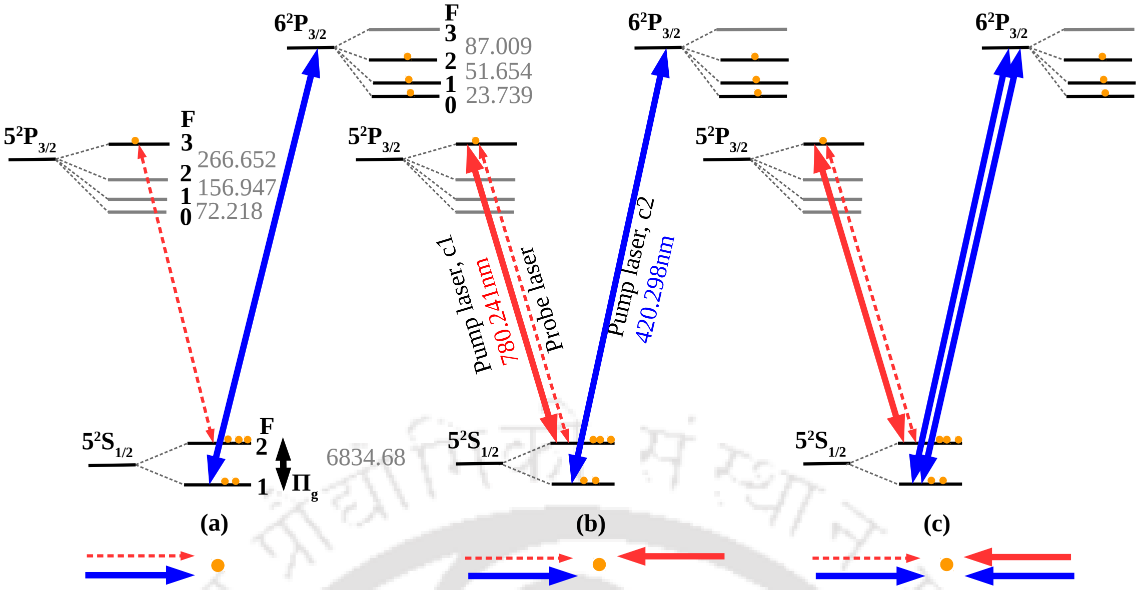

Fig. 6.14: Energy levels (^{87}Rb) with hyperfine splitting (in MHz) and the various transitions in different configurations for EA. (a) optical pumping system, (b) optical pumping system with the VIPO effect at IR transition (c) optical pumping system with the VIPO effect at IR transition and VSS effect at blue transition. $\Pi_g \approx 40$ kHz [11] is the ground state mixing rate.

pump laser scans around the $6P_{3/2}$ hyperfine levels on $5S_{1/2}(F = 1) \rightarrow 6P_{3/2}$ transition. The EA spectrum (when all the three shutters are closed) is shown in Fig. 6.15a by the red trace. The absorption peaks corresponds to the $6P_{3/2}(F = 0, 1, 2)$ hyperfine levels in ^{87}Rb. The peaks for $6P_{3/2}(F = 0, 1)$ are compltely merged while the peaks for $6P_{3/2}(F = 1, 2)$ are partialy merged. The levels $6P_{3/2}(F = 1, 2)$ are detected by the probe via both the direct decay and indirect decay channels [122] while level $6P_{3/2}(F = 0)$ is detected via the indirect decay channels to $5S_{1/2}(F = 2)$ only.

The peaks corresponding to the $6P_{3/2}(F = 0, 1, 2)$ hyperfine levels are resolved using the configuration shown in Fig. 6.14b (i.e., VIPO at IR transition). When shutter 1 is open, dips corresponding to the hyperfine levels are induced inside the broad EA peaks due to VIPO at IR transition (see the blue trace of Fig. 6.15a). The dips appear small due to broad EA background caused by the residual Doppler broadening effect. The broad EA background is removed when shutter 3 is open and the dips corresponding to the hyperfine levels $6P_{3/2}(F = 0, 1, 2)$ are resolved (see the green trace of Fig. 6.15a). The linewidth of the resolved peaks are as follows: F = 2 is 19.4 MHz, F = 1 is 14.8 MHz and F = 0 is 10.5 MHz. The power of the pump beams labeled c1, c2 and c3 used for optimal signal-to-noise ratio of the spectrum are 1.1 mW (or peak intensity $I = 45.4$ mW/cm^2), 4.3 mW (or peak intensity $I = 90.4$ mW/cm^2) and 3.4 mW (or peak intensity $I = 72.6$ mW/cm^2) respectively.

Large and narrow peaks are achieved using the configuration shown in Fig. 6.14b (i.e., VIPO at IR and VSS at blue transition). When shutters 1 and 2 are open, dips corresponding to the hyperfine levels $6P_{3/2}(F = 0, 1, 2)$ are induced inside the broad EA peaks due to VIPO at IR and VSS at blue transition (see the blue trace of Fig. 6.15b). The broad EA background is removed when shutter 3 is open and the dips corresponding to the hyperfine levels $6P_{3/2}(F = 0, 1, 2)$ are resolved (see the green trace of Fig. 6.15b). The linewidth of the resolved peaks are as follows: F = 2 is 16.4 MHz, F = 1 is 13.1 MHz and F = 0 is 12.3 MHz. The power of the pump beams labeled c1, c2 and c3 used for optimal signal-to-noise ratio of the spectrum are 823 μW (or peak intensity I=35.0 mW/cm^2), 4.8 mW (or peak intensity I=102.3 mW/cm^2) and 15.3 mW (or peak intensity I=325.5 mW/cm^2) respectively.

6.3.3.3 Effects of Power broadening on the resolution

The contribution of the IR pump power broadening effect to the final result (i.e., the resolved spectrum of the $6P_{3/2}$ state), is illustrated in Fig. 6.16a. The configuration used here is given in Fig. 6.14b (i.e., VIPO at IR transition) for the case of ^{87}Rb. The power of the blue pump laser beams is fixed (i.e., c2 is 4.2 mW and c3 is 3.2 mW) as the the power of IR pump is changed. At 1 mW of the IR pump, all the three peaks corresponding to the $6P_{3/2}(F = 0, 1, 2)$ hyperfine levels are well resolved (see the red trace of Fig. 6.16a). However, as the IR pump power is increased to 5 mW,

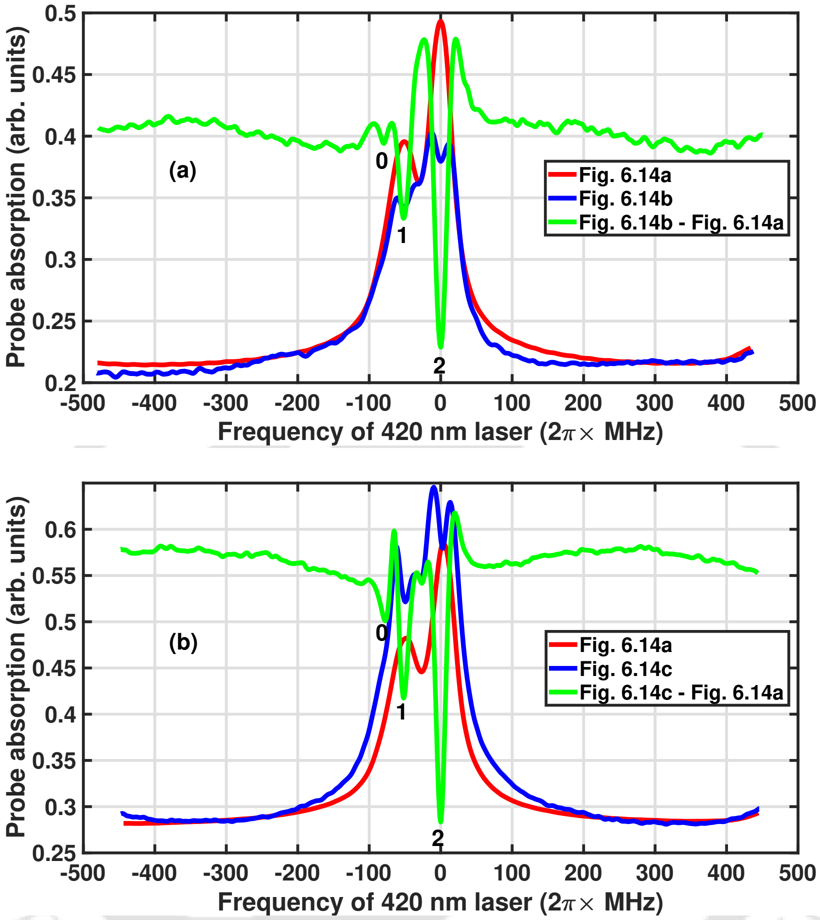

Fig. 6.15: The EA spectrum of the $6P_{3/2}$ hyperfine levels in ^{87}Rb under various configurations shown in Fig. 6.14. The red trace is for the optical pumping system (Fig. 6.14a), the blue trace in Fig. 6.15a is for the optical pumping system with VIPO effect at IR transition (Fig. 6.14b) while the blue trace in Fig. 6.15b is for optical pumping system with VIPO effect at IR and VSS effect at blue transition (Fig. 6.14c). The green trace is the final result after removing the broad transparency background and it is magnified 3 times for visibility purpose.

the peaks corresponding to the $6P_{3/2}(F = 0, 1)$ are completely merged as shown by the green trace of Fig. 6.16a. High intensity of the IR pump broadens the VIPO dips and limits the resolution of the closely spaced hyperfine levels of F = 0 and F = 1 which are 23.739 MHz apart [21]. The frequency scaling of the spectra in Fig. 6.16a is assigned using the resolved peak locations of F = 1 and F = 2 of the red trace. The variation of the linewidth of the resolved peak corresponding to F = 2 with the IR pump power is shown in Fig. 6.16b.

6.3.3.4 VSS at blue transition for a V-type system

Figs. 6.17 illustrate the energy level scheme of a V-type system in ^{87}Rb with VSS effect only. The IR probe laser is locked to resonance on $5S_{1/2}(F = 1) \leftrightarrow 5P_{3/2}(F = 2)$ transition while the blue pump laser scans the $5S_{1/2}(F = 1) \leftrightarrow 6P_{3/2}$ transition. The transparency spectrum of the $6P_{3/2}(F = 0, 1, 2)$ hyperfine levels (when all the three shutters are closed) is shown by the red trace of Fig. 6.18.

The spurious resonance peaks outside the main spectrum are caused by the non zero velocity group atoms (i.e., atoms moving with velocities 123 m/s and 179 m/s). Atoms moving with velocity 123 m/s will see the 780 nm probe laser to be on resonance with $5S_{1/2}(F = 1) \rightarrow 5P_{3/2}(F = 1)$ transition. The three corresponding spurious resonance peaks are located at 291 MHz from the respective real resonance peaks. Similarly, atoms moving with velocity 179 m/s will be resonant for $5S_{1/2}(F = 1) \rightarrow 5P_{3/2}(F = 0)$ transition and another three manifold of the spurious resonance peaks are located at 425 MHz from the respective real resonance peaks (see the red trace of Fig. 6.18a). The spurious resonance peaks are merged up due to the residual Doppler broadening effect.

When the shutter 2 is open (configuration of Fig. 6.17b), dips corresponding to $6P_{3/2}(F = 0, 1, 2)$ hyperfine levels are induced on the real resonance peaks only by

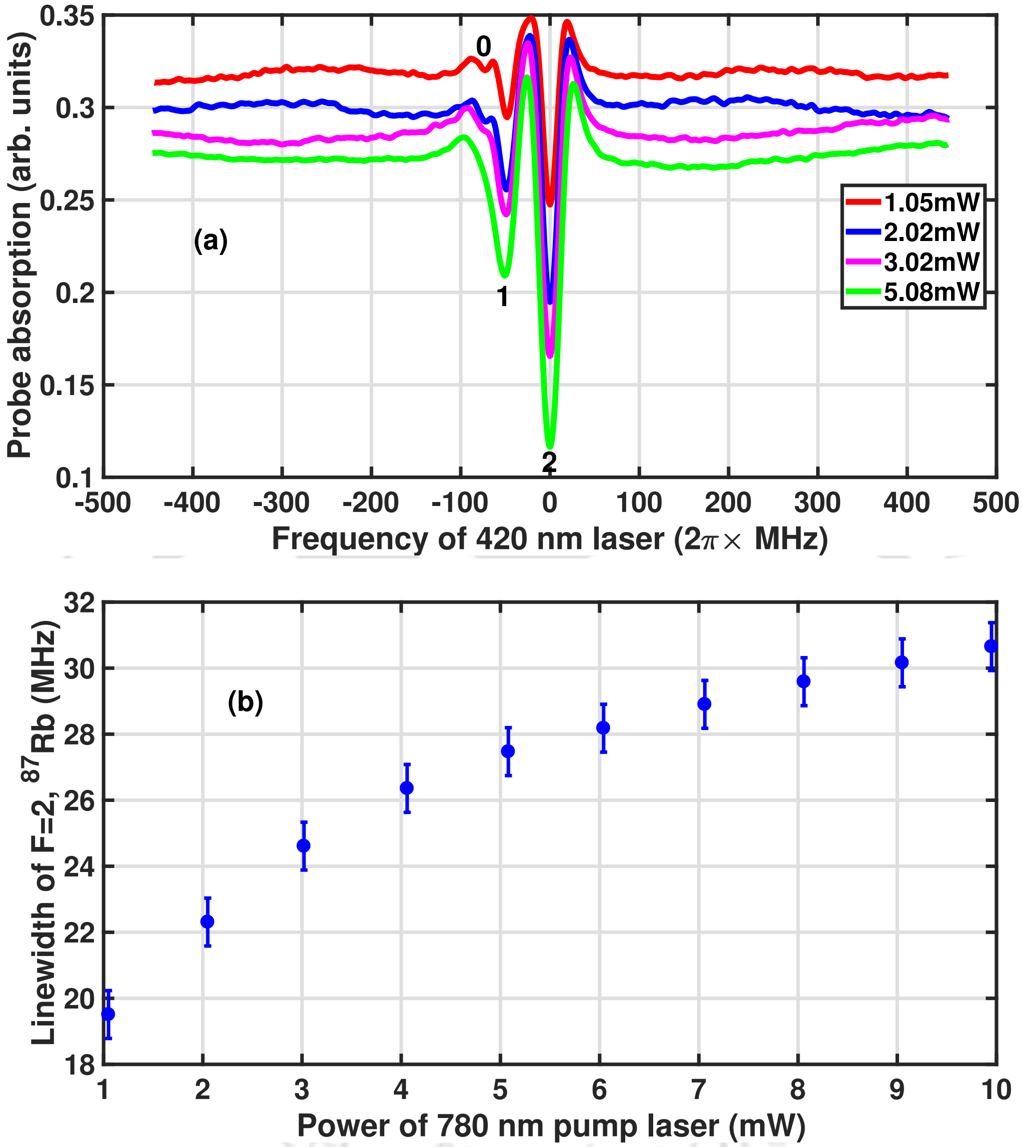

Fig. 6.16: (a) The result of the final spectra of the VIPO dips of the $6P_{3/2}$ hyperfine levels in ^{87}Rb recorded for various powers of IR pump laser after removing the broad absorption background. (b) The variation of the linewidth of the resolved peak F = 2 with the power of IR pump.

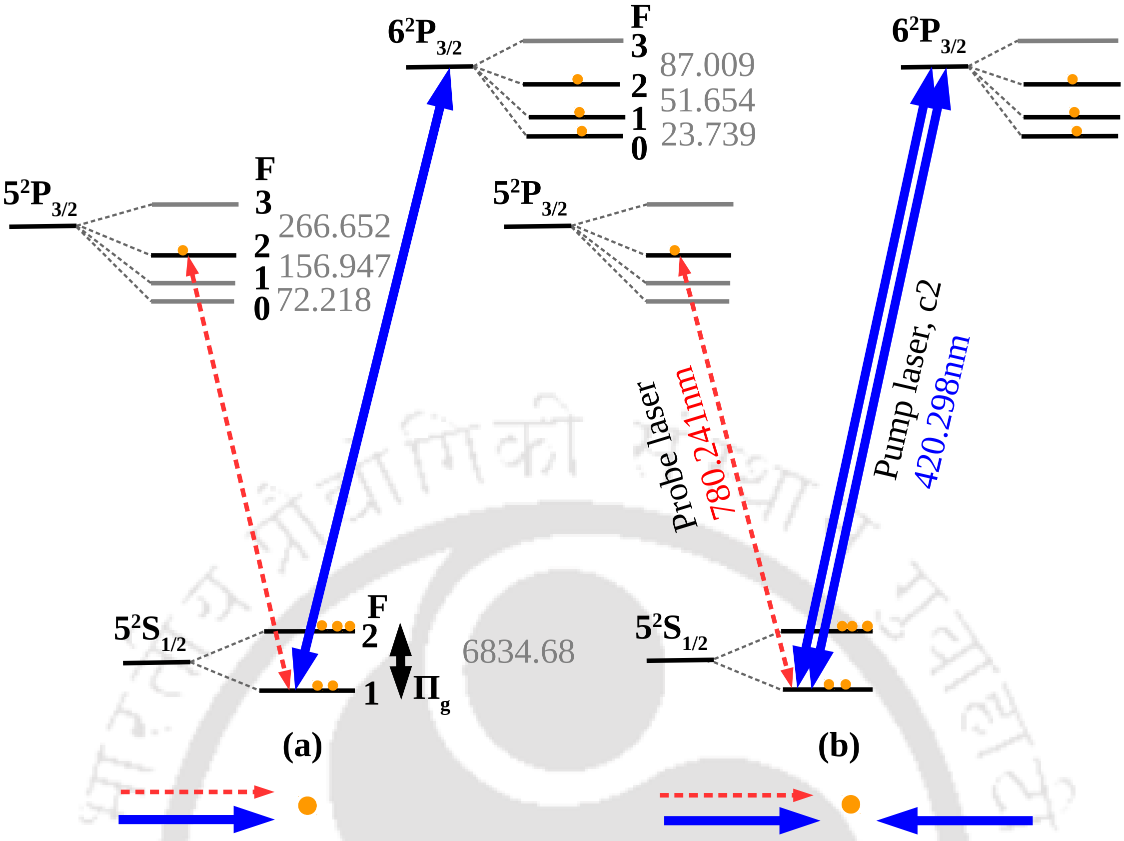

Fig. 6.17: A diagrammatic energy scheme (and hyperfine splitting in MHz) of resolving the $6P_{3/2}$ hyperfine levels in ^{87}Rb using VSS at blue transition.

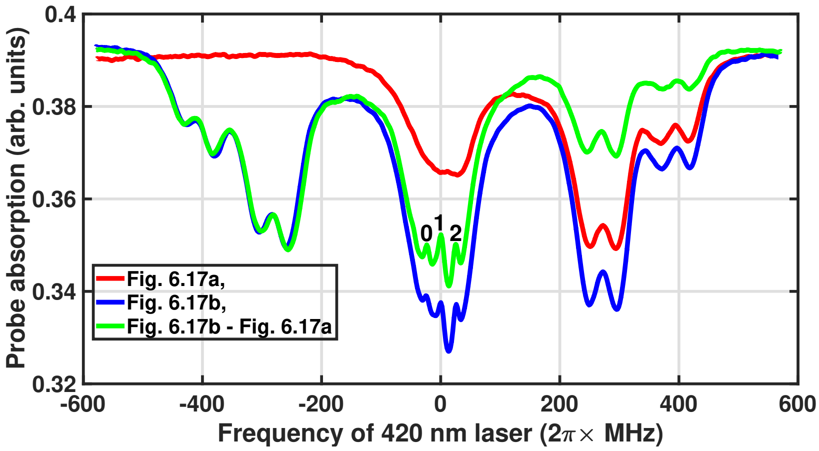

Fig. 6.18: The transparency spectrum of the $6P_{3/2}$ hyperfine levels in ^{87}Rb under various configurations shown in Fig. 6.17. The red trace is for the V-type open system (Fig. 6.17a) and the blue trace is for the V-type open system with VSS effect at blue transition (Fig. 6.17b). The green trace is the final result after removing the broad transparency background.

the VSS at blue transition (see the blue trace of Fig. 6.18b). Note, the VSS effect (or VIPO effect) is a phenomena for near zero velocity group atoms and hence cannot induce dips on the spurious peaks. The spurious resonance peaks appearing on the left side of the real resonance peaks are caused by the counter-propagating blue pump laser beam. The green trace of Fig. 6.18b shows the saturation peaks of the $6P_{3/2}(F = 0, 1, 2)$ hyperfine levels after removing the residual Doppler broadening when shutter 3 is open. The frequency scaling of the spectra in Fig. 6.18 is assigned using the resolved peak locations of F = 1 and F = 2 of the green trace. The power of the pump beams labeled c2 and c3 used for optimal signal-to-noise ratio of the spectrum are 7.8 mW (or peak intensity I = 165.5 mW/cm^2) and 4.4 mW (or peak intensity I = 93.4 mW/cm^2) respectively.

The result of this chapter appear in the following publication: Physical Review A (Phys. Rev. A 103, 013107 (2021); https://doi.org/10.1103/PhysRevA.103.013107).

7

Conclusions and future work

In this thesis work, we have studied the mechanism of induced atomic coherence between multi-level atomic system driven by lasers and their role in the absorption and fluorescence spectrum. In the theoretical study, the electromagnetically induced transparency (EIT) is Autler-Townes splitting (or dressed states) plus quantum interference between the excitation paths of the dressed states. The excitation paths of the dressed states interferes pair-wise and the nature of interference can be constructive, destructive or no interference depending upon the decay rate of the states coupled by the strong control lasers. Further, saturated fluorescence spectroscopy which is a very useful spectroscopic technique for weak transitions was also studied. The fluorescence dip in a fluorescence spectra is caused by velocity selective saturation (VSS) effect and is further modified by velocity induced population oscillation (VIPO) effect.

The theoretical study was experimentally utilized to precisely measure the hyperfine splitting interval of the $6P_{1/2}$ state in ^{87}Rb using double resonance spectroscopy at infrared (strong) transition and blue (weak) transition. The double resonance technique is implemented using EIT effect in a V-type system and enhanced absorption (EA) effect in optical pumping system. The VIPO effect at IR and VSS effect at blue transition were experimentally utilized to resolve closely spaced hyperfine level of the $6P_{3/2}$ state in Rb by eliminating the residual two-photon Doppler broadening in a Doppler mismatched double resonance spectroscopy.

The resolved peaks of the $6P_{3/2}$ state with narrow linewidth, are important for stabilizing the blue laser at a particular transition (i.e., for tight laser locking) for applications in laser cooling and high precision spectroscopy experiments. The spectroscopy of the blue transition is also important for quantum information processing with coherent excitation of Rydberg states in Rb atoms.

Appendices

Appendix A

Analytical solution for probe absorption in a generic multilevel system

The Hamiltonian of the generic system shown in fig. 3.1 in the rotating frame with RWA is given as follows:

$$H = \sum_{j=1}^{n-1} \frac{\Omega_{j,j+1}}{2} |j\rangle \langle j+1| + 0 |1\rangle \langle 1| + \sum_{j=2}^{n} \sum_{i=2}^{j} (-1)^i \delta_{i-1,i} |j\rangle \langle j| , \tag{A.1}$$

where, $\Omega_{j,j+1}$ is Rabi frequency of the lasers driving levels $|j\rangle \leftrightarrow |j+1\rangle$ and $\delta_{j,j+1}$ is the detuning. The probe laser drives $|1\rangle \rightarrow |2\rangle$ transition while the control lasers drives $|2\rangle \leftrightarrow |3\rangle \leftrightarrow |4\rangle , ..., |n-1\rangle \leftrightarrow |n\rangle$ transitions. Time evolution of the population in the various levels is given as follows:

$$
\begin{aligned}
\dot{\rho}_{11} &= -\Gamma_1\rho_{11} + \sum_{i=2}^{n}\Gamma_{i1}\rho_{ii} + \frac{i}{2}\Omega_{12}^{*}\rho_{12} - \frac{i}{2}\Omega_{12}\rho_{21}, \\
\dot{\rho}_{22} &= -\Gamma_2\rho_{22} + \sum_{i=1,i\neq 2}^{n}\Gamma_{i2}\rho_{ii} + \frac{i}{2}\Omega_{12}\rho_{21} - \frac{i}{2}\Omega_{12}^{*}\rho_{12} + \frac{i}{2}\Omega_{23}^{*}\rho_{23} - \frac{i}{2}\Omega_{23}\rho_{32}, \\
&\vdots \\
\dot{\rho}_{jj} &= -\Gamma_j\rho_{jj} + \sum_{i=1,i\neq j}^{n}\Gamma_{ij}\rho_{ii} + \frac{i}{2}\Omega_{j-1,j}\rho_{j,j-1} - \frac{i}{2}\Omega_{j-1,j}^{*}\rho_{j-1,j} + \frac{i}{2}\Omega_{j,j+1}^{*}\rho_{j,j+1} - \frac{i}{2}\Omega_{j,j+1}\rho_{j+1,j}, \\
&\vdots \\
\dot{\rho}_{nn} &= -\Gamma_n\rho_{nn} + \sum_{i=1,i\neq n}^{n}\Gamma_{in}\rho_{ii} + \frac{i}{2}\Omega_{n-1,n}^{*}\rho_{n-1,n} - \frac{i}{2}\Omega_{n-1,n}\rho_{n,n-1}, \qquad \text{(A.2)}
\end{aligned}
$$

where, Γ_{ij} is the spontaneous decay rate of level $|i\rangle$ into $|j\rangle$ and $\Gamma_i \left(= \sum_{j=1,j\neq i}^{n}\Gamma_{ij}\right)$ is the total decay rate of the level $|i\rangle$. The time evolution of the coherence between level $|1\rangle$ and various other levels is given as follows:

$$
\begin{aligned}
\dot{\rho}_{12} &= -\left[\frac{\Gamma_1+\Gamma_2}{2} - i\delta_{12}\right]\rho_{12} + \frac{i}{2}\Omega_{12}(\rho_{11}-\rho_{22}) + \frac{i}{2}\Omega_{23}^{*}\rho_{13}, \\
\dot{\rho}_{13} &= -\left[\frac{\Gamma_1+\Gamma_3}{2} - i\left(\delta_{12}-\delta_{23}\right)\right]\rho_{13} - \frac{i}{2}\Omega_{12}\rho_{23} + \frac{i}{2}\Omega_{23}\rho_{12} + \frac{i}{2}\Omega_{34}^{*}\rho_{14}, \\
&\vdots \\
\dot{\rho}_{1n-1} &= -\left[\frac{\Gamma_1+\Gamma_{n-1}}{2} - i\left(\sum_{i=2}^{n-1}(-1)^{i}\delta_{i-1,i}\right)\right]\rho_{1n-1} \\
&\quad - \frac{i}{2}\Omega_{12}\rho_{2,n-1} + \frac{i}{2}\Omega_{n-2,n-1}\rho_{1,n-2} + \frac{i}{2}\Omega_{n-1,n}^{*}\rho_{1n}, \qquad \text{(A.3)} \\
\dot{\rho}_{1n} &= -\left[\frac{\Gamma_1+\Gamma_n}{2} - i\left(\sum_{i=2}^{n}(-1)^{i}\delta_{i-1,i}\right)\right]\rho_{1n} - \frac{i}{2}\Omega_{12}\rho_{2n} + \frac{i}{2}\Omega_{n-1,n}\rho_{1,n-1}.
\end{aligned}
$$

In the steady state condition (i.e., $\dot{\rho}_{ij} = 0$ for all i and j) $\Omega_{12}\rho_{23}$, $\Omega_{12}\rho_{24}\cdots\Omega_{12}\rho_{2n} \approx 0$ and $\rho_{22} \approx 0$ for a weak probe. Using this approximation, the density matrix element

ρ_{13} is expressed as:

$$\rho_{13} = \cfrac{\frac{i}{2}\frac{\Omega_{23}}{\gamma_{13}}}{1+\cfrac{\frac{1}{4}\frac{|\Omega_{34}|^2}{\gamma_{13}\gamma_{14}}}{1+\cfrac{\frac{1}{4}\frac{|\Omega_{45}|^2}{\gamma_{14}\gamma_{15}}}{1+\cfrac{\frac{1}{4}\frac{|\Omega_{56}|^2}{\gamma_{15}\gamma_{16}}}{1+\cfrac{\cdot}{1+\cfrac{\cdot}{1+\frac{1}{4}\frac{|\Omega_{n-1,n}|^2}{\gamma_{1,n-1}\gamma_{1n}}}}}}}}, \tag{A.4}$$

while the density matrix element ρ_{12} is expressed in terms of ρ_{11} and ρ_{13} as follows:

$$\rho_{12} \approx \frac{i}{2}\frac{\Omega_{12}}{\gamma_{12}}\rho_{11} + \frac{i}{2}\frac{\Omega_{23}^*}{\gamma_{12}}\rho_{13}. \tag{A.5}$$

The substitution of Eq. A.4 into Eq. A.5 yields the expression of ρ_{12} in terms of ρ_{11} as follows,

$$\rho_{12} = \cfrac{\frac{i}{2}\frac{\Omega_{12}}{\gamma_{12}}\rho_{11}}{1+\cfrac{\frac{1}{4}\frac{|\Omega_{23}|^2}{\gamma_{12}\gamma_{13}}}{1+\cfrac{\frac{1}{4}\frac{|\Omega_{34}|^2}{\gamma_{13}\gamma_{14}}}{1+\cfrac{\frac{1}{4}\frac{|\Omega_{45}|^2}{\gamma_{14}\gamma_{15}}}{1+\cfrac{\frac{1}{4}\frac{|\Omega_{56}|^2}{\gamma_{15}\gamma_{16}}}{1+\cfrac{\cdot}{1+\cfrac{\cdot}{1+\frac{1}{4}\frac{|\Omega_{n-1,n}|^2}{\gamma_{1,n-1}\gamma_{1n}}}}}}}}}. \tag{A.6}$$

The imaginary part of ρ_{12}, Im(ρ_{12}) represents the absorption of the probe laser while the real part represents the dispersion.

Appendix B

Analytical solution of the excited state population in two level system

The steady state analytical solution of $\rho_{ee}^{(0)}$, $\rho_{ee}^{(+1)}$ and $\rho_{ee}^{(-1)}$ for a two level system given in Eq. 5.8 (see chapter 5) are as follows, where the γ_i $i = 1, 2, 3, ...$ are given as:

$$\begin{aligned}
\gamma_1 =& \Gamma^2 + \delta^2, \;\; \gamma_2 = \frac{\Gamma^2}{4} + \Delta^2, \;\; \gamma_3 = \frac{\Gamma^2}{4} + (\Delta + \delta)^2, \;\; \gamma_4 = \frac{\Gamma^2}{4} + (\Delta - \delta)^2, \\
\gamma_5 =& \frac{\Gamma^2}{4} - \Delta(\Delta + \delta), \;\; \gamma_6 = \frac{\Gamma^2}{4} + \delta^2 - \Delta^2, \;\; \gamma_7 = \frac{\Gamma^2}{4} + \Delta(\Delta - \delta), \;\; \gamma_8 = \frac{\Gamma^2}{2} + \delta\Delta, \\
\gamma_9 =& \frac{\Gamma^2}{2} - \delta(\Delta + \delta), \;\; \gamma_{10} = \frac{\Gamma^2}{2} + \delta(\Delta - \delta), \;\; \gamma_{11} = \frac{3\Gamma^2}{4} + \Delta^2 - \delta^2, \\
\gamma_{12} =& \frac{3\Gamma^2}{4} - \Delta(\Delta - \delta).
\end{aligned}$$

$$\rho_{ee}^{(0)} = \frac{1}{2}\left\{\frac{\frac{\Omega^2}{2}(\frac{\Gamma^2}{2} + (\Delta + kv_x)^2 + (\Delta - kv_x)^2)}{(\frac{\Gamma^2}{4} + (\Delta + kv_x)^2)(\frac{\Gamma^2}{4} + (\Delta - kv_x)^2)\left[1 + \frac{\frac{\Omega^2}{2}(\frac{\Gamma^2}{2}+(\Delta+kv_x)^2+(\Delta-kv_x)^2)}{(\frac{\Gamma^2}{4}+(\Delta+kv_x)^2)(\frac{\Gamma^2}{4}+(\Delta-kv_x)^2)}\right]}\right\} \times \mathrm{B}, \tag{B.1}$$

$$\rho_{ee}^{(+1)} = \left\{\frac{2\gamma_4\Omega^2(\gamma_2\gamma_9 + \gamma_3\gamma_8) + \Omega^4(2\gamma_4\gamma_5 + \gamma_2\gamma_4 + \gamma_2\gamma_6 + \gamma_3\gamma_7 + \gamma_3\gamma_4)}{2(4\gamma_1\gamma_2\gamma_3\gamma_4 + 4\Omega^2(\gamma_2\gamma_3\gamma_{10} + \gamma_2\gamma_4\gamma_9 + \gamma_3\gamma_4\gamma_8) + \Omega^4(\gamma_2\gamma_4 + 2\gamma_2\gamma_6 + 2\gamma_4\gamma_5 + \gamma_2\gamma_3 + 2\gamma_3\gamma_7 + \gamma_3\gamma_4))}\right\} \times \mathrm{C}, \tag{B.2}$$

$$\rho_{ee}^{(-1)} = \rho_{ee}^{(+1)},\ \ \rho_{gg}^{(+1)} = -\rho_{ee}^{(+1)},\ \ \rho_{gg}^{(-1)} = -\rho_{ee}^{(-1)}\ \text{ and }\ \rho_{gg}^{(0)} = 1 - \rho_{ee}^{(0)},$$

$$\mathrm{B} = \frac{(\gamma_3\Omega^2 + \gamma_2(2\gamma_3 + \Omega^2))(8\gamma_1(\gamma_2 + \gamma_3)\gamma_4 + \Omega^2(4\gamma_2(2\gamma_{10} + 2\gamma_4 + \Omega^2) + 4\gamma_3(2\gamma_{10} + 2\gamma_4 + \Omega^2) + 4\gamma_5(4\gamma_4 + \Omega^2)))}{(\gamma_2 + \gamma_3)(8\gamma_1\gamma_4(\gamma_3\Omega^2 + \gamma_2(2\gamma_3 + \Omega^2)) + \Omega^2(4\gamma_5\Omega^2(6\gamma_4 + \Omega^2) + 2\gamma_3(\Omega^2(4\gamma_{11} + 2\Omega^2) + \gamma_4(8\gamma_8 + 6\Omega^2)) + 2\gamma_2(2\gamma_3(4\gamma_{10} + \Omega^2) + \Omega^2(4\gamma_{12} + 2\Omega^2) + \gamma_4(8\gamma_9 + 6\Omega^2))))},$$

$$\mathrm{C} = \frac{4\gamma_4(8\gamma_1\gamma_2\gamma_3\gamma_4 + \Omega^2(4\gamma_4\gamma_5\Omega^2 + \gamma_3(4\gamma_7\Omega^2 + 2\gamma_4(4\gamma_8 + \Omega^2)) + \gamma_2(4\gamma_6\Omega^2 + 2\gamma_3(4\gamma_{10} + \Omega^2) + 2\gamma_4(4\gamma_9 + \Omega^2))))}{(16\gamma_1\gamma_4^2(\gamma_3\Omega^2 + \gamma_2(2\gamma_3 + \Omega^2)) + \Omega^2(8\gamma_4\gamma_5\Omega^2(6\gamma_4 + \Omega^2) + \gamma_3(4\gamma_4\Omega^4 + 4\gamma_4\Omega^2(4\gamma_{11} + \Omega^2) + 8\gamma_4^2(4\gamma_8 + 3\Omega^2)) + 4\gamma_2\gamma_4(2\gamma_3(4\gamma_{10} + \Omega^2) + \Omega^2(4\gamma_{12} + 2\Omega^2) + \gamma_4(8\gamma_9 + 6\Omega^2))))}.$$

Appendix C

Floquet expansion

C.1 VIPO at IR transition for a V-type closed system

We consider a V-type closed system with VIPO at IR transition. The dynamics of the atom-field interactions is described by Eq. 2.15 and the Hamiltonian given in Eq. 6.1. The substitution of Eq. 6.1 into Eq. 2.15 yields the following set of equations of motion with time-dependent coefficients:

$$\begin{aligned}
\dot{\rho}_{12} =& \frac{i}{2}(\Omega_{\mathrm{c1}} + \Omega_{\mathrm{p}} e^{i\delta_1 t})(\rho_{11} - \rho_{22}) - \frac{i\Omega_{\mathrm{c2}}}{2}\rho_{32} - \gamma_{12}\rho_{12}, \\
\dot{\rho}_{13} =& \frac{i\Omega_{\mathrm{c2}}}{2}(\rho_{11} - \rho_{33}) - \gamma_{13}\rho_{13} - \frac{i}{2}(\Omega_{\mathrm{c1}} + \Omega_{\mathrm{p}} e^{i\delta_1 t})\rho_{23}, \\
\dot{\rho}_{22} =& \frac{i}{2}(\Omega_{\mathrm{c1}} + \Omega_{\mathrm{p}} e^{i\delta_1 t})\rho_{21} - \frac{i}{2}(\Omega^*_{\mathrm{c1}} + \Omega^*_{\mathrm{p}} e^{-i\delta_1 t})\rho_{12} - \Gamma_2\rho_{22}, \\
\dot{\rho}_{23} =& -\frac{i}{2}(\Omega^*_{\mathrm{c1}} + \Omega^*_{\mathrm{p}} e^{-i\delta_1 t})\rho_{13} + \frac{i\Omega_{\mathrm{c2}}}{2}\rho_{21} - \gamma_{23}\rho_{23}, \\
\dot{\rho}_{33} =& -\frac{i\Omega^*_{\mathrm{c2}}}{2}\rho_{13} + \frac{i\Omega_{\mathrm{c2}}}{2}\rho_{31} - \Gamma_3\rho_{33},
\end{aligned} \tag{C.1}$$

where, $\gamma_{12} = i\Delta_{\mathrm{c1}} + \gamma^{dec}_{12}$, $\gamma_{13} = i\Delta_{\mathrm{c2}} + \gamma^{dec}_{13}$ and $\gamma_{23} = i(\Delta_{\mathrm{c2}} - \Delta_{\mathrm{c1}}) + \gamma^{dec}_{23}$, $\gamma^{dec}_{ij} = \frac{1}{2}(\Gamma_i + \Gamma_j)$ and Γ_i is the decay rate of the i^{th} level. The remaining density matrix equations are obtained using the population conservation law $\sum_{j=1}^{3}\rho_{jj} = 1$ and the complex conjugate $\dot{\rho}_{ji} = \dot{\rho}^*_{ij}$.

The absorption of the probe field is obtained by considering the steady state solution of Eq. C.1 to first order in the probe field. In the steady state condition, the absorption of the probe laser (which is proportional to the imaginary part of $\rho_{12}^{(+1)}$) is obtained by substituting the truncated series of the Floquet expansion given in Eq. 5.5 up to first-order into Eq. C.1. The coefficients of the same power in $n\delta_1$ are then compared which yields the following set of steady state equations of motion in the Floquet expansion:

$$
\begin{aligned}
\dot{\rho}_{12}^{(n)} &= \frac{i\Omega_{\mathrm{c1}}}{2}(\rho_{11}^{(n)} - \rho_{22}^{(n)}) + \frac{i\Omega_{\mathrm{p}}}{2}(\rho_{11}^{(n-1)} - \rho_{22}^{(n-1)}) - \frac{i\Omega_{\mathrm{c2}}}{2}\rho_{32}^{(n)} - (\gamma_{12} + in\delta_1)\rho_{12}^{(n)},\\
\dot{\rho}_{13}^{(n)} &= \frac{i\Omega_{\mathrm{c2}}}{2}(\rho_{11}^{(n)} - \rho_{33}^{(n)}) - (\gamma_{13} + in\delta_1)\rho_{13}^{(n)} - \frac{i}{2}(\Omega_{\mathrm{c1}}\rho_{23}^{(n)} + \Omega_{\mathrm{p}}\rho_{23}^{(n-1)}),\\
\dot{\rho}_{21}^{(n)} &= \frac{i\Omega^*_{\mathrm{c1}}}{2}(\rho_{22}^{(n)} - \rho_{11}^{(n)}) + \frac{i\Omega^*_{\mathrm{p}}}{2}(\rho_{22}^{(n+1)} - \rho_{11}^{(n+1)}) + \frac{i\Omega^*_{\mathrm{c2}}}{2}\rho_{23}^{(n)} - (\gamma_{21} + in\delta_1)\rho_{21}^{(n)},\\
\dot{\rho}_{22}^{(n)} &= \frac{i}{2}(\Omega_{\mathrm{c1}}\rho_{21}^{(n)} + \Omega_{\mathrm{p}}\rho_{21}^{(n-1)}) - \frac{i}{2}(\Omega^*_{\mathrm{c1}}\rho_{12}^{(n)} + \Omega^*_{\mathrm{p}}\rho_{12}^{(n+1)}) - (\Gamma_2 + in\delta_1)\rho_{22}^{(n)},\\
\dot{\rho}_{23}^{(n)} &= -\frac{i}{2}(\Omega^*_{\mathrm{c1}}\rho_{13}^{(n)} + \Omega^*_{\mathrm{p}}\rho_{13}^{(n+1)}) + \frac{i\Omega_{\mathrm{c2}}}{2}\rho_{21}^{(n)} - (\gamma_{23} + in\delta_1)\rho_{23}^{(n)},\\
\dot{\rho}_{31}^{(n)} &= \frac{i\Omega^*_{\mathrm{c2}}}{2}(\rho_{33}^{(n)} - \rho_{11}^{(n)}) - (\gamma_{31} + in\delta_1)\rho_{31}^{(n)} + \frac{i}{2}(\Omega^*_{\mathrm{c1}}\rho_{32}^{(n)} + \Omega^*_{\mathrm{p}}\rho_{32}^{(n+1)}),\\
\dot{\rho}_{32}^{(n)} &= \frac{i}{2}(\Omega_{\mathrm{c1}}\rho_{31}^{(n)} + \Omega_{\mathrm{p}}\rho_{31}^{(n-1)}) - \frac{i\Omega^*_{\mathrm{c2}}}{2}\rho_{12}^{(n)} - (\gamma_{32} + in\delta_1)\rho_{32}^{(n)},\\
\dot{\rho}_{33}^{(n)} &= -\frac{i\Omega^*_{\mathrm{c2}}}{2}\rho_{13}^{(n)} + \frac{i\Omega_{\mathrm{c2}}}{2}\rho_{31}^{(n)} - (\Gamma_3 + in\delta_1)\rho_{33}^{(n)}.
\end{aligned}
\tag{C.2}
$$

The imaginary part of the density matrix element $\rho_{12}^{(+1)}$ is proportional to probe absorption and is shown by the red trace of Fig. C.1.

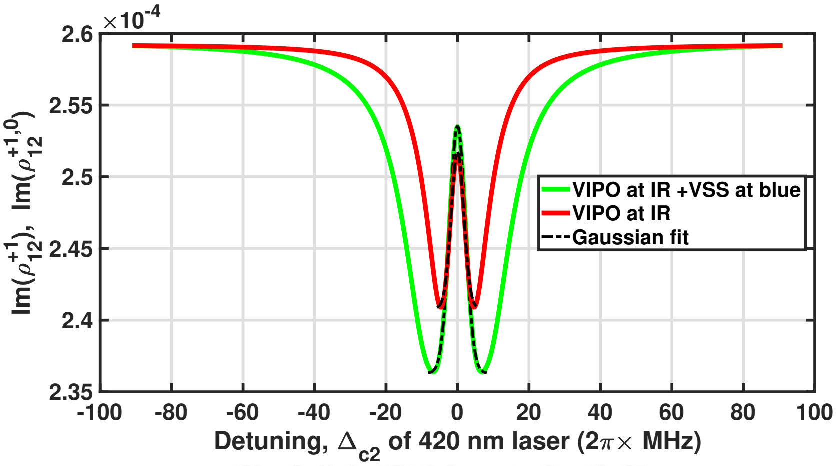

Fig. C.1: Numerically calculated thermal averaged probe absorption vs detuning of 420 nm pump laser for V-type closed system with VIPO dip at IR transition (red trace) and VIPO dip at IR plus VSS at blue transition (green trace). The linewidth of the dip due to the VIPO dip at IR transition is 4.2 MHz while the linewidth of the dip due to the VIPO dip at IR plus VSS at blue transition is 5.2 MHz. $\Omega_{c1} = \Gamma_2$, $\Omega_{c2} = \sqrt{1.5}\Gamma_3$, $\Gamma_2 = 2\pi \times 6.065$ MHz, $\Gamma_3 = 2\pi \times 1.32$ MHz.

C.2 VIPO at IR and VSS at blue transition for a V-type closed system

We consider a V-type closed system with VIPO at IR and VSS at blue transition. The dynamics of the atom-field interactions is obtained from Eq. 2.15 and 6.5 which gives the following set of equations of motion with time-dependent coefficients:

$$\begin{aligned}
\dot{\rho}_{12} =& \frac{i}{2}(\Omega_{\rm c1} + \Omega_{\rm p}e^{i\delta_1 t})(\rho_{11} - \rho_{22}) - \gamma_{12}\rho_{12} - \frac{i}{2}(\Omega_{\rm c2} + \Omega_{\rm c2}e^{i\delta_2 t})\rho_{32}, \qquad (C.3)\\
\dot{\rho}_{13} =& \frac{i}{2}(\Omega_{\rm c2} + \Omega_{\rm c2}e^{i\delta_2 t})(\rho_{11} - \rho_{33}) - \gamma_{13}\rho_{13} - \frac{i}{2}(\Omega_{\rm c1} + \Omega_{\rm p}e^{i\delta_1 t})\rho_{23},\\
\dot{\rho}_{22} =& \frac{i}{2}(\Omega_{\rm c1} + \Omega_{\rm p}e^{i\delta_1 t})\rho_{21} - \frac{i}{2}(\Omega_{\rm c1}^* + \Omega_{\rm p}^* e^{-i\delta_1 t})\rho_{12} - \Gamma_2\rho_{22},\\
\dot{\rho}_{23} =& -\frac{i}{2}(\Omega_{\rm c1}^* + \Omega_{\rm p}^* e^{-i\delta_1 t})\rho_{13} + \frac{i}{2}(\Omega_{\rm c2} + \Omega_{\rm c2}e^{i\delta_2 t})\rho_{21} - \gamma_{23}\rho_{23},\\
\dot{\rho}_{33} =& -\frac{i}{2}(\Omega_{\rm c2}^* + \Omega_{\rm c2}^* e^{-i\delta_2 t})\rho_{13} + \frac{i}{2}(\Omega_{\rm c2} + \Omega_{\rm c2}e^{i\delta_2 t})\rho_{31} - \Gamma_3\rho_{33}.
\end{aligned}$$

The absorption of the probe field is obtained by substituting the truncated series of the Floquet expansion given in Eq. 6.7 up to first-order into Eq. C.3. The coefficients of the same power in $n\delta_1$ and $m\delta_2$ are compared which gives a set of steady state equations of motion as follows:

$$\begin{aligned}
\dot{\rho}_{12}^{(n,m)} =& \frac{i\Omega_{\mathrm{c1}}}{2}(\rho_{11}^{(n,m)} - \rho_{22}^{(n,m)}) + \frac{i\Omega_{\mathrm{p}}}{2}(\rho_{11}^{(n-1,m)} - \rho_{22}^{(n-1,m)}) - \frac{i\Omega_{\mathrm{c2}}}{2}(\rho_{32}^{(n,m)} + \rho_{32}^{(n,m-1)}) \\
& - (\gamma_{12} + i(n\delta_1 + m\delta_2))\rho_{12}^{(n,m)}, \\
\dot{\rho}_{13}^{(n,m)} =& \frac{i\Omega_{\mathrm{c2}}}{2}(\rho_{11}^{(n,m)} - \rho_{33}^{(n,m)}) + \frac{i\Omega_{\mathrm{c2}}}{2}(\rho_{11}^{(n,m-1)} - \rho_{33}^{(n,m-1)}) - (\gamma_{13} + i(n\delta_1 + m\delta_2))\rho_{13}^{(n,m)} \\
& - \frac{i}{2}(\Omega_{\mathrm{c1}}\rho_{23}^{(n,m)} + \Omega_{\mathrm{p}}\rho_{23}^{(n-1,m)}), \\
\dot{\rho}_{21}^{(n,m)} =& \frac{i\Omega_{\mathrm{c1}}^*}{2}(\rho_{22}^{(n,m)} - \rho_{11}^{(n,m)}) + \frac{i\Omega_{\mathrm{p}}^*}{2}(\rho_{22}^{(n+1,m)} - \rho_{11}^{(n+1,m)}) + \frac{i\Omega_{\mathrm{c2}}^*}{2}(\rho_{23}^{(n,m)}\rho_{23}^{(n,m+1)}) \\
& - (\gamma_{21} + i(n\delta_1 + m\delta_2))\rho_{21}^{(n)}, \\
\dot{\rho}_{22}^{(n,m)} =& \frac{i}{2}(\Omega_{\mathrm{c1}}\rho_{21}^{(n,m)} + \Omega_{\mathrm{p}}\rho_{21}^{(n-1,m)}) - \frac{i}{2}(\Omega_{\mathrm{c1}}^*\rho_{12}^{(n,m)} + \Omega_{\mathrm{p}}^*\rho_{12}^{(n+1,m)}) - (\Gamma_2 + i(n\delta_1 + m\delta_2))\rho_{22}^{(n,m)}, \\
\dot{\rho}_{23}^{(n,m)} =& -\frac{i}{2}(\Omega_{\mathrm{c1}}^*\rho_{13}^{(n,m)} + \Omega_{\mathrm{p}}^*\rho_{13}^{(n+1,m)}) + \frac{i\Omega_{\mathrm{c2}}}{2}(\rho_{21}^{(n,m)} + \rho_{21}^{(n,m-1)}) - (\gamma_{23} + i(n\delta_1 + m\delta_2))\rho_{23}^{(n)}, \\
\dot{\rho}_{31}^{(n,m)} =& \frac{i\Omega_{\mathrm{c2}}^*}{2}(\rho_{33}^{(n,m)} - \rho_{11}^{(n,m)}) + \frac{i\Omega_{\mathrm{c2}}^*}{2}(\rho_{33}^{(n,m+1)} - \rho_{11}^{(n,m+1)}) - (\gamma_{31} + i(n\delta_1 + m\delta_2))\rho_{31}^{(n,m)} \\
& + \frac{i}{2}(\Omega_{\mathrm{c1}}^*\rho_{32}^{(n,m)} + \Omega_{\mathrm{p}}^*\rho_{32}^{(n+1,m)}), \\
\dot{\rho}_{32}^{(n,m)} =& \frac{i}{2}(\Omega_{\mathrm{c1}}\rho_{31}^{(n,m)} + \Omega_{\mathrm{p}}\rho_{31}^{(n-1,m)}) - \frac{i\Omega_{\mathrm{c2}}^*}{2}(\rho_{12}^{(n,m)} + \rho_{12}^{(n,m+1)}) - (\gamma_{32} + i(n\delta_1 + m\delta_2))\rho_{32}^{(n,m)}, \\
\dot{\rho}_{33}^{(n,m)} =& -\frac{i\Omega_{\mathrm{c2}}^*}{2}(\rho_{13}^{(n,m)} + \rho_{13}^{(n,m+1)}) + \frac{i\Omega_{\mathrm{c2}}}{2}(\rho_{31}^{(n,m)} + \rho_{31}^{(n,m-1)}) - (\Gamma_3 + i(n\delta_1 + m\delta_2))\rho_{33}^{(n,m)}.
\end{aligned} \tag{C.4}$$

The imaginary part of the density matrix element $\rho_{12}^{(+1,0)}$ is proportional to probe absorption and is shown by the green trace of Fig. C.1.

Appendix D

Analytical solution of VIPO at IR transition for optical pumping system

The steady state analytical solution of the density matrix elements $\rho_{11}^{(0)}$, $\rho_{22}^{(0)}$, $\rho_{11}^{(+1)}$ and $\rho_{22}^{(+1)}$ for a four-level optical pumping system given in Eq. 6.11 (see chapter 6) are as follows:

$$\rho_{11}^{(0)} = \frac{(\Gamma_2((\Gamma_2+\Pi_g)^2+4\Delta_{c1}^2)+\Omega_{c1}^2(\Gamma_2+\Pi_g))(\Omega_{c2}^2(\Gamma_3+\Pi_g)(\Gamma_{31}+\Pi_g)+\Gamma_3\Pi_g((\Gamma_3+\Pi_g)^2+4\Delta_{c2}^2))}{\begin{array}{l}2\Omega_{c2}^2(\Gamma_3+\Pi_g)(\frac{1}{2}\Gamma_2(\Gamma_{31}+3\Pi_g)((\Gamma_2+\Pi_g)^2+4\Delta_{c1}^2)+\Omega_{c1}^2(\Gamma_2+\Pi_g)(\Gamma_{31}+2\Pi_g))+\Gamma_3\Pi_g((\Gamma_3+\Pi_g)^2+4\Delta_{c2}^2)\\ (2\Gamma_2((\Gamma_2+\Pi_g)^2+4\Delta_{c1}^2)+3\Omega_{c1}^2(\Gamma_2+\Pi_g))\end{array}}, \tag{D.1}$$

$$\rho_{22}^{(0)} = \frac{\Omega_{c1}^2(\Gamma_2+\Pi_g)(\Omega_{c2}^2(\Gamma_3+\Pi_g)(\Gamma_{31}+\Pi_g)+\Gamma_3\Pi_g((\Gamma_3+\Pi_g)^2+4\Delta_{c2}^2))}{\begin{array}{l}2\Omega_{c2}^2(\Gamma_3+\Pi_g)(\frac{1}{2}\Gamma_2(\Gamma_{31}+3\Pi_g)((\Gamma_2+\Pi_g)^2+4\Delta_{c1}^2)+\Omega_{c1}^2(\Gamma_2+\Pi_g)(\Gamma_{31}+2\Pi_g))+\Gamma_3\Pi_g((\Gamma_3+\Pi_g)^2+4\Delta_{c2}^2)\\ (2\Gamma_2((\Gamma_2+\Pi_g)^2+4\Delta_{c1}^2)+3\Omega_{c1}^2(\Gamma_2+\Pi_g))\end{array}}, \tag{D.2}$$

$$\begin{aligned}\rho_{11}^{(+1)} = &\frac{\begin{array}{l}\Omega_{c1}\Omega_p(\Gamma_2+\Pi_g+i\delta_1)(\Gamma_2+\Pi_g+2i(\delta_1-\Delta_{c1}))\\[2ex] (\frac{i\Omega_{c2}^2(\Gamma_{31}-\Pi_g)(\rho_{11}^{(0)}-\rho_{22}^{(0)})(\Gamma_3+\Pi_g+2i\delta_1)(2\Delta_{c1}+i(\Gamma_2+\Pi_g+2i\delta_1))(\Gamma_2+\Pi_g+2i(\delta_1+\Delta_{c1}))}{((\Gamma_2+i\delta_1)(4\Delta_{c1}^2+(\Gamma_2+\Pi_g+2i\delta_1)^2)+\Omega_{c1}^2(\Gamma_2+\Pi_g+2i\delta_1))((\Gamma_3+i\delta_1)(4\Delta_{c2}^2+(\Gamma_3+\Pi_g+2i\delta_1)^2)+2\Omega_{c2}^2(\Gamma_3+\Pi_g+2i\delta_1))}\\ +\frac{(\rho_{11}^{(0)}-\rho_{22}^{(0)})((\Gamma_2-\Pi_g)(4\Delta_{c1}^2+(\Gamma_2+\Pi_g+2i\delta_1)^2)+\Omega_{c1}^2(\Gamma_2+\Pi_g+2i\delta_1))}{(\Gamma_2+i\delta_1)(4\Delta_{c1}^2+(\Gamma_2+\Pi_g+2i\delta_1)^2)+\Omega_{c1}^2(\Gamma_2+\Pi_g+2i\delta_1)}-(\rho_{11}^{(0)}-\rho_{22}^{(0)}))\end{array}}{\mathrm{A}(\Gamma_2+\Pi_g-2i\Delta_{c1})((2\Pi_g+i\delta_1)(\Gamma_2+\Pi_g+2i(\delta_1-\Delta_{c1}))(\Gamma_2+\Pi_g+2i(\delta_1+\Delta_{c1}))+\Omega_{c1}^2(\Gamma_2+\Pi g+2i\delta_1))},\\[2ex] &(-\frac{i\Omega_{c1}^2\Omega_{c2}^2(\Gamma_{31}-\Pi_g)(\Gamma_2+\Pi_g+2i\delta_1)(\Gamma_3+\Pi_g+2i\delta_1)(\Gamma_2+\Pi_g+2i(\delta_1-\Delta_{c1}))(\Gamma_2+\Pi_g+2i(\delta_1+\Delta_{c1}))}{\mathrm{B}(\delta_1-i\Gamma_3)(4\Delta_{c2}^2+(\Gamma_3+\Pi_g+2i\delta_1)^2)-2i\mathrm{B}\Omega_{c2}^2(\Gamma_3+\Pi_g+2i\delta_1)}\\ &-\frac{\Omega_{c1}^2(\Gamma_2+\Pi_g+2i\delta_1)((\Gamma_2-\Pi_g)(4\Delta_{c1}^2+(\Gamma_2+\Pi_g+2i\delta_1)^2)+\Omega_{c1}^2(\Gamma_2+\Pi_g+2i\delta_1))}{\mathrm{B}}+1)\end{aligned} \tag{D.3}$$

$$\rho_{22}^{(+1)} = -\frac{\Omega_{c1}(-\rho_{11}^{(+1)}\Omega_{c1}(\Gamma_2+\Pi_g+2i\delta_1)(\Gamma_2+\Pi_g-2i\Delta_{c1})-\Omega_p(\rho_{11}^{(0)}-\rho_{22}^{(0)})(\Gamma_2+\Pi_g+i\delta_1)(\Gamma_2+\Pi_g+2i(\delta_1-\Delta_{c1})))}{(\Gamma_2+\Pi_g-2i\Delta_{c1})((\Gamma_2+i\delta_1)(4\Delta_{c1}^2+(\Gamma_2+\Pi_g+2i\delta_1)^2)+\Omega_{c1}^2(\Gamma_2+\Pi_g+2i\delta_1))}, \quad \text{(D.4)}$$

where,

$$\begin{aligned}\mathrm{A} =&1+\frac{\Omega_{c2}^2(\Gamma_{31}-\Pi_g)(\Gamma_3+\Pi_g+2i\delta_1)(\Gamma_2+\Pi_g+2i(\delta_1-\Delta_{c1}))(\Gamma_2+\Pi_g+2i(\delta_1+\Delta_{c1}))}{((2\Pi_g+i\delta_1)(4\Delta_{c1}^2+(\Gamma_2+\Pi_g+2i\delta_1)^2)+\Omega_{c1}^2(\Gamma_2+\Pi_g+2i\delta_1))((\Gamma_3+i\delta_1)(4\Delta_{c2}^2+(\Gamma_3+\Pi_g+2i\delta_1)^2)+2\Omega_{c2}^2(\Gamma_3+\Pi_g+2i\delta_1))},\\ \mathrm{B} =&\mathrm{A}((\Gamma_2+i\delta_1)(4\Delta_{c1}^2+(\Gamma_2+\Pi_g+2i\delta_1)^2)+\Omega_{c1}^2(\Gamma_2+\Pi_g+2i\delta_1))((2\Pi_g+i\delta_1)(4\Delta_{c1}^2+(\Gamma_2+\Pi_g+2i\delta_1)^2)+\Omega_{c1}^2(\Gamma_2+\Pi_g+2i\delta_1)).\end{aligned}$$

Appendix E

Density matrix formulation for two-level system driven by pump and probe lasers

The density matrix component which corresponds to the absorption of a particular laser field, is identified when working in the Schrödinger picture. The Hamiltonian H_I in the RWA given in Eq. 2.7, is transformed into the Schrödinger picture under a unitary transformation $U_1^\dagger H_I U_1$. For a two-level system coupled with a probing laser, the Hamiltonian H_I in the RWA is:

$$H_I = \frac{\hbar}{2}\Big\{\Omega_p e^{i\delta_{12}^p t} \left|1\right\rangle \left\langle 2\right| + \Omega_p^* e^{-i\delta_{12}^p t} \left|2\right\rangle \left\langle 1\right| \Big\}, \tag{E.1}$$

and it transforms into the Schrödinger picture as,

$$H_I = \frac{\hbar}{2}\Big\{\Omega_p e^{i\omega_p t} \left|1\right\rangle \left\langle 2\right| + \Omega_p^* e^{-i\omega_p t} \left|2\right\rangle \left\langle 1\right| \Big\}, \tag{E.2}$$

under the unitary transformation $U_1^\dagger H_I U_1$. Where, $U_1 = e^{i\omega_1 t} \left|1\right\rangle \left\langle 1\right| + e^{i\omega_2 t} \left|2\right\rangle \left\langle 2\right|$ and $\delta_{12}^p = \omega_p - (\omega_2 - \omega_1)$ is the detuning of the probing laser from resonance on $\left|1\right\rangle \rightarrow \left|2\right\rangle$ transition. The equations of motion for the two-level system without the incoherent processes such as spontaneous decay rates is obtained by substituting Eq. E.2 into

Eq. 2.14 and is expressed as:

$$\begin{aligned}
\dot{\rho}_{11} =& \frac{i\Omega_p^*}{2} e^{-i\omega_p t}\rho_{12} - \frac{i\Omega_p}{2} e^{i\omega_p t}\rho_{21}, \\
\dot{\rho}_{12} =& \frac{i\Omega_p}{2} e^{i\omega_p t}\rho_{11} - \frac{i\Omega_p}{2} e^{i\omega_p t}\rho_{22}, \\
\dot{\rho}_{21} =& -\frac{i\Omega_p^*}{2} e^{-i\omega_p t}\rho_{11} + \frac{i\Omega_p^*}{2} e^{-i\omega_p t}\rho_{22}, \\
\dot{\rho}_{22} =& -\frac{i\Omega_p^*}{2} e^{-i\omega_p t}\rho_{12} + \frac{i\Omega_p}{2} e^{i\omega_p t}\rho_{21}.
\end{aligned} \tag{E.3}$$

From the equations of motion (Eq. E.3), the density matrix element $\dot{\rho}_{21}$ is oscillating at the frequency of the probing laser field $(\Omega_p^* e^{-\omega_p t})$. However, since $\rho_{21} = \rho_{12}^*$, the imaginary part of ρ_{12} is proportional to the absorption of the probing field.

For a two-level system coupled by two lasers (i.e., a strong pump and a weak probe laser fields), the Hamiltonian H_I in the RWA is given as:

$$H_I = \frac{\hbar}{2}\Big\{(\Omega_c + \Omega_p e^{i\delta t})e^{i\delta^c_{12}t}\,|1\rangle\langle 2| + (\Omega_c^* + \Omega_p^* e^{-i\delta t})e^{-i\delta^c_{12}t}\,|2\rangle\langle 1|\Big\}, \tag{E.4}$$

where, $\delta = \omega_p - \omega_c$ is the probe field detuning with respect to the pump field and $\delta^c_{12} = \omega_c - (\omega_2 - \omega_1)$ is the pump field detuning with the atomic resonance transition. The Hamiltonian H_I given in Eq. E.4 transforms into the Schrödinger picture under the unitary transformation $U_1^\dagger H_I U_1$ as,

$$H_I = \frac{\hbar}{2}\Big\{(\Omega_c + \Omega_p e^{i\delta t})e^{i\omega_c t}\,|1\rangle\langle 2| + (\Omega_c^* + \Omega_p^* e^{-i\delta t})e^{-i\omega_c t}\,|2\rangle\langle 1|\Big\}. \tag{E.5}$$

The equations of motion for the two-level system coupled with two lasers is also obtained by substituting Eq. E.5 into Eq. 2.14 and is expressed as:

$$\begin{aligned}
\dot{\rho}_{11} =& \frac{i}{2}(\Omega_c^* + \Omega_p^* e^{-i\delta t})e^{-i\omega_c t}\rho_{12} - \frac{i}{2}(\Omega_c + \Omega_p e^{i\omega_p t})e^{i\omega_c t}\rho_{21}, \\
\dot{\rho}_{12} =& \frac{i}{2}(\Omega_c + \Omega_p e^{i\delta t})e^{i\omega_c t}\rho_{11} - \frac{i}{2}(\Omega_c + \Omega_p e^{i\delta t})e^{i\omega_c t}\rho_{22}, \\
\dot{\rho}_{21} =& -\frac{i}{2}(\Omega_c^* + \Omega_p^* e^{-i\delta t})e^{-i\omega_c t}\rho_{11} + \frac{i}{2}(\Omega_c^* + \Omega_p^* e^{-i\delta t})e^{-i\omega_c t}\rho_{22}, \\
\dot{\rho}_{22} =& -\frac{i}{2}(\Omega_c^* + \Omega_p^* e^{-i\delta t})e^{-i\omega_c t}\rho_{12} + \frac{i}{2}(\Omega_c + \Omega_p e^{i\delta t})e^{i\omega_c t}\rho_{21}.
\end{aligned} \tag{E.6}$$

Treating the strong pump field Ω_c correctly to all orders and the weak probe field Ω_p to first order only in the above equations of motion, ρ_{21} oscillates at three dominant frequencies: ω_c, ω_p and $2\omega_c - \omega_p$. Using the Floquet expansion to first order in the probe field:

$$\rho_{ij}(t) = \rho_{ij}^{(\omega_c)}(t)e^{-i\omega_c t} + \rho_{ij}^{(\omega_p)}(t)e^{-i\omega_p t} + \rho_{ij}^{(2\omega_c-\omega_p)}(t)e^{-i(2\omega_c-\omega_p)t}, \tag{E.7}$$

$\rho_{21}^{(\omega_c)}$ oscillates at the frequency of the pump field Ω_c, $\rho_{21}^{(\omega_p)}$ oscillates at the frequency of the probe field Ω_p and $\rho_{21}^{(2\omega_c-\omega_p)}$ is for wave-mixing. In the rotating frame of the pump field, the above Floquet expansion (Eq. E.7) is of the form:

$$\rho_{ij}(t) = \rho_{ij}^{(0)}(t) + \rho_{ij}^{(\delta)}(t)e^{-i\delta t} + \rho_{ij}^{(-\delta)}(t)e^{i\delta t}, \tag{E.8}$$

which is also expressed as $\rho_{ij}(t) = \sum_{n=-\infty}^{\infty} \rho_{ij}^{(n\delta)}(t)e^{-in\delta t}$ for the infinity series, where $\delta = \omega_p - \omega_c$. The Floquet expansion in Eq. E.8 is obtained from Eq. E.7 by subtracting the index of ρ_{ij} with ω_c and then multiply with $e^{i\omega_c t}$. Since $\rho_{21} = \rho_{12}^*$, the imaginary part of $\rho_{12}^{(0)}$, $\rho_{12}^{(+1)}$ and $\rho_{12}^{(-1)}$ is proportional to the absorption of the strong pump field, the weak probe field and wave-mixing response respectively.

Bibliography

[1] Kasapi, A., Jain, M., Yin, G. Y. & Harris, S. E. Electromagnetically induced transparency: Propagation dynamics. Phys. Rev. Lett. **74**, 2447–2450 (1995). URL `https://link.aps.org/doi/10.1103/PhysRevLett.74.2447`.

[2] Hau, L. V., Harris, S. E., Dutton, Z. & Behroozi, C. H. Light speed reduction to 17 metres per second in an ultracold atomic gas. Nature **397**, 594–598 (1999).

[3] Phillips, D. F., Fleischhauer, A., Mair, A., Walsworth, R. L. & Lukin, M. D. Storage of light in atomic vapor. Phys. Rev. Lett. **86**, 783–786 (2001). URL `https://link.aps.org/doi/10.1103/PhysRevLett.86.783`.

[4] Turukhin, A. V. et al. Observation of ultraslow and stored light pulses in a solid. Phys. Rev. Lett. **88**, 023602 (2001). URL `https://link.aps.org/doi/10.1103/PhysRevLett.88.023602`.

[5] Vudyasetu, P. K., Camacho, R. M. & Howell, J. C. Storage and retrieval of multimode transverse images in hot atomic rubidium vapor. Phys. Rev. Lett. **100**, 123903 (2008). URL `https://link.aps.org/doi/10.1103/PhysRevLett.100.123903`.

[6] Shuker, M., Firstenberg, O., Pugatch, R., Ron, A. & Davidson, N. Storing images in warm atomic vapor. Phys. Rev. Lett. **100**, 223601 (2008). URL `https://link.aps.org/doi/10.1103/PhysRevLett.100.223601`.

[7] Eilam, A., Azuri, I., Sharypov, A. V., Wilson-Gordon, A. D. & Friedmann, H. Spatial optical memory based on coherent population oscillations. Opt. Lett. **35**, 772–774 (2010). URL `http://ol.osa.org/abstract.cfm?URI=ol-35-5-772`.

[8] Hemmer, P. R. et al. Semiconductor laser excitation of Ramsey fringes by using a Raman transition in a cesium atomic beam. J. Opt. Soc. Am. B **10**, 1326–1329 (1993). URL `http://josab.osa.org/abstract.cfm?URI=josab-10-8-1326`.

[9] Esnault, F.-X. et al. Cold-atom double-Λ coherent population trapping clock. Phys. Rev. A **88**, 042120 (2013). URL `https://link.aps.org/doi/10.1103/PhysRevA.88.042120`.

[10] He, P., Tengdin, P. M., Anderson, D. Z., Rey, A. M. & Holland, M. Sub-Doppler laser cooling using electromagnetically induced transparency. Phys. Rev. A **95**, 053403 (2017). URL `https://link.aps.org/doi/10.1103/PhysRevA.95.053403`.

[11] Li, Y.-q. & Xiao, M. Observation of quantum interference between dressed states in an electromagnetically induced transparency. Phys. Rev. A **51**, 4959–4962 (1995). URL `https://link.aps.org/doi/10.1103/PhysRevA.51.4959`.

[12] Agarwal, G. S. Nature of the quantum interference in electromagnetic-field-induced control of absorption. Phys. Rev. A **55**, 2467–2470 (1997). URL `https://link.aps.org/doi/10.1103/PhysRevA.55.2467`.

[13] Khan, S., Bharti, V. & Natarajan, V. Role of dressed-state interference in electromagnetically induced transparency. Physics Letters A **380**, 4100 – 4104 (2016). URL `http://www.sciencedirect.com/science/article/pii/S0375960116313433`.

[14] Arimondo, E. V coherent population trapping in laser spectroscopy. vol. 35 of Progress in Optics, 257 – 354 (Elsevier, 1996). URL http://www.sciencedirect.com/science/article/pii/S0079663808705316.

[15] Boller, K.-J., Imamoğlu, A. & Harris, S. E. Observation of electromagnetically induced transparency. Phys. Rev. Lett. **66**, 2593–2596 (1991). URL https://link.aps.org/doi/10.1103/PhysRevLett.66.2593.

[16] Lezama, A., Barreiro, S. & Akulshin, A. M. Electromagnetically induced absorption. Phys. Rev. A **59**, 4732–4735 (1999). URL https://link.aps.org/doi/10.1103/PhysRevA.59.4732.

[17] Harris, S. E. Lasers without inversion: Interference of lifetime-broadened resonances. Phys. Rev. Lett. **62**, 1033–1036 (1989). URL https://link.aps.org/doi/10.1103/PhysRevLett.62.1033.

[18] Imamoğlu, A. & Harris, S. E. Lasers without inversion: interference of dressed lifetime-broadened states. Opt. Lett. **14**, 1344–1346 (1989). URL http://ol.osa.org/abstract.cfm?URI=ol-14-24-1344.

[19] Cohen-tannoudji, C. & Guèry-odelin, D. Advances in atomic physics: an overview (World Scientific, 2011).

[20] Imamogˇlu, A. Interference of radiatively broadened resonances. Phys. Rev. A **40**, 2835–2838 (1989). URL https://link.aps.org/doi/10.1103/PhysRevA.40.2835.

[21] Glaser, C. et al. Absolute frequency measurement of rubidium $5S$–$6P$ transitions. Phys. Rev. A **102**, 012804 (2020). URL https://link.aps.org/doi/10.1103/PhysRevA.102.012804.

[22] Nyakang'o, E. O., Shylla, D., Natarajan, V. & Pandey, K. Hyperfine measurement of the $6P_{1/2}$ state in ^{87}Rb using double resonance on blue and IR transition. Journal of Physics B: Atomic, Molecular and Optical Physics **53**, 095001 (2020). URL https://doi.org/10.1088%2F1361-6455%2Fab7670.

[23] Menon, S. & Agarwal, G. S. Gain components in the Autler-Townes doublet from quantum interferences in decay channels. Phys. Rev. A **61**, 013807 (1999). URL `https://link.aps.org/doi/10.1103/PhysRevA.61.013807`.

[24] Krishna, A., Pandey, K., Wasan, A. & Natarajan, V. High-resolution hyperfine spectroscopy of excited states using electromagnetically induced transparency. EPL (Europhysics Letters) **72**, 221–227 (2005). URL `http://stacks.iop.org/0295-5075/72/221`.

[25] Boyd, R. W., Raymer, M. G., Narum, P. & Harter, D. J. Four-wave parametric interactions in a strongly driven two-level system. Phys. Rev. A **24**, 411–423 (1981). URL `https://link.aps.org/doi/10.1103/PhysRevA.24.411`.

[26] She, C. Y. & Yu, J. R. Doppler-free saturation fluorescence spectroscopy of na atoms for atmospheric application. Appl. Opt. **34**, 1063–1075 (1995). URL `http://ao.osa.org/abstract.cfm?URI=ao-34-6-1063`.

[27] Nyakang'o, Elijah Ogaro & Pandey, Kanhaiya. Role of velocity induced coherent population oscillation in saturated fluorescence spectroscopy. Eur. Phys. J. D **74**, 96 (2020). URL `https://doi.org/10.1140/epjd/e2020-100519-0`.

[28] Im, K.-B. et al. Saturated absorption signals for the Cs D_2 line. Phys. Rev. A **63**, 034501 (2001). URL `https://link.aps.org/doi/10.1103/PhysRevA.63.034501`.

[29] Hänsch, T. W., Levenson, M. D. & Schawlow, A. L. Complete hyperfine structure of a molecular iodine line. Phys. Rev. Lett. **26**, 946–949 (1971). URL `https://link.aps.org/doi/10.1103/PhysRevLett.26.946`.

[30] Yang, T. et al. A high flux source of cold strontium atoms. The European Physical Journal D **69**, 226 (2015). URL `https://doi.org/10.1140/epjd/e2015-60288-y`.

[31] Marsman, A., Hessels, E. A. & Horbatsch, M. Shifts due to quantum-mechanical interference from distant neighboring resonances for saturated fluorescence spectroscopy of the $2\,^3S$ to $2\,^3P$ intervals of helium. Phys. Rev. A **89**, 043403 (2014). URL https://link.aps.org/doi/10.1103/PhysRevA.89.043403.

[32] Courtillot, I. et al. Accurate spectroscopy of Sr atoms. Eur. Phys. J. D **33**, 161–171 (2005). URL https://doi.org/10.1140/epjd/e2005-00058-0.

[33] Chan, E. A., Aljunid, S. A., Zheludev, N. I., Wilkowski, D. & Ducloy, M. Doppler-free approach to optical pumping dynamics in the $6S_{1/2} \rightarrow 5D_{5/2}$ electric quadrupole transition of cesium vapor. Opt. Lett. **41**, 2005–2008 (2016). URL http://ol.osa.org/abstract.cfm?URI=ol-41-9-2005.

[34] Li-Guo, Z., Zhong-Zheng, L., Zhi-Ming, T., Li, L. & Jing-Biao, C. Velocity transfer spectroscopy of Rb 420 nm transition. Chinese Physics Letters **31**, 083101 (2014). URL http://stacks.iop.org/0256-307X/31/i=8/a=083101.

[35] Pustelny, S. et al. Nonlinear magneto-optical rotation in rubidium vapor excited with blue light. Phys. Rev. A **92**, 053410 (2015). URL https://link.aps.org/doi/10.1103/PhysRevA.92.053410.

[36] Ye, J., Swartz, S., Jungner, P. & Hall, J. L. Hyperfine structure and absolute frequency of the ^{87}Rb $5P_{3/2}$ state. Opt. Lett. **21**, 1280–1282 (1996). URL http://ol.osa.org/abstract.cfm?URI=ol-21-16-1280.

[37] Marian, A., Stowe, M. C., Felinto, D. & Ye, J. Direct frequency comb measurements of absolute optical frequencies and population transfer dynamics. Phys. Rev. Lett. **95**, 023001 (2005). URL https://link.aps.org/doi/10.1103/PhysRevLett.95.023001.

[38] Banerjee, A. & Natarajan, V. Absolute-frequency measurements of the D_2 line and fine-structure interval in ^{39}K. Phys. Rev. A **70**, 052505 (2004). URL https://link.aps.org/doi/10.1103/PhysRevA.70.052505.

[39] Touahri, D. et al. Frequency measurement of the $5S_{1/2}(F = 3)\rightarrow 5D_{5/2}(F = 5)$ two-photon transition in rubidium. Optics Communications **133**, 471 – 478 (1997). URL `http://www.sciencedirect.com/science/article/pii/S0030401896004713`.

[40] Morzyński, P. et al. Absolute frequency measurement of rubidium 5S→7S two-photon transitions. Opt. Lett. **38**, 4581–4584 (2013). URL `http://ol.osa.org/abstract.cfm?URI=ol-38-22-4581`.

[41] Chui, H.-C. et al. Absolute frequency measurement of rubidium 5S→7S two-photon transitions with a femtosecond laser comb. Opt. Lett. **30**, 842–844 (2005). URL `http://ol.osa.org/abstract.cfm?URI=ol-30-8-842`.

[42] Wieman, C., Flowers, G. & Gilbert, S. Inexpensive laser cooling and trapping experiment for undergraduate laboratories. American Journal of Physics **63**, 317–330 (1995). URL `https://doi.org/10.1119/1.18072`. `https://doi.org/10.1119/1.18072`.

[43] Tiwari, V. B., Singh, S., Rawat, H. S. & Mehendale, S. C. Cooling and trapping of ^{85}Rb atoms in the ground hyperfine $F = 2$ state. Phys. Rev. A **78**, 063421 (2008). URL `https://link.aps.org/doi/10.1103/PhysRevA.78.063421`.

[44] Gomez, E., Aubin, S., Orozco, L. A. & Sprouse, G. D. Lifetime and hyperfine splitting measurements on the 7S and 6P levels in rubidium. J. Opt. Soc. Am. B **21**, 2058–2067 (2004). URL `http://josab.osa.org/abstract.cfm?URI=josab-21-11-2058`.

[45] McKay, D. C. et al. Low-temperature high-density magneto-optical trapping of potassium using the open 4S→5P transition at 405 nm. Phys. Rev. A **84**, 063420 (2011). URL `https://link.aps.org/doi/10.1103/PhysRevA.84.063420`.

[46] Duarte, P. M. et al. All-optical production of a lithium quantum gas using narrow-line laser cooling. Phys. Rev. A **84**, 061406 (2011). URL `https://link.aps.org/doi/10.1103/PhysRevA.84.061406`.

[47] Lee, W.-K. & Moon, H. S. Measurement of absolute frequencies and hyperfine structure constants of $4D_{5/2}$ and $4D_{3/2}$ levels of ^{87}Rb and ^{85}Rb using an optical frequency comb. Phys. Rev. A **92**, 012501 (2015). URL `https://link.aps.org/doi/10.1103/PhysRevA.92.012501`.

[48] Saffman, M., Walker, T. G. & Mølmer, K. Quantum information with Rydberg atoms. Rev. Mod. Phys. **82**, 2313–2363 (2010). URL `https://link.aps.org/doi/10.1103/RevModPhys.82.2313`.

[49] Mack, M. et al. Measurement of absolute transition frequencies of ^{87}Rb to nS and nD Rydberg states by means of electromagnetically induced transparency. Phys. Rev. A **83**, 052515 (2011). URL `https://link.aps.org/doi/10.1103/PhysRevA.83.052515`.

[50] Simonelli, C. et al. Deexcitation spectroscopy of strongly interacting Rydberg gases. Phys. Rev. A **96**, 043411 (2017). URL `https://link.aps.org/doi/10.1103/PhysRevA.96.043411`.

[51] Safronova, M. S., Williams, C. J. & Clark, C. W. Relativistic many-body calculations of electric-dipole matrix elements, lifetimes, and polarizabilities in rubidium. Phys. Rev. A **69**, 022509 (2004). URL `https://link.aps.org/doi/10.1103/PhysRevA.69.022509`.

[52] Zhang, S.-N. et al. A 420 nm blue diode laser for the potential rubidium optical frequency standard. Chinese Physics Letters **34**, 074211 (2017). URL `https://doi.org/10.1088%2F0256-307x%2F34%2F7%2F074211`.

[53] Zhang, S., Chang, P., Shang, H. & Chen, J. Development of ultra-stable Rb-referenced 420nm optical frequency standard. In

2018 IEEE International Frequency Control Symposium (IFCS), 1–4 (IEEE, 2018).

[54] Navarro-Navarrete, J. et al. Doppler-free saturation of the cascade fluorescence that follows excitation of the 5S→6P transition in atomic rubidium. arXiv preprint arXiv:1906.07114 (2019).

[55] Feiertag, D. & Zu Putlitz, G. Hyperfine structure, g j factors and lifetimes of excited $^2P_{1/2}$ states of Rb. Zeitschrift für Physik A Hadrons and nuclei **261**, 1–12 (1973).

[56] Xia, W. et al. Precision frequency measurement of ^{87}Rb 5S1/2(F= 2)→5D5/2(F′= 4) two-photon transition through a fiber-based optical frequency comb. Chinese Physics Letters **33**, 053201 (2016). URL https://doi.org/10.1088%2F0256-307x%2F33%2F5%2F053201.

[57] Boon, J. R., Zekou, E., Fulton, D. J. & Dunn, M. H. Experimental observation of a coherently induced transparency on a blue probe in a Doppler-broadened mismatched V-type system. Phys. Rev. A **57**, 1323–1328 (1998). URL https://link.aps.org/doi/10.1103/PhysRevA.57.1323.

[58] Ponciano-Ojeda, F. et al. Optical spectroscopy of the $5P_{3/2}$ →$6P_{1/2}$ electric dipole-forbidden transition in atomic rubidium. Journal of Physics B: Atomic, Molecular and Optical Physics **52**, 135001 (2019). URL https://doi.org/10.1088%2F1361-6455%2Fab1b94.

[59] Das, D. & Natarajan, V. Precise measurement of hyperfine structure in the $6P_{1/2}$ state of ^{133}Cs. Journal of Physics B: Atomic, Molecular and Optical Physics **39**, 2013 (2006). URL http://stacks.iop.org/0953-4075/39/i=8/a=018.

[60] Das, D., Pandey, K., Wasan, A. & Natarajan, V. Resolving closely spaced hyperfine levels in the $3P_{3/2}$ state of ^{23}Na.

Journal of Physics B: Atomic, Molecular and Optical Physics **39**, 3111 (2006). URL http://stacks.iop.org/0953-4075/39/i=14/a=017.

[61] Gea-Banacloche, J., Li, Y.-q., Jin, S.-z. & Xiao, M. Electromagnetically induced transparency in ladder-type inhomogeneously broadened media: Theory and experiment. Phys. Rev. A **51**, 576–584 (1995). URL https://link.aps.org/doi/10.1103/PhysRevA.51.576.

[62] Shepherd, S., Fulton, D. J. & Dunn, M. H. Wavelength dependence of coherently induced transparency in a Doppler-broadened cascade medium. Phys. Rev. A **54**, 5394–5399 (1996). URL https://link.aps.org/doi/10.1103/PhysRevA.54.5394.

[63] Mohapatra, A. K., Jackson, T. R. & Adams, C. S. Coherent optical detection of highly excited Rydberg states using electromagnetically induced transparency. Phys. Rev. Lett. **98**, 113003 (2007). URL http://link.aps.org/doi/10.1103/PhysRevLett.98.113003.

[64] Baldit, E., Bencheikh, K., Monnier, P., Levenson, J. A. & Rouget, V. Ultraslow light propagation in an inhomogeneously broadened rare-earth ion-doped crystal. Phys. Rev. Lett. **95**, 143601 (2005). URL https://link.aps.org/doi/10.1103/PhysRevLett.95.143601.

[65] Boyd, R. W. Slow and fast light: fundamentals and applications. Journal of Modern Optics **56**, 1908–1915 (2009). URL https://doi.org/10.1080/09500340903159495. https://doi.org/10.1080/09500340903159495.

[66] Piredda, G. & Boyd, R. Slow light by means of coherent population oscillations: laser linewidth effects. Journal of the European Optical Society - Rapid publications **2** (2007). URL http://www.jeos.org/index.php/jeos_rp/article/view/07004.

[67] Zapasskiĭ, V. S. & Kozlov, G. G. A saturable absorber, coherent population oscillations, and slow light. Optics and Spectroscopy **100**, 419–424 (2006). URL https://doi.org/10.1134/S0030400X06030192.

[68] Bigelow, M. S., Lepeshkin, N. N. & Boyd, R. W. Observation of ultraslow light propagation in a ruby crystal at room temperature. Phys. Rev. Lett. **90**, 113903 (2003). URL https://link.aps.org/doi/10.1103/PhysRevLett.90.113903.

[69] Kumar, P., Singh, A. K., Bharti, V., Natarajan, V. & Pandey, K. Study of CPO resonances on the intercombination line in ^{173}Yb. Journal of Physics B: Atomic, Molecular and Optical Physics **51**, 035502 (2018). URL http://stacks.iop.org/0953-4075/51/i=3/a=035502.

[70] Mrozek, M. et al. Coherent population oscillations with nitrogen-vacancy color centers in diamond. Phys. Rev. B **94**, 035204 (2016). URL https://link.aps.org/doi/10.1103/PhysRevB.94.035204.

[71] Hillman, L. W., Boyd, R. W., Krasinski, J. & Stroud, C. Observation of a spectral hole due to population oscillations in a homogeneously broadened optical absorption line. Optics Communications **45**, 416 – 419 (1983). URL http://www.sciencedirect.com/science/article/pii/0030401883903036.

[72] Ficek, Z. & Swain, S. Quantum interference and coherence: theory and experiments, vol. 100 (Springer Science & Business Media, 2005).

[73] Arimondo, E., Inguscio, M. & Violino, P. Experimental determinations of the hyperfine structure in the alkali atoms. Rev. Mod. Phys. **49**, 31–75 (1977). URL https://link.aps.org/doi/10.1103/RevModPhys.49.31.

[74] Jin, W. G. et al. Laser-rf double-resonance spectroscopy of ^{177,179}Hf.

Phys. Rev. A **52**, 157–164 (1995). URL https://link.aps.org/doi/10.1103/PhysRevA.52.157.

[75] Lewty, N. C., Chuah, B. L., Cazan, R., Sahoo, B. K. & Barrett, M. D. Spectroscopy on a single trapped ^{137}Ba^{+} ion for nuclear magnetic octupole moment determination. Opt. Express **20**, 21379–21384 (2012). URL http://www.opticsexpress.org/abstract.cfm?URI=oe-20-19-21379.

[76] Morris, J. R. & Shore, B. W. Reduction of degenerate two-level excitation to independent two-state systems. Phys. Rev. A **27**, 906–912 (1983). URL https://link.aps.org/doi/10.1103/PhysRevA.27.906.

[77] Pandey, K. Role of different types of subsystems in a doubly driven Λ system in ^{87}Rb. Phys. Rev. A **87**, 043838 (2013). URL http://link.aps.org/doi/10.1103/PhysRevA.87.043838.

[78] Li, Y.-q. & Xiao, M. Observation of quantum interference between dressed states in an electromagnetically induced transparency. Phys. Rev. A **51**, 4959–4962 (1995). URL https://link.aps.org/doi/10.1103/PhysRevA.51.4959.

[79] Fleischhauer, M., Imamoglu, A. & Marangos, J. P. Electromagnetically induced transparency: Optics in coherent media. Rev. Mod. Phys. **77**, 633–673 (2005). URL https://link.aps.org/doi/10.1103/RevModPhys.77.633.

[80] Shepherd, S., Fulton, D. J. & Dunn, M. H. Wavelength dependence of coherently induced transparency in a Doppler-broadened cascade medium. Phys. Rev. A **54**, 5394–5399 (1996). URL https://link.aps.org/doi/10.1103/PhysRevA.54.5394.

[81] Agarwal, G. S. Nature of the quantum interference in electromagnetic field induced control of absorption. Phys. Rev. A **55**, 2467–2470 (1997). URL https://link.aps.org/doi/10.1103/PhysRevA.55.2467.

[82] Abi-Salloum, T. Y. Electromagnetically induced transparency and Autler-Townes splitting: Two similar but distinct phenomena in two categories of three-level atomic systems. Phys. Rev. A **81**, 053836 (2010). URL `https://link.aps.org/doi/10.1103/PhysRevA.81.053836`.

[83] Tan, C. & Huang, G. Crossover from electromagnetically induced transparency to Autler-Townes splitting in open ladder systems with Doppler broadening. J. Opt. Soc. Am. B **31**, 704–715 (2014). URL `http://josab.osa.org/abstract.cfm?URI=josab-31-4-704`.

[84] Bason, M. G., Mohapatra, A. K., Weatherill, K. J. & Adams, C. S. Narrow absorptive resonances in a four-level atomic system. Journal of Physics B: Atomic, Molecular and Optical Physics **42**, 075503 (5pp) (2009). URL `http://stacks.iop.org/0953-4075/42/075503`.

[85] Chen, Y., Wei, X. G. & Ham, B. S. Optical properties of an N-type system in Doppler-broadened multilevel atomic media of the rubidium D_2 line. Journal of Physics B: Atomic, Molecular and Optical Physics **42**, 065506 (2009). URL `http://stacks.iop.org/0953-4075/42/i=6/a=065506`.

[86] Sheng, J., Yang, X., Khadka, U. & Xiao, M. All-optical switching in an N-type four-level atom-cavity system. Opt. Express **19**, 17059–17064 (2011). URL `http://www.opticsexpress.org/abstract.cfm?URI=oe-19-18-17059`.

[87] Hong, T., Cramer, C., Nagourney, W. & Fortson, E. N. Optical clocks based on ultranarrow three-photon resonances in alkaline earth atoms. Phys. Rev. Lett. **94**, 050801 (2005).

[88] Sedlacek, J. A. et al. Microwave electrometry with Rydberg atoms in a vapour cell using bright atomic resonances. Nature physics **8**, 819 (2012). URL `http://link.aps.org/doi/10.1103/PhysRevLett.111.063001`.

[89] Zhang, B. et al. Coherence generation and population transfer by stimulated Raman adiabatic passage and π pulse in a four-level ladder system. Opt. Express **19**, 12000–12007 (2011). URL http://www.opticsexpress.org/abstract.cfm?URI=oe-19-13-12000.

[90] Ghosh, A. et al. A study on electromagnetically induced transparency and velocity selective optically pumped absorption in an eight-level inverted Y-type atomic system. Journal of Physics B: Atomic, Molecular and Optical Physics **51**, 145501 (2018). URL https://doi.org/10.1088%2F1361-6455%2Faac6f5.

[91] Kumar, S., Lauprêtre, T., Bretenaker, F., Goldfarb, F. & Ghosh, R. Polarization-dependent manipulation of optical properties in a tripod system. Phys. Rev. A **88**, 023852 (2013). URL http://link.aps.org/doi/10.1103/PhysRevA.88.023852.

[92] Leroux, F. et al. Non-Abelian adiabatic geometric transformations in a cold strontium gas. Nature Communications **9**, 3580 (2018). URL https://doi.org/10.1038/s41467-018-05865-3.

[93] Hu, Y.-X., Miniatura, C., Wilkowski, D. & Grémaud, B. U(3) artificial gauge fields for cold atoms. Phys. Rev. A **90**, 023601 (2014). URL http://link.aps.org/doi/10.1103/PhysRevA.90.023601.

[94] Pandey, K., Kwong, C. C., Pramod, M. S. & Wilkowski, D. Linear and nonlinear magneto-optical rotation on the narrow strontium intercombination line. Phys. Rev. A **93**, 053428 (2016). URL http://link.aps.org/doi/10.1103/PhysRevA.93.053428.

[95] Mallick, N. S., Dey, T. N. & Pandey, K. Microwave assisted transparency in an M-system. Journal of Physics B: Atomic, Molecular and Optical Physics **50**, 195502 (2017). URL https://doi.org/10.1088%2F1361-6455%2Faa8a35.

[96] Shylla, D., Ogaro, E. N. & Pandey, K. Highly sensitive atomic based MW interferometry. Scientific Reports **8**, 8692 (2018). URL https://doi.org/10.1038/s41598-018-27011-1.

[97] Shylla, D. & Pandey, K. Single reference atomic based MW interferometry using eit. arXiv:1802.09935 (2018). URL https://arxiv.org/abs/1802.09935.

[98] Simons, M. T. et al. Electromagnetically induced transparency (EIT) and Autler-Townes (AT) splitting in the presence of band-limited white Gaussian noise. Journal of Applied Physics **123**, 203105 (2018). URL https://doi.org/10.1063/1.5020173. https://doi.org/10.1063/1.5020173.

[99] Volz, U. & Schmoranzer, H. Precision lifetime measurements on alkali atoms and on helium by beam–gas–laser spectroscopy. Physica Scripta **T65**, 48–56 (1996). URL https://doi.org/10.1088%2F0031-8949%2F1996%2Ft65%2F007.

[100] Caliebe, E. & Niemax, K. Oscillator strengths of the principal series lines of Rb. Journal of Physics B: Atomic and Molecular Physics **12**, L45 (1979). URL http://stacks.iop.org/0022-3700/12/i=2/a=003.

[101] Migdalek, J. & Kim, Y.-K. Core polarization and oscillator strength ratio anomaly in potassium, rubidium and caesium. Journal of Physics B: Atomic, Molecular and Optical Physics **31**, 1947 (1998). URL http://stacks.iop.org/0953-4075/31/i=9/a=011.

[102] Theodosiou, C. E. Lifetimes of alkali-metal atom Rydberg states. Phys. Rev. A **30**, 2881–2909 (1984). URL https://link.aps.org/doi/10.1103/PhysRevA.30.2881.

[103] Das, D. & Natarajan, V. Hyperfine spectroscopy on the $6P_{3/2}$ state of ^{133}Cs using coherent control. EPL (Europhysics Letters) **72**, 740 (2005). URL http://stacks.iop.org/0295-5075/72/i=5/a=740.

[104] Feld, M. S., Burns, M. M., Kühl, T. U., Pappas, P. G. & Murnick, D. E. Laser-saturation spectroscopy with optical pumping. Opt. Lett. **5**, 79–81 (1980). URL `http://ol.osa.org/abstract.cfm?URI=ol-5-2-79`.

[105] Smith, D. A. & Hughes, I. G. The role of hyperfine pumping in multilevel systems exhibiting saturated absorption. American Journal of Physics **72**, 631–637 (2004). URL `https://doi.org/10.1119/1.1652039`. `https://doi.org/10.1119/1.1652039`.

[106] Noh, H. R. Effect of optical pumping in saturated absorption spectroscopy: an analytic study for two-level atoms. European Journal of Physics **30**, 1181 (2009). URL `http://stacks.iop.org/0143-0807/30/i=5/a=025`.

[107] Sautenkov, V. et al. Using phase dynamics in EIT to probe ground state relaxation in rubidium vapor. Journal of Modern Optics **56**, 975–979 (2009). URL `https://doi.org/10.1080/09500340902836275`. `https://doi.org/10.1080/09500340902836275`.

[108] Fulton, D. J., Shepherd, S., Moseley, R. R., Sinclair, B. D. & Dunn, M. H. Continuous-wave electromagnetically induced transparency: A comparison of V, Λ, and cascade systems. Phys. Rev. A **52**, 2302–2311 (1995). URL `https://link.aps.org/doi/10.1103/PhysRevA.52.2302`.

[109] Manjappa, M., Undurti, S. S., Karigowda, A., Narayanan, A. & Sanders, B. C. Effects of temperature and ground-state coherence decay on enhancement and amplification in a Δ atomic system. Phys. Rev. A **90**, 043859 (2014). URL `https://link.aps.org/doi/10.1103/PhysRevA.90.043859`.

[110] Tiwari, V. B., Singh, S., Rawat, H. S., Singh, M. P. & Mehendale, S. C. Electromagnetically induced transparency in cold ^{85}Rb atoms trapped in the ground hyperfine F= 2 state. Journal of Physics B: Atomic, Molecular and Optical Physics **43**, 095503 (2010). URL `https://doi.org/10.1088%2F0953-4075%2F43%2F9%2F095503`.

[111] Donley, E. A., Heavner, T. P., Levi, F., Tataw, M. O. & Jefferts, S. R. Double-pass acousto-optic modulator system. Review of Scientific Instruments **76**, 063112 (2005). URL https://doi.org/10.1063/1.1930095. https://doi.org/10.1063/1.1930095.

[112] Urvoy, A. et al. Optical coherences and wavelength mismatch in ladder systems. Journal of Physics B: Atomic, Molecular and Optical Physics **46**, 245001 (2013). URL https://doi.org/10.1088%2F0953-4075%2F46%2F24%2F245001.

[113] Hughes, I. & Hase, T. Measurements and their uncertainties (Oxford University Press, 2010).

[114] Grundevik, P., Gustavsson, M., Rosén, A. & Svanberg, S. High resolution laser fluorescence spectroscopy in the deep blue spectral region. Zeitschrift für Physik A Atoms and Nuclei **283**, 127–132 (1977). URL https://doi.org/10.1007/BF01418703.

[115] Beloy, K. et al. Determination of the $5d6s$ $^3D_1$ state lifetime and blackbody-radiation clock shift in Yb. Phys. Rev. A **86**, 051404 (2012). URL https://link.aps.org/doi/10.1103/PhysRevA.86.051404.

[116] Demtroder, W. Laser Spectroscopy (Springer, 1998).

[117] Gutterres, R. F. et al. Determination of the ^{87}Rb $5p$ state dipole matrix element and radiative lifetime from the photoassociation spectroscopy of the Rb$_2$ $0_g^-(P_{3/2})$ long-range state. Phys. Rev. A **66**, 024502 (2002). URL https://link.aps.org/doi/10.1103/PhysRevA.66.024502.

[118] Safronova, M. S. & Safronova, U. I. Critically evaluated theoretical energies, lifetimes, hyperfine constants, and multipole polarizabilities in ^{87}Rb. Phys. Rev. A **83**, 052508 (2011). URL https://link.aps.org/doi/10.1103/PhysRevA.83.052508.

[119] Vdović, S., Ban, T., Aumiler, D. & Pichler, G. EIT at $5^2S_{1/2} \rightarrow 6^2P_{3/2}$ transition in a mismatched V-type rubidium system. Optics Communications **272**, 407 – 413 (2007). URL `http://www.sciencedirect.com/science/article/pii/S0030401806013101`.

[120] Shirley, J. H. Solution of the Schrödinger equation with a Hamiltonian periodic in time. Phys. Rev. **138**, B979–B987 (1965). URL `https://link.aps.org/doi/10.1103/PhysRev.138.B979`.

[121] Giovannini, U. D. & Hübener, H. Floquet analysis of excitations in materials. Journal of Physics: Materials **3**, 012001 (2019). URL `https://doi.org/10.1088%2F2515-7639%2Fab387b`.

[122] Noh, H.-R. & Moon, H. S. Transmittance signal in real ladder-type atoms. Phys. Rev. A **85**, 033817 (2012). URL `https://link.aps.org/doi/10.1103/PhysRevA.85.033817`.